

SMMAN: quasi-Simultaneous Multi-wavelength Monitoring of gamma-ray-loud AGNs with the Nanshan 26-m radio telescope

LANG CUI ^{1,2,3} KRISHNA MOHANA A ¹ XIN WANG ^{1,2} NING CHANG ¹ GUIPING TAN,¹ AND XIANG LIU ¹

¹State Key Laboratory of Radio Astronomy and Technology, Xinjiang Astronomical Observatory, CAS, 150 Science 1-Street, Urumqi 830011, China

²School of Astronomy and Space Science, University of Chinese Academy of Sciences, No.1 Yanqihu East Road, Beijing 101408, China

³Xinjiang Key Laboratory of Radio Astrophysics, 150 Science 1-Street, Urumqi 830011, China

ABSTRACT

Active Galactic Nuclei (AGNs) are characterized by strong temporal flux density variability across the electromagnetic spectrum, offering insights into the complex physical processes governing accretion and plasma outflows. To systematically investigate AGNs flux density variability in radio bands, a long-term program was initiated in late 2016: quasi-Simultaneous Multiwavelength Monitoring of gamma-ray-loud AGNs with the Nanshan 26-m radio telescope (SMMAN). This work presents the first data release of the SMMAN program, spanning over eight years from 2016 to 2024 with observations at 4.8 and 23.6 GHz. The SMMAN sample includes 131 northern ($\delta > \sim 0^\circ$) sources selected from the Fermi Large Area Telescope third source catalog. The characteristics of variability, spectral index, luminosity, and γ -ray loudness factor are examined for different AGN classes within the sample. Target sources exhibit stronger variability at 23.6 GHz compared to 4.8 GHz, with BL Lac objects being more variable than flat-spectrum radio quasars (FSRQs). BL Lacs generally have flatter radio spectra, while FSRQs, blazar candidates of uncertain type (BCUs), and radio galaxies (RDGs) span a wider range from flat to steep. FSRQs are more radio-luminous than BL Lacs and other classes, with BCUs intermediate and RDGs generally fainter. FSRQs and BL Lacs have higher γ -ray loudness factors than RDGs, while BCUs have intermediate values. The SMMAN dataset, incorporated with other historical and ongoing monitoring programs, will provide a unique opportunity to investigate the evolution of spectral energy distributions, search for quasi-periodic oscillations, and analyze supermassive black hole binary systems.

Keywords: Astronomy databases (83); Active galactic nuclei (16); Relativistic jets (1390); Radio continuum emission (1340); Gamma-rays (637)

1. INTRODUCTION

Galaxies that contain a highly bright, compact region at their center, called active galactic nuclei (AGNs), are known as active galaxies (Urry & Padovani 1995). It is found that the high luminosity at the central compact region is powered by supermassive black holes (SMBH; mass $\sim 10^8 - 10^9 M_\odot$) via processes known as accretion (Frank et al. 2002). Active galaxies are also found to possess relativistic jet structures emanating from the central region (Rees 1966). Active galaxy's multiwave-

length emission is dominated by non-thermal radiation extending from radio to γ -ray bands exhibiting intense and rapid flux density variations. In particular, a class of AGNs called blazars with a relativistic jet pointing towards Earth show extreme variability (Blandford & Rees 1978; Blandford & Königl 1979). Due to the small jet viewing angle, the blazar's observed emission is highly Doppler boosted and outshines all other components, thus making them ideal candidates to study the physical conditions and emission processes in relativistic jets. From an observational standpoint, blazars are categorized into two sub-classes: flat-spectrum radio quasars (FSRQs) and BL Lacertae (BL Lacs) objects. FSRQs exhibit emission line equivalent widths (EW) $> 5 \text{ \AA}$, while BL Lacs show $\text{EW} < 5 \text{ \AA}$ (Stocke et al. 1991;

Stickel et al. 1991). As per the classification suggested by Ghisellini et al. (2011), which relies on the luminosity of the broad-line region (BLR), FSRQs exhibit a higher BLR luminosity ($L_{\text{BLR}}/L_{\text{Edd}} > 5 \times 10^{-4}$) compared to BL Lacs, with L_{Edd} representing the Eddington luminosity of the supermassive black hole located at the core of the AGN. The flux variability timescales in blazars range from minutes to years (e.g., Boettcher 2004; Foschini et al. 2013; Orienti et al. 2014; Böttcher 2019, and references therein) and were classified into three types caused by different mechanisms (Fan 2005). These variations occur as flares or the quiescent/low-activity states. Another key feature of active galaxies is that their broadband spectral energy distribution (SED) from radio to γ -rays exhibits two-hump structure (e.g. Fossati et al. 1998). In addition, it is observed that AGNs/blazars exhibit high optical and radio polarization during flaring periods along with their polarization, showing intensive variability not only in terms of fraction but also in terms of the orientation of the polarization plane (e.g. Jorstad et al. 2007; Marscher et al. 2010; Blinov et al. 2021).

Studying the physical properties of AGNs through multi-frequency data has been found to be one of the most effective ways in the past, which has been employed in several studies (Marscher 2016; Böttcher 2019, and the references therein). A key feature of AGNs is that the flux density observed from them shows variations across different wavebands over varying time intervals. Further, it is observed that the behavior of the broadband flares of blazars is quite complex. The literature study points out that such flaring activities are not always simultaneous in different wavebands. Also, it is important to study the long-term activity of blazars. From the multiband observations of the AGNs, it is noticed that the variability patterns in different wavebands are sometimes correlated and sometimes not (e.g. Liodakis et al. 2018, and references therein). Comprehending the physical basis for the observed variability remains one of the key unresolved issues in the study of AGNs. Temporal studies can be an efficient method to extract the time evolution trends of observed variability and to identify plausible connections across various blazar emission bands (e.g. Liodakis et al. 2018, and references therein). Therefore, a highly effective approach to comprehending jet emission and its dynamics involves examining the alterations in the physical characteristics of AGNs/blazars that are necessary to generate variations in multi-frequency light curves. Hence, simultaneous monitoring of the AGNs across different wavelengths is important to discern the physical mech-

anisms in them.

The “*Fermi Gamma-ray Space Telescope*” (hereafter *Fermi*) was launched in June of 2008 and the “Large Area Telescope” (LAT; Atwood et al. 2009) on-board provides a unique opportunity for the systematic study of AGNs/blazar variability (Böttcher 2019; Principe 2022; Casaburo et al. 2025). *Fermi*-LAT with its initial four years of observation, the source catalog (3FGL; Acero et al. 2015) includes blazars that account for more than $\sim 60\%$ of the identified sources. The most recent update of the fourth source catalog (4FGL-DR4) spans more than 14 years and includes a total of 7,195 sources within the energy range of 50 MeV to 1 TeV (Abdollahi et al. 2020; Ballet et al. 2023). Approximately 56% of these sources are associated with AGNs, including blazars. Conducting a comprehensive monitoring campaign of AGNs across multiple bands (radio to γ -ray) and carrying out temporal and spectral analysis is essential to understand the causes of the underlying flux density variations in them. Under this motivation, prior to the launch of the *Fermi* and after it, there are a few ongoing and historical AGNs multiband monitoring programs¹. A few of the major radio band surveys are briefly introduced below, with emphasis on the importance of multi-frequency radio monitoring projects. The University of Michigan Radio Astronomy Observatory’s (UMRAO; Aller et al. 1985) 26-m paraboloid telescope was devoted to monitoring the flux density and polarization of blazar jets from the mid-1960s until June 2012 (Aller et al. 2017). This facility provided centimeter-band variability over decades at 14.5, 8.0, and 4.8 GHz. The UMRAO data have been utilized in numerous extensive studies concerning flaring blazars and to acquire information regarding various jet and shock parameters that are not directly observable (Aller et al. 2014; Hughes et al. 2015; Aller et al. 2016) and also in several multiband temporal and spectral studies (e.g. Krishna Mohana et al. 2024; Mohana A et al. 2025). UMRAO observations were also used for the calibration and interpretation of the less frequently sampled Very Long Baseline Array (VLBA) imaging data (Aller et al. 2017, and references therein). It is to be noted that the long-term monitoring data set could help to search for a supermassive black hole binary (SMBHB) candidates by identifying the periodic nature in the light curves (e.g. Readhead et al. 2025; Molina et al. 2025).

¹ <https://www.cv.nrao.edu/MOJAVE/blazarlist.html>

The radio telescope RATAN-600 (Parijskij 1993) in Zelenchukskaya, Russia, which is an ongoing survey, has regularly monitored AGNs, including blazars, since 2005. The observations were carried out with the six frequency bands at 1.25, 2.25, 4.7, 8.2, 11.2, and 22.3 GHz, simultaneously (within 1–2 min) when a source moves along the focal line where the receivers are located. These data formed the basis for the first version of the BLcat (Mingaliev et al. 2014), and the latest updated version of this catalog is “RATAN-600 multi-frequency catalog of blazars” (Sotnikova et al. 2022), which includes about 1830 source. Using these catalogs with information of flux densities, spectral indices, variability, and radio luminosity for the large blazar list, several studies to understand the flare activity and synchrotron radio spectra of AGNs were reported (e.g. Mufakharov et al. 2015; Sotnikova et al. 2019; Larionov et al. 2020; Sotnikova et al. 2021; Krishna Mohana et al. 2024; Kunert-Bajraszewska et al. 2025). The Fermi-GST AGN Multi-frequency Monitoring Alliance (F-GAMMA) programme (Fuhrmann et al. 2007; Angelakis et al. 2010; Fuhrmann et al. 2014), conducted at the Effelsberg telescope and IRAM 30 m telescope in Germany, performed nearly monthly broadband radio monitoring of selected blazars from January 2007 to January 2015 (Angelakis et al. 2019). The monitoring was carried out at multi-frequency from 2.64 to 43 GHz, which includes the frequencies of 2.64, 4.85, 8.35, 10.45, 14.6, 23.05, 32, 43, 86.2, 142.3, and 228.9 GHz. Using initial 3.5 yr data, a cross-correlation analysis was carried out by Fuhrmann et al. (2014) between the radio and γ -ray light curves of 54 *Fermi*-bright blazars, with the aim of determining the exact location of the γ -ray emission region. Fuhrmann et al. (2016) reported a multi-frequency study of AGNs in *Fermi* era to examine whether the γ -ray loudness is related to the radio variability. The 2007-2015 multi-frequency radio data published in Angelakis et al. (2019) is used in several temporal and spectral studies of blazars (e.g. Paliya et al. 2021; Kim et al. 2022; Krishna Mohana et al. 2024).

The Owens Valley Radio Observatory (OVRO) blazar monitoring program (Richards et al. 2011) offers an extensive data collection to examine AGNs variability at 15 GHz. It stands as the most comprehensive and sensitive radio monitoring survey of blazars, which has been in progress since 2008. Currently, the complete sample encompasses approximately 1850 sources, each of which is observed at a frequency of roughly twice a week. Observations from OVRO helped make progress in blazar jet physics through cross-correlations in the time domain

between *Fermi*-LAT γ -ray and 15 GHz light curves. It was found that there is a close connection between γ -ray and 15 GHz blazar emission (Max-Moerbeck et al. 2014; Hovatta et al. 2015; Pushkarev et al. 2019). In 2004, a program was initiated to monitor blazars at the 32 m radio antennas of the INAF-Institute of Radioastronomy (IRA), located in Medicina and Noto, Italy (Bach et al. 2007). Beginning in 2004, 47 targets were observed with a monthly cadence at 5, 8, 24, and 43 GHz. The Radio Observations of Blazars with INaf telescopes (ROBIN) program has continued to thrive over the years and remains active at frequencies of 8 and 24 GHz, having reached 20 years of operation (Marchili et al. 2025). The data accumulated through the program have been utilized in numerous studies and publications, primarily in relation to Whole Earth Blazar Telescope (WEBT) multi-frequency campaigns (e.g. Raiteri et al. 2007; Abdo et al. 2010a; Carnerero et al. 2015; Raiteri et al. 2017, 2024). The monitoring program has facilitated the examination of how the variability characteristics and SED of blazars evolve over time (Marchili et al. 2025, and references therein).

At the Aalto University Metsähovi Radio Observatory (MRO, Finland), several hundred AGNs and a few galactic microquasars have been monitored at 22, 37, and 87 GHz since 1980 using the 13.7 m radio telescope (Teraesranta et al. 1998). At present, there are 271 sources in the MRO monitoring program with data at 22 and 37 GHz, where the latter includes observations spanning up to 42 years. Data from this ongoing program have contributed to research on the long-term behavior, statistical properties, source populations, and radio variability models of AGNs. This monitoring has enabled studies of the radio to γ -ray connection in blazars, as well as radio versus optical behavior and multi-frequency variability models (e.g. Hovatta et al. 2007; Kankkunen et al. 2025). The Submillimeter Array (SMA; Gurwell et al. 2007) in Hawaii, United States, has been monitoring the quasars to determine the flux densities and variability at 230 and 345 GHz since the beginning of 2003 with 437 sources at present. The observations from this program were utilized in different long-term timing and spectral studies of AGNs (e.g. Villata et al. 2009; Fuhrmann et al. 2014; Jorstad & Marscher 2016).

The above-mentioned radio monitoring programs were successful in providing data, complementing other multiband observations. The studies above show that a comprehensive investigation into radio and radio/ γ -ray populations helps to address the enduring questions

about AGNs physical attributes. These include the location, structure, and radiative characteristics of the γ -ray emission region. Additionally, such research addresses the collimation, composition, particle acceleration, and emission mechanisms in AGNs/blazar jets. Also, to detect the presence of shorter and longer time scales of quasi-periodic oscillations (QPOs) in the AGNs light curves, it is essential to have long-term adequate continuous data (e.g. King et al. 2013; Li et al. 2023). Blazars have also been identified as candidate sources of PeV-energy neutrinos (IceCube Collaboration et al. 2018; Buson et al. 2022). To thoroughly explore blazars and the link between their radio emissions and neutrinos, multiband, high-cadence, long-term observations are essential (Kovalev et al. 2020; Plavin et al. 2020; Hovatta et al. 2021). Motivated by this, the quasi-Simultaneous Multiwavelength Monitoring of gamma-ray-loud AGNs with the Nanshan 26-m radio telescope (SMMAN) program operated by Xinjiang Astronomical Observatory (XAO) in China started in late 2016 and remains active. The information obtained from the SMMAN program, along with *Fermi*-LAT observations, will enable to systematically determine the radio and its connection with other multiband observational characteristics of the gamma-ray-loud AGNs population. In the following, we discuss the SMMAN dataset in 4.8 and 23.6 GHz. The details of the source sample and the radio data analysis are described in Section 2. In Section 3, we present and discuss the results. Finally, we summarize and conclude the findings of our work in Section 4.

2. OBSERVATION AND DATA REDUCTION

2.1. Facility

The SMMAN program is carried out with the Nanshan Radio Telescope (NSRT), which is located on the Nanshan Mountain, with the geographic coordinates of 43°28'17"N, 87°10'41"E, and an altitude of 2080 meters, ~ 70 km southwest of Urumqi city, China. Apart from single-dish scientific observations, NSRT has been involved in a large number of Very Long Baseline Interferometry (VLBI) observations in the last ~ 30 years, as a formal member of the European VLBI Network (EVN). NSRT now consists of a 26-meter parabolic antenna and four receivers operating at L-band (1-2 GHz), S/X-band (2.3/8.6 GHz), C-band (4-8 GHz), and K-band (22-24 GHz). The receivers utilized in the SMMAN program operate in the C and K bands, centered at 4800 MHz and 23600 MHz, with terminal recording bandwidths of 500 MHz for both. The main technical specifications of the receivers used in the SMMAN program are listed in Table 1.

Table 1. Main technical specifications of the receivers used in the SMMAN program.

Parameters		C-band	K-band
Center frequency	[MHz]	4800	23600
Terminal bandwidth	[MHz]	500	500
System temperature	[K]	26	45
Reference signal	[K]	1.7	2.5
FWHP/Beam	[arcsec]	546	105
Aperture efficiency	[%]	65	62
Conversion Factor	[K/Jy]	0.174	0.208

2.2. Source selection and monitoring schedule

Our goal is to monitor those bright variable blazars, the majority of which have been captured by the *Fermi*-LAT. Therefore, the initial source sample was established by filtering the *Fermi*-LAT 3FGL catalog (Acero et al. 2015) and cross-matching with the NRAO VLA Sky Survey (NVSS)² by putting a criteria of flux density at 1.4 GHz ($S_{1.4 \text{ GHz}} > 300$ mJy, point-like structure, and source declination (J2000) $> \sim 0^\circ$). Finally, our SMMAN sample contains 131 gamma-ray-loud AGNs, which include 113 blazars (FSRQs = 81 and BL Lacs = 32), nine active galaxies of uncertain type (bcu), seven radio galaxies (rdg), one compact steep spectrum quasar (css), and one steep spectrum radio quasar (ssrq), respectively. The distribution of SMMAN sources in the sky and their redshift distribution is illustrated in Figure 1. These sources were quasi-simultaneously monitored in the C and K bands using the 26-meter NSRT for the last approximately eight years (2016-2024), with a cadence of about one month.

2.3. Data Acquisition and Reduction

Flux density measurements with single-dish antennas can be performed through multiple modes, such as on-off, mapping, and cross-scan. Considering the monitoring efficiency and measurement accuracy, our SMMAN program has adopted the cross-scan mode. The cross-scan mode is achieved by performing multiple sub-scans of the target source in two orthogonal directions. Our observations were carried out with 4+4 sub-scans in azimuth and elevation over the target's position, respectively. The data were acquired in this manner at both C-band (4.8 GHz) and K-band (23.6 GHz). For a single sub-scan, the scan width is set to 5 times the beam width, which is ~ 50 and ~ 10 arcmin

² <https://www.cv.nrao.edu/nvss/>

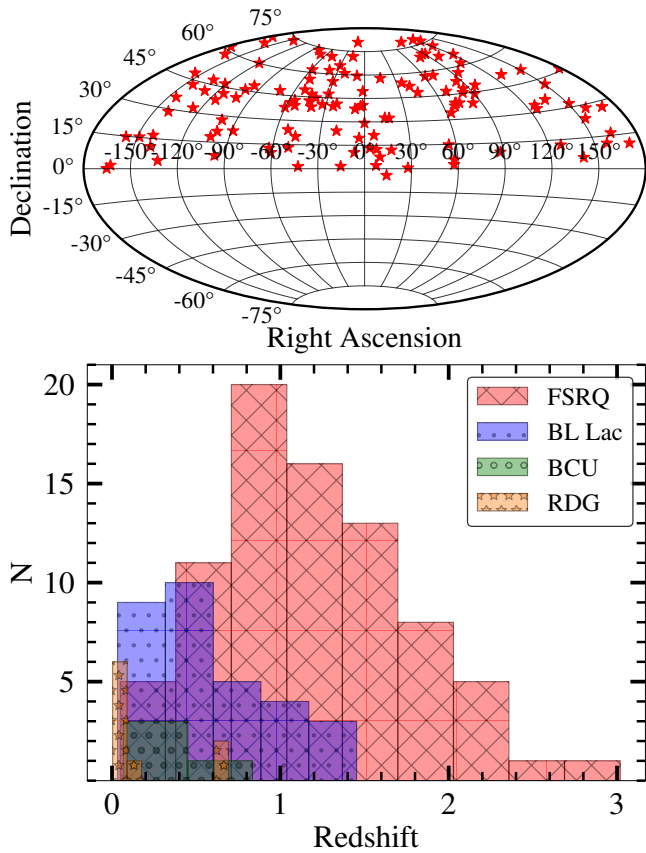


Figure 1. Top: the Hammer-Aitoff projection of the SM-MAN monitored sources in sky distribution (in equatorial coordinates). Bottom: the redshift distribution of the sources in the SM-MAN program.

for C-band and K-band, respectively. The total sampling time is set to 20 to 30 seconds for each sub-scan, while the sampling time for each data point is fixed at 64 ms during scanning.

The target samples are mainly point sources for the 26-meter NSRT at C and K bands. A sub-scan across the target is simply equal to a beam-wide Gaussian, which is the convolution of the source and the telescope beam. Given the structural perturbations induced by the telescope scanning motions, a Gaussian kernel with a full width at half maximum (FWHM) comparable to the beam size was adopted for scan data model fitting. During cross-scanning, the response attenuation in the orthogonal direction is determined by the Gaussian peak offset along both scan axes, thereby allowing for correcting flux density measurement reduction caused by pointing deviation. As an example, such a cross-scan mode is illustrated in Figure 2.

The data reduction and calibration process includes Gaussian fitting, pointing correction, gain correction, and absolute flux density calibration. Gaussian fitting is used to subtract the baseline of the system temperature drifting and extract the Gaussian-like signals from the sub-scans. Pointing correction is to calibrate the antenna pointing error with each other direction’s offset in the scans. After that, we subsequently conducted atmospheric opacity and antenna gain calibration to further correct the elevation gain effect. Finally, the absolute flux density was tuned using the calibration factors generated by three primary calibrators, 3C 48, NGC 7027, and 3C 286 (Baars et al. 1977; Ott et al. 1994; Zijlstra et al. 2008; Angelakis et al. 2015). The observed average flux density for these calibrator sources during the SM-MAN program is presented in Table 2.

Table 2. The observed average flux densities (in unit of Jy) of the standard calibrators during the SM-MAN program.

ν	Source		
(GHz)	3C 48	3C 286	NGC 7027
4.8	5.63 (0.11)	7.51 (0.16)	5.37 (0.11)
23.6	1.26 (0.19)	2.43 (0.22)	5.40 (0.39)

NOTE—The values quoted inside the parentheses are the standard deviation of the measurements.

All the data reduction and calibration processes above are conducted with the NSRT radio continuum data processing software *Data Analysis Application for Radio Continuum* (DAARC)³, which is developed by our team in Python language.

2.4. γ -ray data

We utilized the monthly binned γ -ray flux and spectral index data from the *Fermi*-LAT Light Curve Repository⁴ (LCR; Abdollahi et al. 2023) in the energy range of 0.1–100 GeV, covering the same time period as the radio observations (2016 November 1 to 2024 November 30) presented in this study. For a detailed description of the unbinned maximum-likelihood data analysis, we refer to Abdollahi et al. (2020). In this work, we employed the light curve obtained by allowing the spectral slope to vary freely during the fitting process and the fit results of only the convergent likelihood analysis. The significance of a source detection is evaluated using

³ <https://github.com/junliu/daarc>

⁴ <https://fermi.gsfc.nasa.gov/ssc/data/access/lat/LightCurveRepository/>

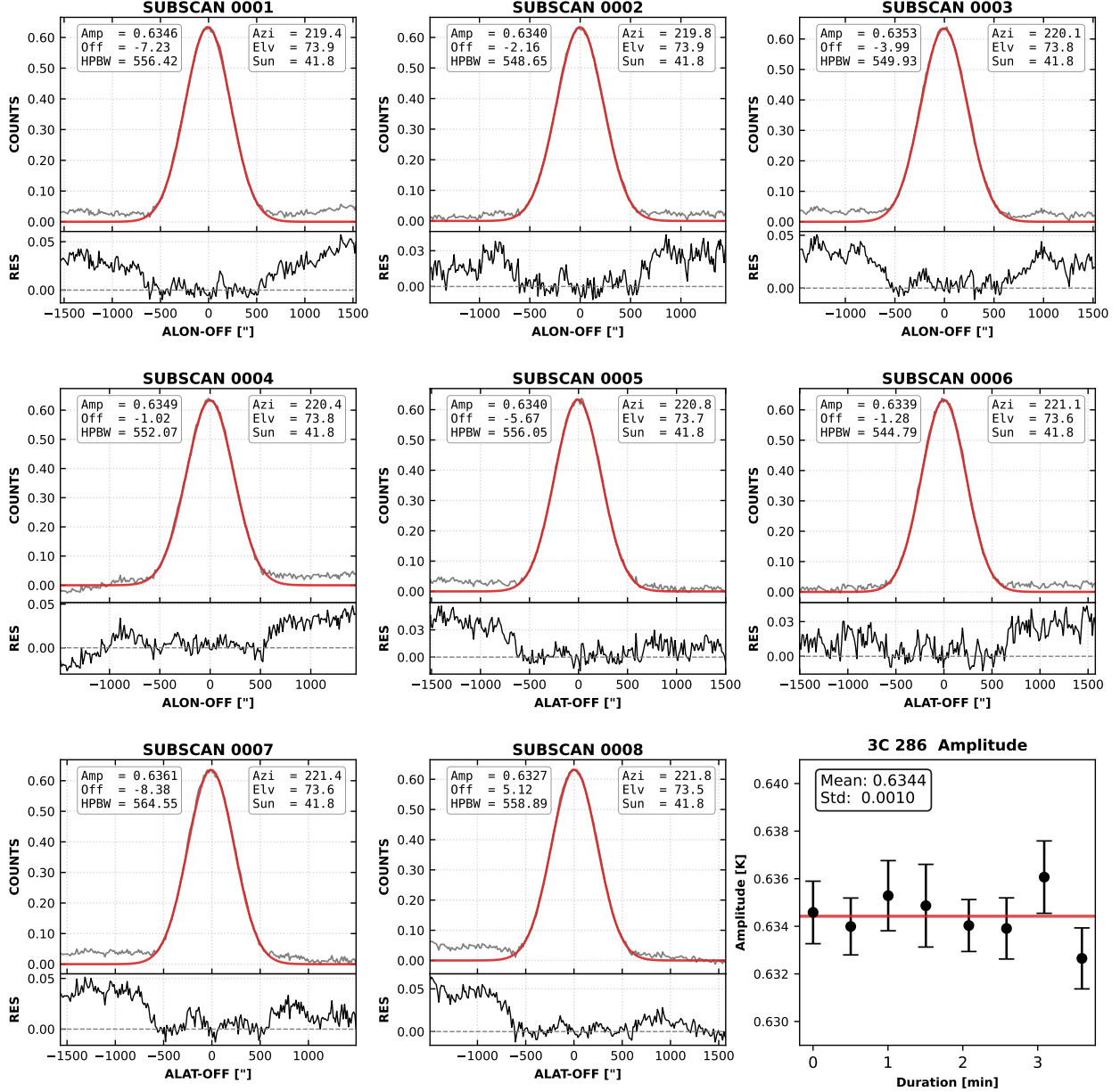


Figure 2. Example of a 4+4 cross-scan observation of the calibrator source 3C 286 at 4.8 GHz. The first four subplots display longitude (azimuthal) subscans, followed by the next four showing latitude (elevational) subscans. For each of these eight subplots, the upper panel presents the subscan results, with the red curve representing the Gaussian fit model and the grey line indicating the actual observed data. The lower panel beneath each subscan plot shows the residuals of the model fit. The final subplot summarizes the fitted Gaussian amplitudes from all individual subscans, with a solid red horizontal line indicating the mean amplitude.

the test statistic $TS = 2 \times \log(L_1/L_0)$, where L_0 is the likelihood of the null model (no source) and L_1 is the likelihood of the model that includes the source. In the monthly binned light curve, we only consider those bins with detection significance of $\geq 2\sigma$ ($TS \geq 4$), and the upper limit values (for non-detection bins) were not included. It is important to note that performing a full *Fermi*-LAT data analysis for 131 SMMAN sources

is computationally demanding and time-consuming. Therefore, we used the available light curves from the LCR. These light curves of various γ -ray sources from this repository have been utilized in previous research studies (e.g. Di Gesu et al. 2023; Wang et al. 2023).

3. RESULTS AND DISCUSSION

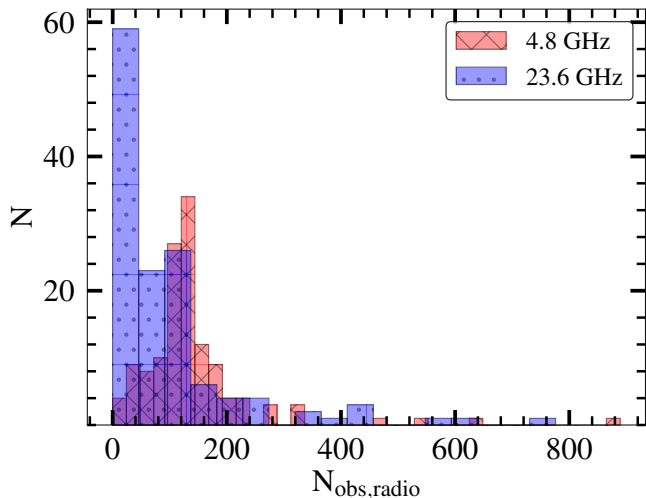


Figure 3. The number of radio measurements for the SM-MAN sources (131 objects).

The basic information about the sources that were monitored in this work is listed in Table 3 of Appendix A. Note that in our analysis and discussion part, we have considered the different AGN classes from Table 3 of the Appendix A as FSRQ (FSRQ+fsrq), BL Lac (BLL+bll), BCU (bcu), and RDG (RDG+rdg+css+ssrq). Here, the AGNs class is defined according to the *Fermi* Large Area Telescope Fourth Source Catalog Data Release 4 (4FGL-DR4; Ballet et al. 2023), with designations in capital letters representing confirmed identifications, and those in lower-case letters denoting associations. The number of radio measurements for the SM-MAN sources between 1 November 2016 and 30 November 2024, as presented in this work, is shown in Figure 3. Most sources have more observations at 23.6 GHz than at 4.8 GHz, and some sources have exceptionally large datasets with more than 400 measurements. All histogram figures presented in this work use binning based on Knuth’s optimal, data-driven method (Knuth 2006). The overlap of the SM-MAN sources with other historical surveys or ongoing monitoring programs is displayed in Figure 4. From this plot, one can easily identify the number of sources having counter monitoring data for the SM-MAN sample, which is useful for further studies that could cover more multiband radio observations. The sources that overlap among the SM-MAN targets and UMRAO, F-GAMMA, RATAN-600, OVRO, ROBIN, MRO, and SMA monitoring programs are shown in Table 4 of Appendix A.

To depict the importance of the SM-MAN monitoring program, a long-term multiband light curve of the BL Lac object S4 0954+65 using the data from the SM-

MAN, RATAN-600⁵ (Mingaliev et al. 2014; Sotnikova et al. 2022), F-GAMMA⁶ (Angelakis et al. 2019) and ROBIN⁷ (Marchili et al. 2025) monitoring program is shown in Figure 5. The plot clearly shows that the SM-MAN program has covered a greater number of observations after 2016 November compared to the other surveys (publicly available), which is important due to the fact that adequate continuous data are essential for long-term temporal and spectral studies, and the detection of QPOs. In addition, a part of the data from the SM-MAN program has been utilized in systematic studies of a few individual blazars in earlier research works (e.g. Kun et al. 2022; Krishna Mohana et al. 2024; Kun et al. 2024; Mohana A et al. 2025), which also showcase the significance of the SM-MAN program along with other multiwavelength observations.

3.1. Variability and Other Physical Parameter Estimations

To quantify the variability of sources, at each frequency band, the variability index (V_S) is calculated using the formula adopted from Aller et al. (1992), defined as

$$V_S = \frac{(S_i - \sigma_i)_{\max} - (S_i + \sigma_i)_{\min}}{(S_i - \sigma_i)_{\max} + (S_i + \sigma_i)_{\min}}, \quad (1)$$

where S_{\max} and S_{\min} are the maximum and minimum values of the flux density over all epochs of observations, while σ_{\max} and σ_{\min} are their root-mean-square errors. The uncertainty ΔV_S of the variability index was calculated as

$$\Delta V_S = \frac{2 S_{\min} (\sigma_{S_{\min}} + \sigma_{S_{\max}})}{(S_{\min} + S_{\max})^2} \quad (2)$$

The variability index is based solely on the two extreme flux density values. Therefore, it is necessary to characterize the variability of the light curve as a whole, incorporating all available flux density measurements. Hence, to identify the presence of true intrinsic variability in the light curve, we have used the fractional root mean square variability parameter (F_{var}), since it considers the uncertainties in flux density measurements. Here we use the relation given in Vaughan et al. (2003), which is defined as:

$$F_{var} = \sqrt{\frac{S^2 - \sigma^2}{r^2}} \quad (3)$$

⁵ <https://www.sao.ru/blcat/>

⁶ <https://cdsarc.cds.unistra.fr/viz-bin/cat/J/A+A/626/A60>

⁷ <https://cdsarc.cds.unistra.fr/viz-bin/cat/J/A+A/702/A140>

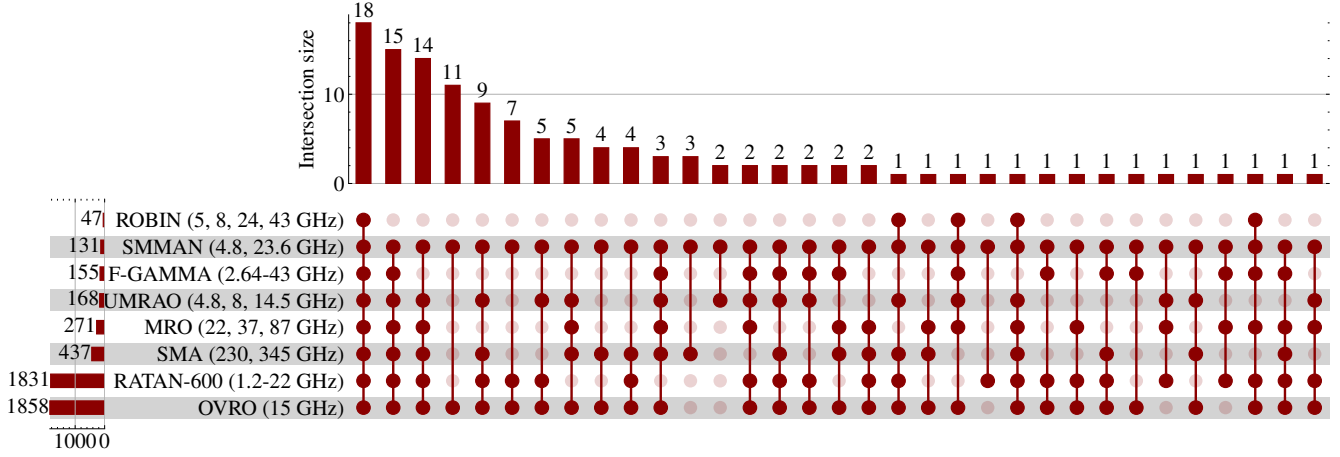


Figure 4. UpSet plot describing the overlapping of the SMMAN sources with other monitoring programs. Reading chart: the horizontal set size bar chart displays the total number of sources within each distinct monitoring program. Vertical intersection size bar chart, positioned at the top, illustrates the number of sources of each particular intersection or combination of monitoring programs. The solid dots and lines (linked by a vertical line) signify the sources that belong to a particular intersection.

S4 0954+65

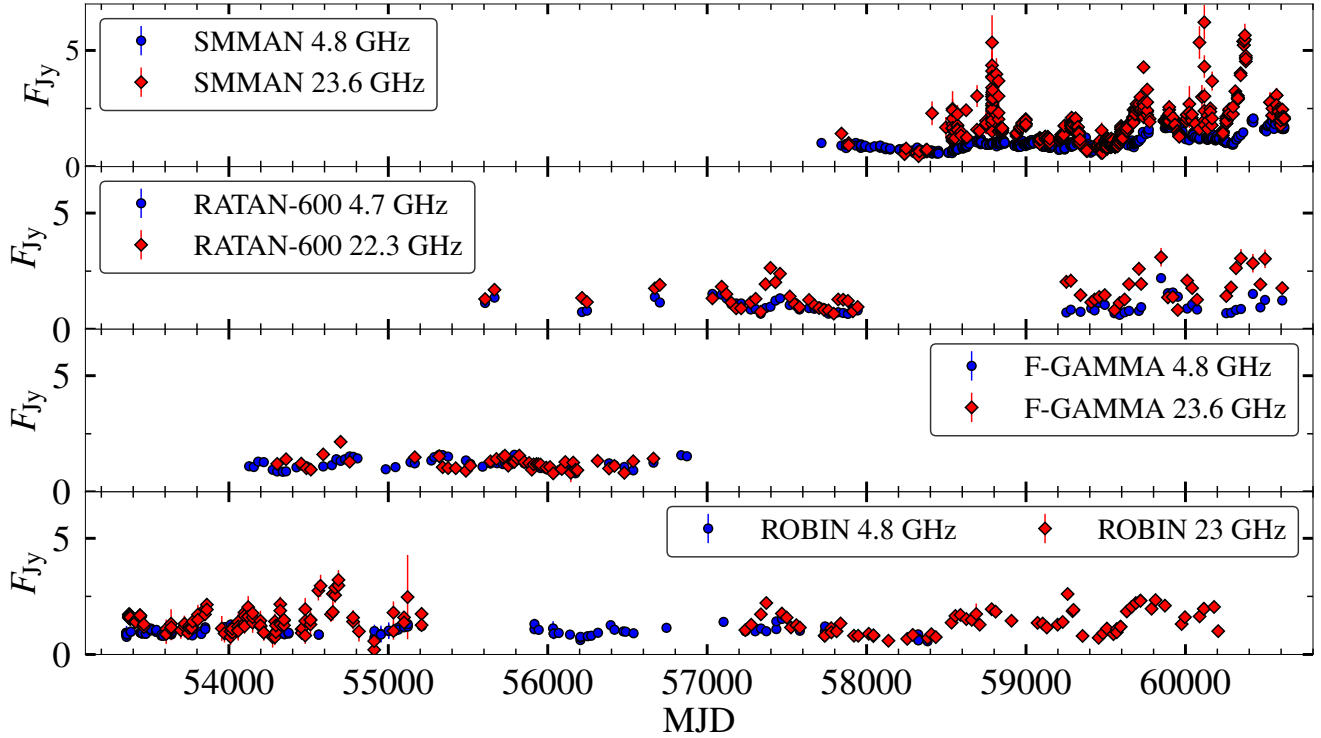


Figure 5. Multiband light curve of S4 0954+65 using SMMAN, RATAN-600, F-GAMMA, and ROBIN monitoring program data at ~ 4.8 and ~ 23 GHz.

$$err(F_{var}) = \sqrt{\left(\sqrt{\frac{1}{2N}} \cdot \frac{\sigma^2}{r^2 F_{var}}\right)^2 + \left(\sqrt{\frac{\sigma^2}{N}} \cdot \frac{1}{r}\right)^2} \quad (4)$$

where, $\sigma_{\chi^2}^2 = S^2 - \sigma^2$, is called excess variance, S^2 is the sample variance, σ^2 is the mean square uncertainties of each observation and r is the sample mean.

The radio spectral index is calculated in two frequency intervals (4.8 and 23.6 GHz). The radio spectral index

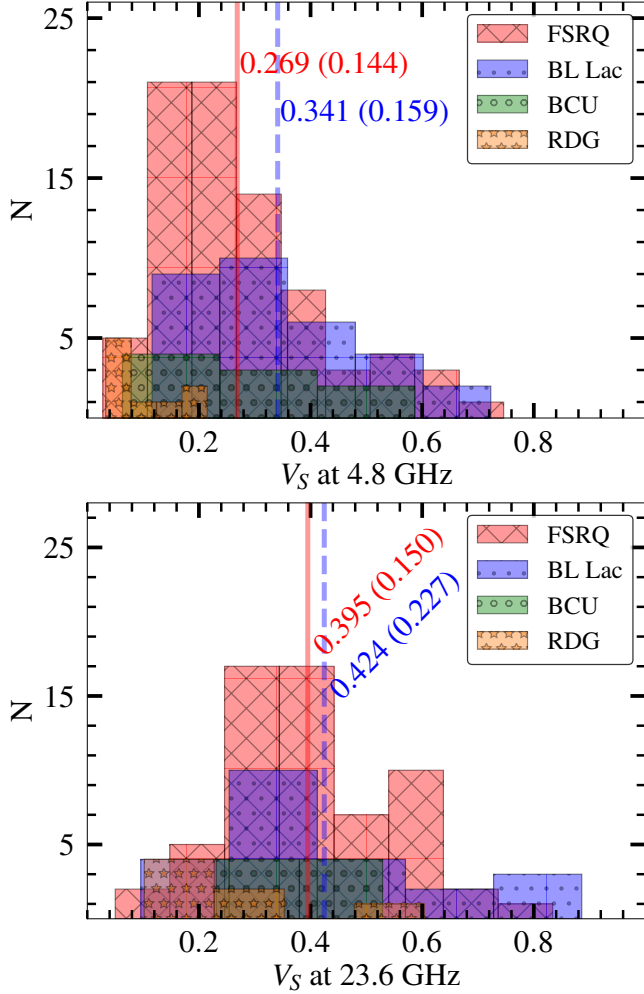


Figure 6. Histogram of the variability index at 4.8 GHz (top panel) and 23.6 GHz (bottom panel). The objects have been categorized according to their type of AGNs classification. The transparent solid red and dashed blue vertical lines represent the average values with standard deviation inside parentheses for FSRQs and BL Lacs, respectively.

α defined from the power law $S_\nu \sim \nu^\alpha$, where S_ν is the flux density at frequency ν , and α is a spectral slope. It is calculated using the formula:

$$\alpha = \frac{\log S_2 - \log S_1}{\log \nu_2 - \log \nu_1}, \quad (5)$$

where S_1 and S_2 are the flux densities at frequencies ν_1 and ν_2 , respectively. The uncertainty in the spectral index was determined using Gaussian error propagation as:

$$\Delta\alpha = K \sqrt{\left(\frac{\Delta S_{4.8 \text{ GHz}}}{S_{4.8 \text{ GHz}}}\right)^2 + \left(\frac{\Delta S_{23.6 \text{ GHz}}}{S_{23.6 \text{ GHz}}}\right)^2}, \quad (6)$$

where the factor of $K \approx |\log(4.8 \text{ GHz}/23.6 \text{ GHz}) \cdot \ln(10)|^{-1}$ arises from the derivation of the spectral in-

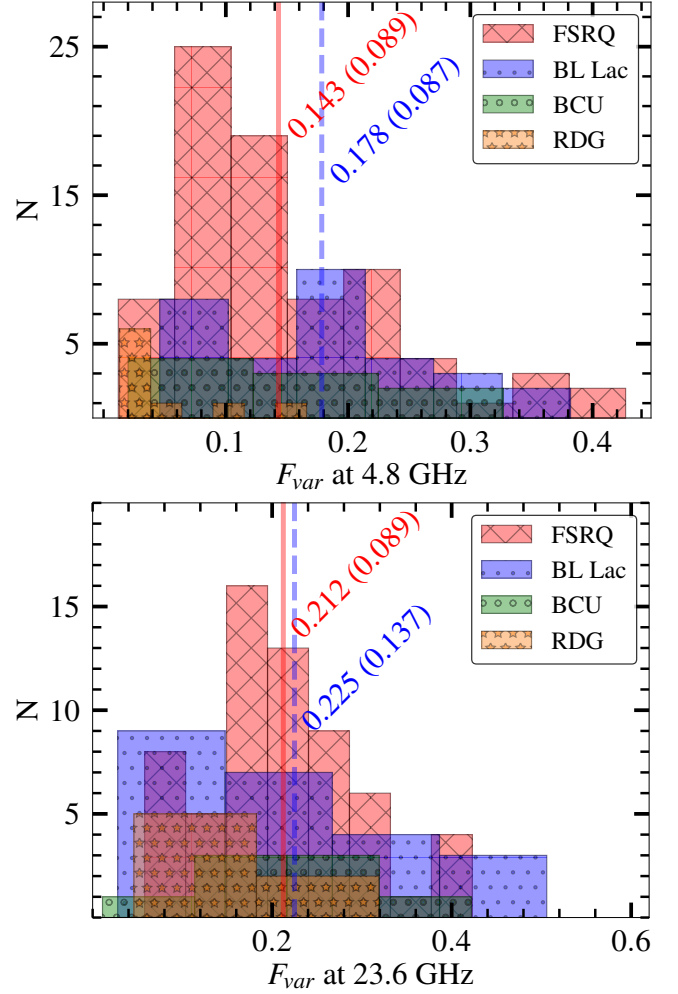


Figure 7. Histogram of the fractional variability at 4.8 GHz (top panel) and 23.6 GHz (bottom panel). The transparent solid red and dashed blue vertical lines represent the average values with standard deviation inside parentheses for FSRQs and BL Lacs, respectively.

dex as defined in Equation 5.

The radio luminosity was calculated at 4.8 and 23.6 GHz following the equation:

$$P = 4\pi D_L^2 S (1+z)^{-\alpha-1}, \quad (7)$$

where S is the measured flux density at 4.8 or 23.6 GHz, z is the redshift, α is the average spectral index in the interval 4.8 and 23.6 GHz, and D_L is the luminosity distance. For calculation of luminosity distances, we used the Λ CDM cosmology with $H_0 = 67.74 \text{ km s}^{-1} \text{ Mpc}^{-1}$, $\Omega_m = 0.3089$, and $\Omega_\Lambda = 0.6911$ (Planck Collaboration et al. 2016).

3.2. Characteristics of Radio Variability, Spectral index and Luminosity: Relation to AGNs Class

The estimated variability index values for different sources at 4.8 and 23.6 GHz are presented in Table 5 of Appendix A. The histograms of V_S at two frequencies are shown in Figure 6. At 23.6 GHz $\sim 97\%$ of the sources exhibit variability above the 10% level ($V_S > 0.1$), whereas at lower frequency 4.8 GHz $\sim 90\%$ sources show significant variability. The range in the variability for FSRQs and BL Lacs at 4.8 GHz is comparable (varying from < 0.1 up to ~ 0.74) with the mean value for FSRQs at 0.269 ($\sigma = 0.144$) and for BL Lacs at 0.341 ($\sigma = 0.159$). The BCU and RDG classes vary from < 0.1 up to maximum values of 0.21 and 0.59, respectively. Similarly, at 23.6 GHz, the range of variability in FSRQs and BL Lacs is comparable (varying from < 0.1 up to ~ 0.85) with the mean value for FSRQs at 0.395 ($\sigma = 0.150$) and for BL Lacs at 0.424 (~ 0.227). The BCU and RDG classes vary from 0.1 up to maximum values of 0.53 and 0.60, respectively.

The calculated fractional variability values for different SMMAN sources in the C and K bands are given in Table 5 of the Appendix A. In Figure 7, we show fractional variability histograms at 4.8 and 23.6 GHz for different classes of AGNs in our sample. It is observed that at 4.8 GHz, $\sim 60\%$ of the sources show fractional variability $> 10\%$. The F_{var} value of the FSRQs found vary from $< 10\%$ to a maximum of $\sim 42\%$ with a mean value of 0.143 ($\sigma = 0.089$), BL Lacs show a range between $< 10\%$ and a maximum value of $\sim 30\%$ with a mean value of 0.178 ($\sigma = 0.087$). A similar trend of variation is observed in active galaxies of uncertain type with a maximum value up to $\sim 33\%$ and in radio galaxies with maximum variation up to 17%. In contrast to lower frequency behavior, $\sim 84\%$ of the sources exhibit fractional variability $> 10\%$. Here, the different classes show variation of $F_{var} > 10\%$ to maximum values of $\sim 42\%$, $\sim 50\%$, $\sim 42\%$, and $\sim 32\%$ in FSRQs, BL Lacs, BCUs, and RDGs, respectively. At 23.6 GHz, the mean value of F_{var} for FSRQs and BL Lacs is found to be 0.212 ($\sigma = 0.089$) and 0.225 ($\sigma = 0.137$), respectively. It is noticed that from both the estimation of variability index and fractional variability values at 4.8 and 23.6 GHz, a trend for sources to exhibit a higher degree of variability at 23.6 GHz than at 4.8 GHz, with a mean value for BL Lacs higher than the FSRQs. These results are consistent with the pattern reported by [Aller et al. \(1992\)](#) and [Sotnikova et al. \(2022\)](#) for a sample comprising 62 extragalactic objects (at 4.8 and 14.5 GHz) and 1700 blazars (in frequency range 1.2-22.3 GHz),

respectively.

The average spectral index with associated error and the range in spectral index (minimum and maximum values) over the entire observing period are presented in Table 5 of the Appendix A. It is worth noting that when estimating the spectral index, monthly averaged flux densities were used to ensure temporal alignment between the two frequencies. In Figure 8, the left panel shows the distribution of average spectral indices, while the right panel displays the range of spectral indices versus their average values for the various AGNs classes in the SMMAN sample. BL Lac objects tend to exhibit comparatively flatter spectra than the other classes, whereas FSRQs, BCUs, and RDGs show a broader distribution, spanning from flat to steep. The mean spectral indices for FSRQs is -0.032 ($\sigma = 0.172$) with values ranging between -0.387 and $+0.437$. For BL Lacs, the spectral index ranges from -0.212 to $+0.313$, with a mean of $+0.032$ ($\sigma = 0.158$). Radio galaxies generally display steep spectra (ranging between -0.851 to 0.178), and the BCUs are also skewed toward steeper spectral indices (varying from -0.851 to -0.057). Also, the BL Lacs and FSRQs were found to show a higher degree of variability trend at both frequency bands compared to the other classes.

Figure 9 shows variability indices versus average spectral index in the range of 4.8-23.6 GHz. At both 4.8 and 23.6 GHz, ~ 90 of the sources with $\alpha \geq -0.4$ show variability greater than 10% level. The majority of these sources belong to the FSRQ and BL Lac classes. Also, sources with $\alpha \leq -0.4$ exhibit a low degree of variability at both frequency bands. Interestingly, the radio galaxy 3C 111 with $\alpha = -0.696$ shows variability above 10% at both 4.8 and 23.6 GHz with a maximum value of $V_S = 0.604$ at 23.6 GHz. Such large variability could be due to the major outburst, which is usually associated with the release of radio knots from the core ([Kadler et al. 2008](#); [Grossberger et al. 2012](#)). Similar features are noticed in the case of fractional variability versus the average spectral index plot (Figure 10).

The radio luminosity was calculated using the Equation 7 for different classes of AGNs in our sample, the distribution is presented in Figure 11, and the values are given in the Table 5 of the Appendix A. The distribution ranges from 2.58×10^{24} to 5.65×10^{28} W Hz $^{-1}$ at 4.8 GHz, and from 6.60×10^{23} to 3.68×10^{31} W Hz $^{-1}$ at 23.6 GHz. In both frequency bands, FSRQs exhibit higher radio luminosity than BL Lacs and other classes. Specifically, at 4.8 GHz, FSRQs have radio luminosi-

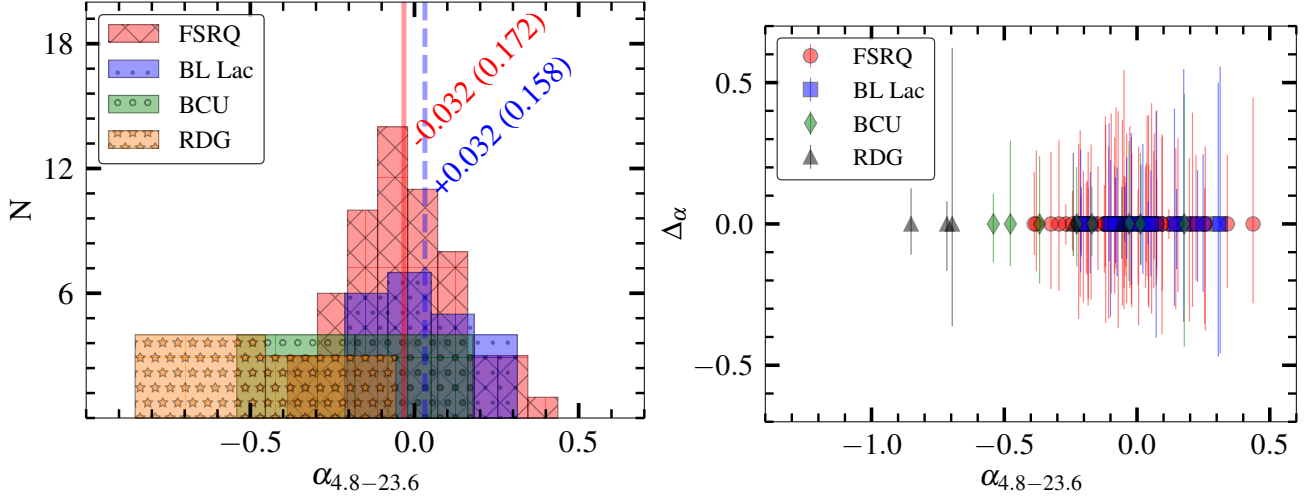


Figure 8. Histogram of average radio spectral index in the spectral region 4.8-23.6 GHz (left panel). The transparent solid red and dashed blue vertical lines represent the average values with standard deviation inside parentheses for FSRQs and BL Lacs, respectively. The spread of spectral indices, estimated as the difference between maximum and minimum values in the region 4.8-23.6 GHz, as a function of average spectral index (right panel).

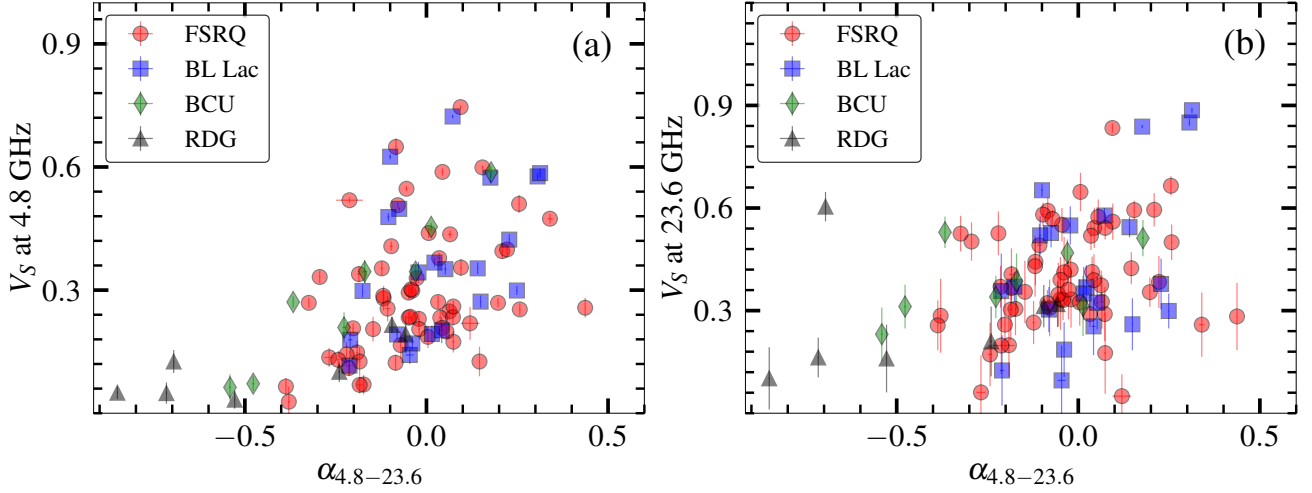


Figure 9. Variability index vs. average spectral index at 4.8 GHz (a) and 23.6 GHz (b).

ties from 1.19×10^{25} to 5.65×10^{28} W Hz^{-1} (mean 9.47×10^{27} , $\sigma = 12.06 \times 10^{27}$ W Hz^{-1}), while BL Lacs range from 3.84×10^{24} to 9.55×10^{27} W Hz^{-1} (mean 1.88×10^{27} , $\sigma = 2.47 \times 10^{27}$ W Hz^{-1}). At 23.6 GHz, the BL Lacs span from 2.74×10^{24} to 1.23×10^{28} W Hz^{-1} (mean 1.95×10^{27} , $\sigma = 2.81 \times 10^{27}$ W Hz^{-1}) and FSRQs from 1.17×10^{25} to 6.20×10^{28} W Hz^{-1} (mean 9.21×10^{27} , $\sigma = 11.29 \times 10^{27}$ W Hz^{-1}). In both bands, BCUs have radio luminosities intermediate between BL Lacs and FSRQs. RDGs exhibit lower luminosities, typically below the mean value of FSRQs.

3.3. Gamma-ray and Radio Properties of the SMAN Sample

To investigate the connection between radio and γ -ray emissions, we use *Fermi*-LAT data in the energy range of 0.1 – 100 GeV covering the same time period (2016 November 1 to 2024 November 30) as that of the radio observation presented in this work. The details of the γ -ray data are provided in Section 2. The LCR provides light curves for all sources in the 4FGL-DR2 catalog with a variability index greater than 21.67 (Abdollahi et al. 2023). This index serves as a proxy for the average fractional variability $\delta F/F$, where δF is measured on timescales of one year. Consequently, among the 131 SMAN sources, we obtained monthly binned light curves and spectral indices for 105. From the light curves, we calculated the average flux and spectral in-

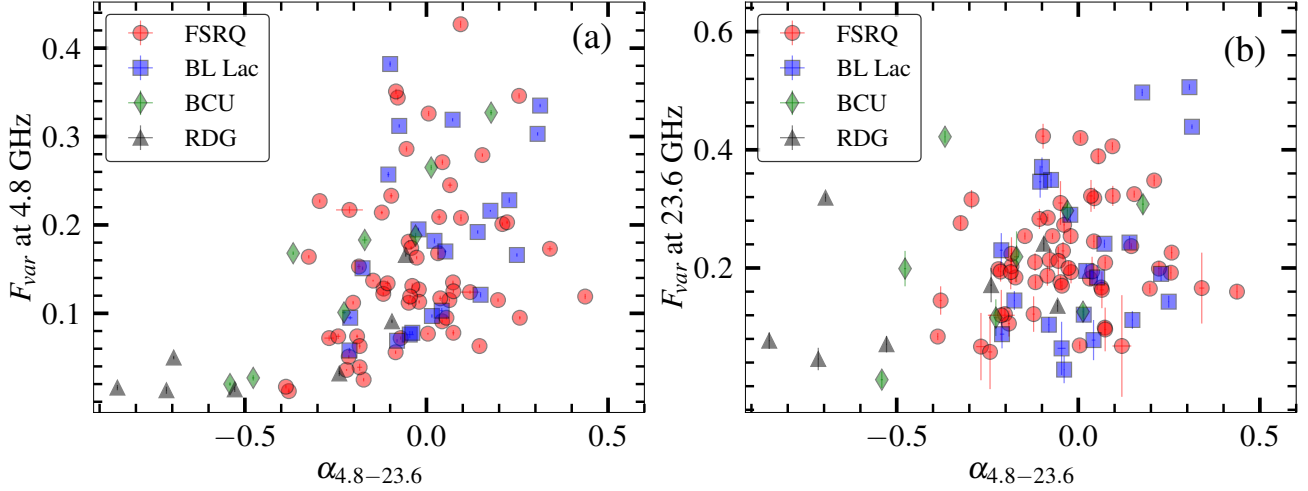


Figure 10. Fractional variability vs. average spectral index at 4.8 GHz (a) and 23.6 GHz (b).

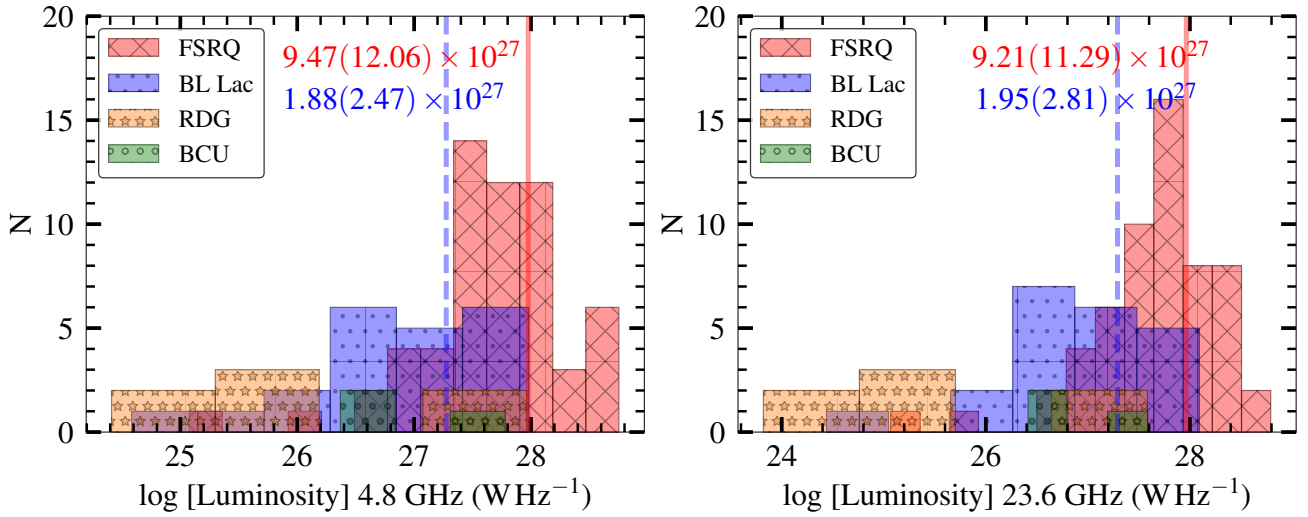


Figure 11. Distribution of the radio luminosity at 4.8 GHz (left panel) and 23.6 GHz (right panel). The transparent solid red and dashed blue vertical lines represent the average values with standard deviation inside parentheses for FSRQs and BL Lacs, respectively.

indices; the values are presented in Table 5 of the Appendix A. Further, following the procedures described in Böck et al. (2016) with the assumption that sources have a power-law photon flux spectrum (Equation 8), the γ -ray energy flux and luminosities for the 105 sources were calculated as follows.

$$N_{\text{ph}}(E) = S_{\text{ph}} \frac{1-\Gamma}{E_0} \left[\left(\frac{E_{\text{max}}}{E_0} \right)^{1-\Gamma} - \left(\frac{E_{\text{min}}}{E_0} \right)^{1-\Gamma} \right]^{-1} \left(\frac{E}{E_0} \right)^{-\Gamma} \quad (8)$$

where S_{ph} is the estimated photon flux in the energy band from E_{min} to E_{max} (E_0 is the reference energy used to make the expression dimensionless while applying a non-integer exponent), for photon index $\Gamma \neq 1$. Then the energy flux in that band is given by

$$S_E = S_{\text{ph}} E_0 \frac{1-\Gamma}{2-\Gamma} \frac{(E_{\text{max}}/E_0)^{2-\Gamma} - (E_{\text{min}}/E_0)^{2-\Gamma}}{(E_{\text{max}}/E_0)^{1-\Gamma} - (E_{\text{min}}/E_0)^{1-\Gamma}} \quad (9)$$

for $\Gamma \neq 2$.

Because the sources in the sample are distributed across various redshifts, the measured luminosities were corrected using the K-correction as described by Ghisellini et al. (2009), i.e.,

$$L_E = 4\pi d_L^2 \frac{S_E}{(1+z)^{2-\Gamma}} \quad (10)$$

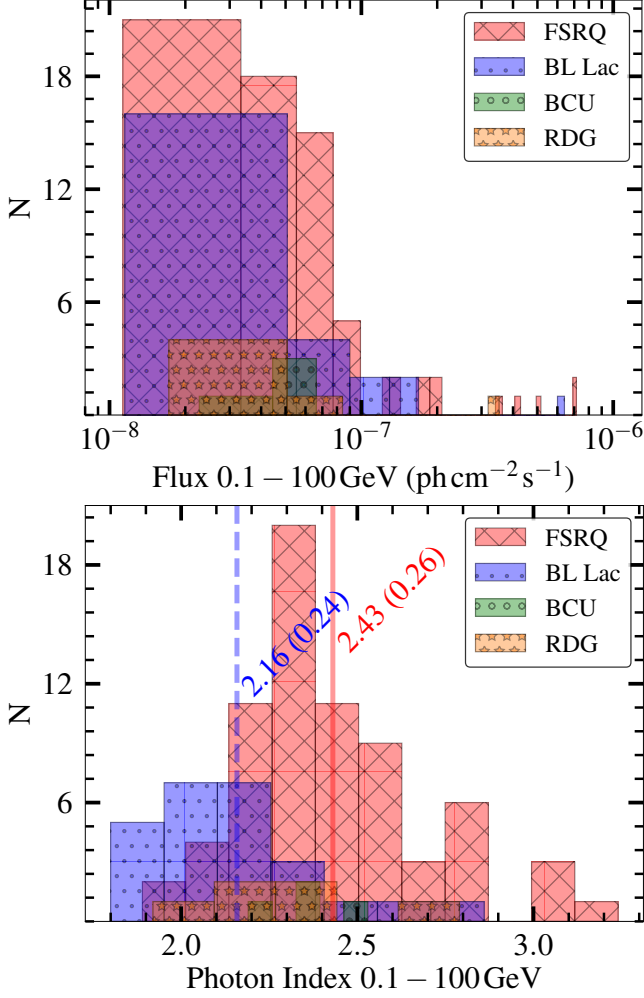


Figure 12. Top: *Fermi*-LAT flux distribution of the sources. Bottom: *Fermi*-LAT γ -ray photon index distribution of the sources. The transparent solid red and dashed blue vertical lines represent the average values with standard deviation inside parentheses for FSRQs and BL Lacs, respectively.

where z is the redshift of the source, S_E the energy flux, and Γ the photon spectral index in the γ -ray band. The luminosity distance, d_L , was calculated assuming a flat universe with the cosmological parameters same as those used in the estimation of the radio luminosity.

The γ -ray flux distribution for the SMMAN sample is shown in the top panel of Figure 12, while the bottom panel presents the corresponding distribution of spectral indices. On average, BL Lacs tend to exhibit harder spectra than FSRQs, consistent with earlier results based on the 3FGL sources (see Figure 7 of Ackermann et al. 2015). We performed the two sample Kolmogorov–Smirnov (KS) test to check whether the BL Lac objects have the same distribution as those of FSRQs. The test shows a strong statistical result with

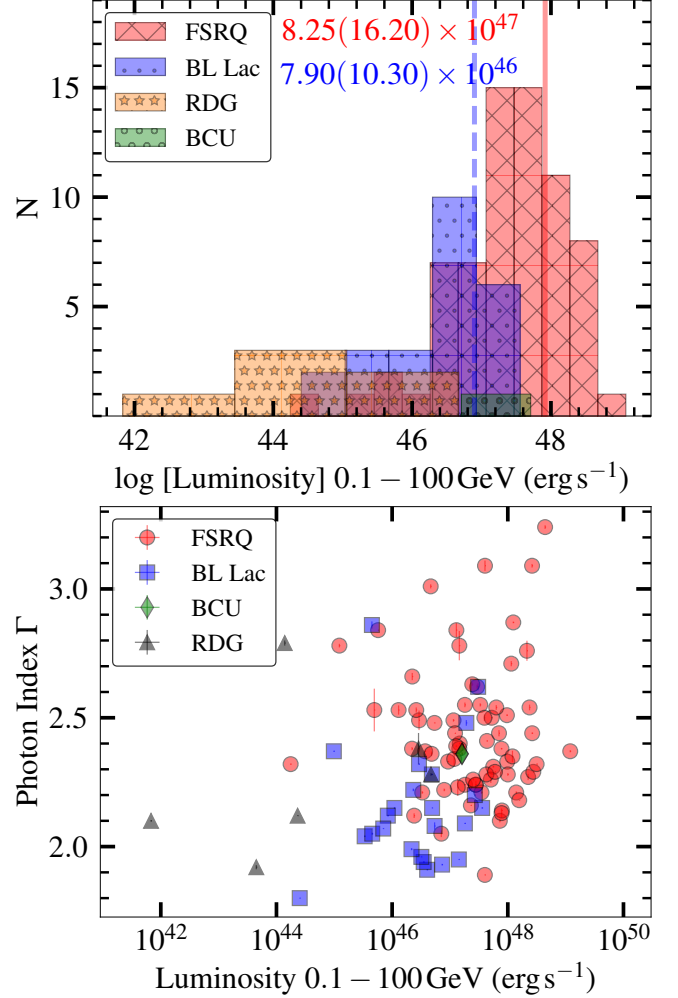


Figure 13. *Fermi*-LAT γ -ray luminosity distribution of the sources (top panel). The transparent solid red and dashed blue vertical lines represent the average values with standard deviation inside parentheses for FSRQs and BL Lacs, respectively. γ -ray luminosities Vs. photon indices for different source classes (bottom panel).

a p -value of 7×10^{-6} . This result is in agreement with earlier studies, which have shown a relationship between the γ -ray spectral index and the peak frequency of the synchrotron component in the spectral energy distribution. It is to be noted that blazars were also classified into three subclass based on the synchrotron peak frequency (ν_p): low-synchrotron-peaked (LSP; $\log(\nu_p) < 14$ Hz), intermediate-synchrotron-peaked (ISP; $14 \text{ Hz} < \log(\nu_p) < 15$ Hz), and high-synchrotron-peaked (HSP; $\log(\nu_p) > 15$ Hz) blazars (Abdo et al. 2010b; Fan et al. 2016; Yang et al. 2022). As the synchrotron peak frequency drops, their γ -ray spectra become softer (see, e.g., Figure 17 of Ackermann et al. (2011) and Figure 10 of Ackermann et al. (2015)).

The observed γ -ray luminosities, as calculated from Equation 10 and given in Table 5 of the Appendix A, exhibit a clear dependence on the classification of the source (top panel of Figure 13). The luminosities of radio galaxies are low, those of BL Lac objects are in between, while FSRQs exhibit high luminosities. The bottom panel of Figure 13 shows the relation between the γ -ray luminosity and the spectral index. A trend of the spectral index becoming harder with decreasing luminosity is noticed. This relation for all *Fermi*-LAT detected AGNs in 3FGL is presented in Figure 14 of Ackermann et al. (2015) and in the Figure 10 of Ajello et al. (2020) for the fourth *Fermi*-Large Area Telescope Source Catalog (4FGL; Abdollahi et al. 2020). This pattern has been widely addressed in the perspective of “blazar sequence” in the earlier studies (Ackermann et al. 2015, and references therein).

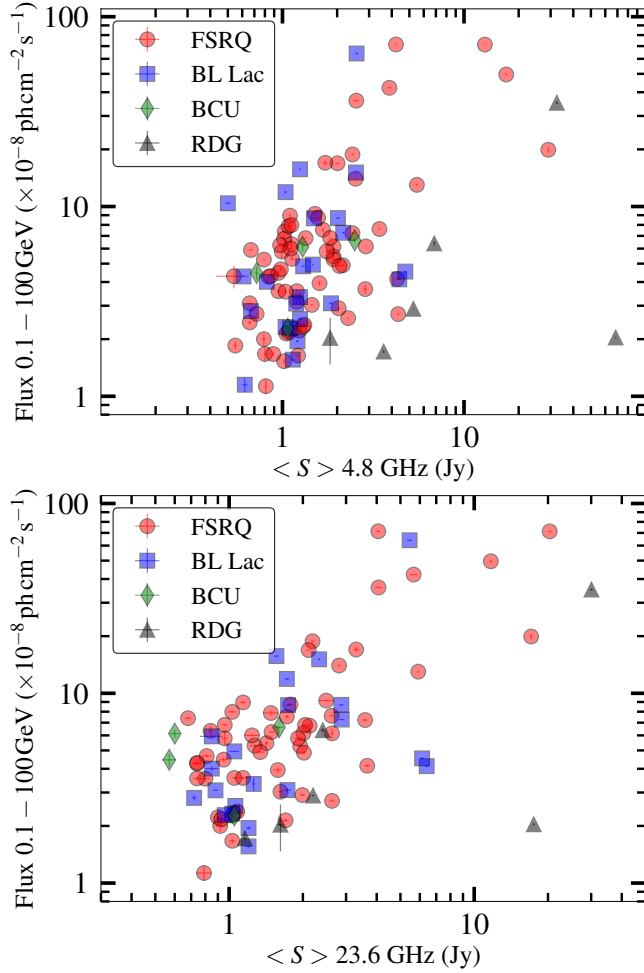


Figure 14. Relation between γ -ray flux and radio flux density at 4.8 GHz (top panel) and 23.6 GHz (bottom panel).

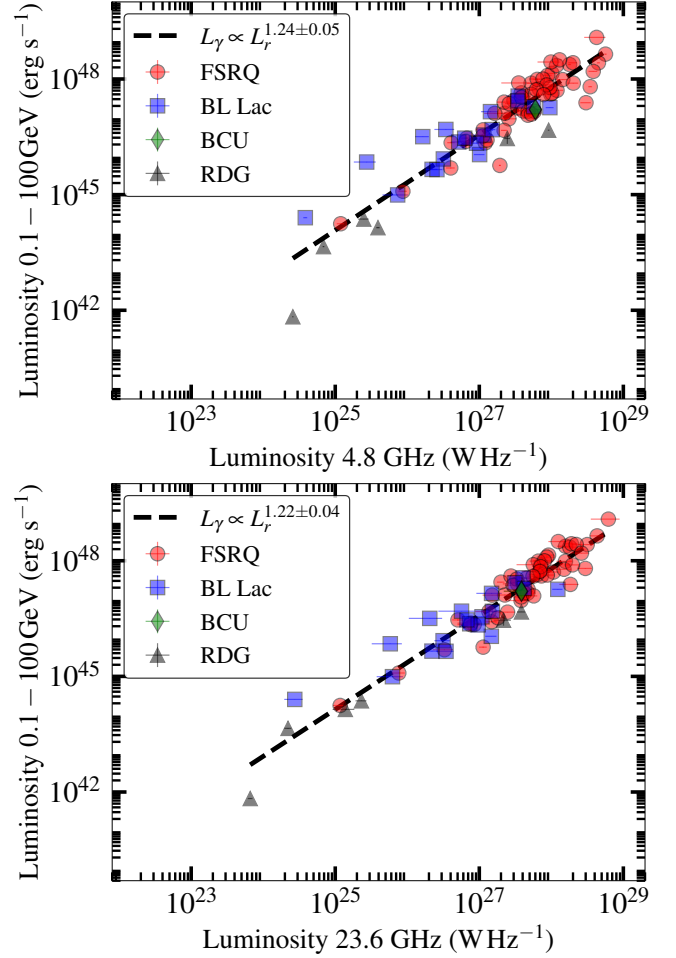


Figure 15. The relationship between γ -ray luminosity and radio luminosity is illustrated. The dashed line represents the fitted power-law relation between the two luminosities.

Figure 14 shows the γ -ray flux and radio flux density relation (top panel for 4.8 GHz and bottom panel for 23.6 GHz). The Kendall’s τ rank correlation coefficient is 0.29 with a p -value of 1.1×10^{-5} and 0.37 with a p -value of 3.6×10^{-7} for the cases of 4.8 and 23.6 GHz, respectively, thus confirming the correlation between these quantities. The γ -ray luminosities were calculated as explained in Section 2. The relation between γ -ray and radio luminosity is presented in Figure 15. A linear fit in log-log space gives $L_\gamma \propto L_r^{1.24 \pm 0.05}$ (Pearson correlation coefficient = 0.68) and $L_\gamma \propto L_r^{1.22 \pm 0.04}$ (Pearson correlation coefficient = 0.86) for radio luminosities of 4.8 and 23.6 GHz, respectively. Such a correlation could be induced by observational effects, which depend on the source distance (e.g., Böck et al. 2016).

Following the definition of γ -ray loudness in Böck et al. (2016) as the ratio of the total γ -ray flux to the radio flux density (S_γ/S_R), the distribution of γ -ray

loudness is shown in Figure 16 for both C and K band data. Taking into account the case of both frequency bands, the γ -ray loudness value ranges from ~ -9.53 to ~ -6.60 . It is noted that both FSRQ and BL Lac classes have a higher loudness factor compared to radio galaxies, and the value for BCUs falls between them. The mean value of γ -ray loudness for FSRQs and BL Lacs is at -7.46 ($\sigma = 0.30$) and -7.44 ($\sigma = 0.38$), respectively, in the C band case. For the K band, the mean values are -7.44 ($\sigma = 0.26$) and -7.50 ($\sigma = 0.33$) for FSRQs and BL Lacs, respectively.

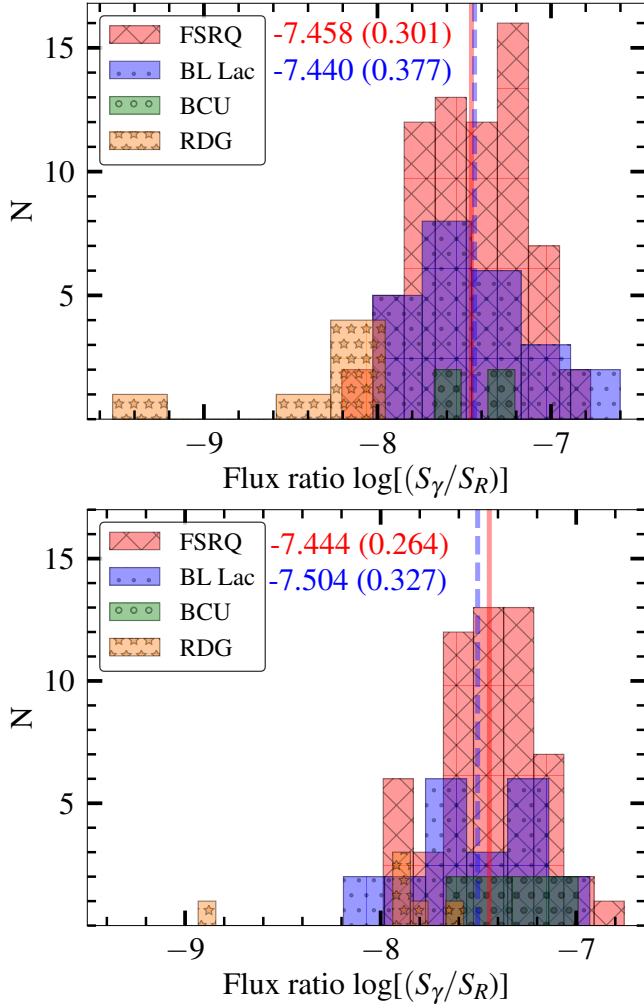


Figure 16. Top: distribution of the ratio between γ -ray flux and radio flux density (4.8 GHz). Bottom: distribution of the ratio between γ -ray flux and radio flux density (23.6 GHz). The transparent solid red and dashed blue vertical lines represent the average values with standard deviation inside parentheses for FSRQs and BL Lacs, respectively.

The distribution of the γ -ray loudness shows a similar dependence on the source class as the γ -ray spectral

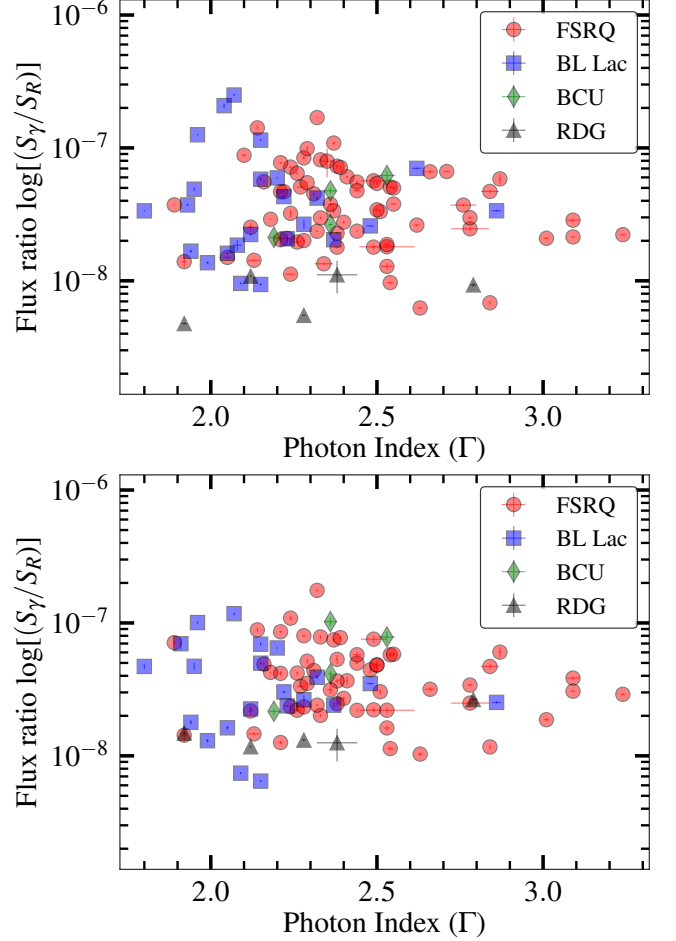


Figure 17. Scatter plot of γ -ray loudness and γ -ray spectral index using 4.8 GHz data (top panel) and 23.6 GHz data (bottom panel).

index distribution. Both BL Lacs and FSRQs have a wider distribution range; however, BL Lacs appear to have slightly higher γ -ray loudness factor compared to FSRQs. This relationship is consistent with shifts in the peak frequencies of the SEDs. When the synchrotron peak moves to higher frequencies, the radio-band flux density decreases. In contrast, a shift in the high-energy SED peak to higher frequencies increases the observed γ -ray flux and results in a more intense spectrum. This interpretation is further supported by the observed weak anticorrelation (Kendall τ rank correlation = -0.17 at 4.8 GHz and -0.19 at 23 GHz) between the γ -ray spectral index and the γ -ray loudness as shown in Figure 17. The weak anticorrelation observed here may be due to the consideration of the average γ -ray spectral index value calculated from the γ -ray monthly light curve taken from the *Fermi* LCR. This pattern is in agreement with the study reported by Böck et al. (2016) with

a strong anticorrelation (see Figure 9).

4. SUMMARY AND CONCLUSIONS

We present a first release of a dataset of 131 gamma-ray-loud AGNs monitored using the Nanshan 26-m Radio Telescope (NSRT) during the November 2016 to November 2024 period in the frequency band of 4.8 and 23.6 GHz. We summarize and conclude our findings as follows.

1. The main objective of the SMMAN program was primarily to offer essential multi-frequency radio monitoring at the lower frequency bands that complements the γ -ray observations conducted by *Fermi*-LAT along with the other multiband monitoring program and to investigate all pertinent aspects of radio physics of gamma-ray-loud AGNs.
2. The light curves presented here are unbinned, and each data point was subjected to proper post-measurement corrections, including Gaussian fitting, pointing calibration, atmospheric opacity, gain calibration, and absolute flux density calibration. The complete dataset has undergone a final quality check. The light curves of 131 SMMAN sources and three calibrator sources are presented in Figure 18 of Appendix B.
3. From the variability analysis, we find a trend in which sources show a higher degree of variability at 23.6 GHz than at 4.8 GHz, with BL Lacs exhibiting higher mean variability levels than FSRQs. BCUs and radio galaxies show lower variability compared to BL Lacs and FSRQs. In both frequency bands, FSRQs show higher radio luminosities than BL Lacs and other source classes. BCUs display radio luminosities intermediate between those of BL Lacs and FSRQs, while RDGs have lower luminosities, generally below the mean luminosity of FSRQs.
4. The radio spectral index indicates that BL Lac objects generally have flatter spectra, whereas FSRQs, BCUs, and RDGs span a wider range from flat to steep. At 4.8 and 23.6 GHz, about 90% of sources with $\alpha \geq -0.4$ display variability above 10%, predominantly among FSRQs and BL Lacs.

Sources with $\alpha \leq -0.4$, however, show little variability at either frequency.

5. The γ -ray loudness factor was estimated for different sources, and it was found that FSRQs and BL Lacs are louder than radio galaxies, whereas BCUs lie between these two populations. The distribution of γ -ray loudness exhibits a dependence on source class similar to that of the γ -ray spectral index distribution. In addition, a weak anticorrelation is observed between the γ -ray spectral index and the γ -ray loudness factor.
6. The data release of long-term light curve from this monitoring program in the lower frequency bands provides a unique coverage of the radio part of the SED and is a good addition to the other historical and ongoing programs covering the frequency range from low to high frequency bands.

The users utilizing the SMMAN radio data in their publications are kindly requested to acknowledge the source of the data by citing this paper. To use the data and for details, please contact Lang Cui (cuilang@xao.ac.cn).

ACKNOWLEDGEMENTS

We are thankful to Sándor Frey, Timur Mufakharov, and Junhui Fan for carefully reading the manuscript and providing insightful comments. This work was supported by the Tianshan Talent Training Program (grant No. 2023TSYCCX0099) and the National Key R&D Program of China (grant Nos. 2024YFA1611500 and 2022SKA0120102). This work was also partly supported by the Urumqi Nanshan Astronomy and Deep Space Exploration Observation and Research Station of Xinjiang (XJYWZ2303) and the Central Guidance for Local Science and Technology Development Fund (grant No. ZYYD2026JD01). The Nanshan 26-m Radio Telescope (NSRT) is operated by the Xinjiang Astronomical Observatory (XAO), CAS. This research has made use of the SIMBAD database, operated at CDS, Strasbourg, France. This research has made use of the NASA/IPAC Extragalactic Database (NED), which is operated by the Jet Propulsion Laboratory, California Institute of Technology, under contract with the National Aeronautics and Space Administration. This research has utilized the RATAN-600 data, provided by the Special Astrophysical Observatory of the Russian Academy of Sciences (SAO RAS).

APPENDIX

A. SOURCE SAMPLE

Table 3 lists all the sources included in the current data release. In Table 4, the information on whether the data for SMMAN sources is available in the other historical or the ongoing monitoring programs, such as UMRAO, F-GAMMA, RATAN-600, OVRO, ROBIN, MRO, and SMA, is provided with the corresponding name in that monitoring program.

Table 3. Information regarding the NSRT monitored sources in the SMMAN program.

Name 3FGL	Assoc. Name	Coordinates (J2000)		AGN Class	z	4.8 GHz		23.6 GHz	
		RA	Dec			N	$\langle S \rangle$ (Jy)	N	$\langle S \rangle$ (Jy)
(1)	(2)	(3)	(4)	(5)	(6)	(7)	(8)	(9)	(10)
J0012.4+7040	TXS 0008+704	00 11 31.90	+70 45 31.62	bcu	...	163	0.75 (0.25)	68	0.88 (0.30)
J0014.6+6119	4C +60.01	00 14 48.79	+61 17 43.54	bcu	...	226	1.97 (0.07)	52	0.83 (0.10)
J0059.6+0003	PKS 0056-00	00 59 05.51	+00 06 51.62	fsrq	0.719	100	1.39 (0.11)
J0102.8+5825	TXS 0059+581	01 02 45.76	+58 24 11.14	fsrq	0.644	227	2.43 (0.68)	227	3.59 (1.21)
J0108.7+0134	4C +01.02	01 08 38.77	+01 35 00.32	fsrq	2.099	146	3.88 (1.27)	157	5.66 (2.44)
J0110.2+6806	4C +67.04	01 10 12.87	+68 05 41.22	bll	0.290	173	0.89 (0.05)
J0130.8+1441	4C +14.06	01 29 55.35	+14 46 47.84	fsrq	1.630	39	0.57 (0.05)
J0137.0+4752	OC 457	01 36 58.59	+47 51 29.10	fsrq	0.859	201	1.91 (0.23)	171	2.63 (0.51)
J0205.0+1510	4C +15.05	02 04 50.41	+15 14 11.04	bcu	0.834	157	2.50 (0.42)	93	1.60 (0.69)
J0217.5+7349	S5 0212+73	02 17 30.81	+73 49 32.62	fsrq	2.346	211	3.42 (0.12)	226	2.62 (0.56)
J0221.1+3556	B0218+357	02 21 05.47	+35 56 13.72	FSRQ	0.944	124	1.03 (0.08)	15	0.68 (0.08)
J0222.6+4301	3C 66A	02 22 39.61	+43 02 07.80	BLL	0.370	5	0.85 (0.20)
J0237.9+2848	4C +28.07	02 37 52.41	+28 48 08.99	FSRQ	1.213	175	2.43 (0.44)	140	2.19 (0.46)
J0238.6+1636	AO 0235+164	02 38 38.93	+16 36 59.28	BLL	0.940	284	1.49 (0.48)	213	1.74 (0.45)
J0242.3+1059	OD 166	02 42 29.17	+11 01 00.73	fsrq	2.680	52	0.84 (0.04)	29	0.74 (0.18)
J0303.6+4716	4C +47.08	03 03 35.24	+47 16 16.27	bll	0.475	184	1.85 (0.58)	105	1.73 (0.64)
J0308.6+0408	NGC 1218	03 08 26.22	+04 06 39.30	rdg	0.028	144	3.61 (0.10)	83	1.16 (0.13)
J0319.8+4130	NGC 1275	03 19 48.16	+41 30 42.11	RDG	0.018	140	32.46 (5.45)	145	30.08 (5.15)
J0336.5+3210	NRAO 140	03 36 30.11	+32 18 29.34	fsrq	1.265	156	1.91 (0.22)	117	1.42 (0.23)
J0354.1+4643	B3 0350+465	03 54 30.01	+46 43 18.75	bcu	...	56	0.72 (0.13)	16	0.57 (0.15)
J0358.8+6002	TXS 0354+599	03 59 02.64	+60 05 22.07	fsrq	0.455	181	1.12 (0.09)	59	0.84 (0.14)
J0418.5+3813c	3C 111	04 18 21.28	+38 01 35.80	rdg	0.048	275	6.86 (0.39)	271	2.41 (0.81)
J0423.8+4150	4C +41.11	04 23 56.01	+41 50 02.71	bll	0.830	129	1.58 (0.24)	83	1.18 (0.22)
J0510.0+1802	PKS 0507+17	05 10 02.37	+18 00 41.58	fsrq	0.416	117	1.02 (0.12)	117	2.13 (0.42)
J0512.9+4038	B3 0509+406	05 12 52.54	+40 41 43.62	bcu	...	140	1.07 (0.21)	80	1.05 (0.33)
J0517.4+4540	4C +45.08	05 17 28.90	+45 37 04.86	FSRQ	0.839	101	0.79 (0.08)
J0519.3+2746	4C +27.15	05 19 33.02	+27 44 04.27	bcu	0.068	106	0.72 (0.04)
J0521.7+2113	TXS 0518+211	05 21 45.96	+21 12 51.45	bll	0.108	27	0.50 (0.09)
J0532.7+0732	OG 050	05 32 39.00	+07 32 43.34	FSRQ	1.254	125	1.67 (0.20)	95	1.72 (0.34)
J0533.2+4822	TXS 0529+483	05 33 15.86	+48 22 52.81	fsrq	1.160	105	1.13 (0.31)	68	1.27 (0.44)
J0603.8+2155	4C +22.12	06 03 51.56	+21 59 37.70	bcu	...	113	1.29 (0.05)	32	0.60 (0.15)
J0638.6+7324	S5 0633+73	06 39 21.96	+73 24 58.04	fsrq	1.850	161	0.99 (0.13)	121	0.96 (0.27)
J0710.5+4732	S4 0707+47	07 10 46.10	+47 32 11.14	bll	1.292	74	0.61 (0.06)
J0721.9+7120	S5 0716+71	07 21 53.45	+71 20 36.36	BLL	0.230	648	1.25 (0.27)	626	1.56 (0.80)
J0750.6+1232	OI 280	07 50 52.05	+12 31 04.83	fsrq	0.889	127	1.91 (0.32)	95	1.95 (0.41)
J0757.0+0956	PKS 0754+100	07 57 06.64	+09 56 34.85	bll	0.266	126	1.21 (0.22)	84	1.20 (0.26)
J0758.7+3747	NGC 2484	07 58 28.11	+37 47 11.81	rdg	0.041	103	1.22 (0.04)
J0805.4+6144	TXS 0800+618	08 05 18.18	+61 44 23.70	fsrq	3.018	66	0.66 (0.09)
J0809.5+4045	S4 0805+41	08 08 56.65	+40 52 44.89	fsrq	1.418	118	1.08 (0.14)	3	1.48 (0.18)
J0818.2+4223	S4 0814+42	08 18 16.00	+42 22 45.42	bll	0.530	120	1.30 (0.28)
J0824.9+5551	OJ 535	08 24 47.24	+55 52 42.67	fsrq	1.419	166	1.20 (0.13)
J0824.9+3916	4C +39.23	08 24 55.48	+39 16 41.91	fsrq	1.216	93	1.24 (0.08)	31	0.90 (0.24)
J0830.7+2408	OJ 248	08 30 52.09	+24 10 59.82	FSRQ	0.939	99	0.95 (0.11)	35	0.95 (0.22)

NOTE—The 3FGL name (Col. 1); an association (often more common) name (Col. 2); the coordinates in RA-Dec (Cols. 3 and 4); the AGN class (Col. 5) according to *Fermi* Large Area Telescope Fourth Source Catalog Data Release 4 (4FGL-DR4; Ballet et al. 2023) with designations in capital letters represent confirmed identifications, while those in lower case letters denote associations; the redshift (Col. 6) taken from NASA/IPAC Extragalactic Database (NED) and the SIMBAD astronomical database (Wenger et al. 2000); the number of observations in 4.8 and 23.6 GHz for each source (Col. 7 and 9), and the average flux density calculated over these observations (Col. 8 and 10).

Table 3. Continued.

Name 3FGL	Assoc. Name	Coordinates (J2000)		AGN Class	z	4.8 GHz		23.6 GHz	
		RA	Dec			<i>N</i>	$\langle S \rangle$ (Jy)	<i>N</i>	$\langle S \rangle$ (Jy)
(1)	(2)	(3)	(4)	(5)	(6)	(7)	(8)	(9)	(10)
J0832.6+4914	OJ 448	08 32 23.22	+49 13 21.04	bll	0.548	43	0.56 (0.10)
J0840.8+1315	3C 207	08 40 47.59	+13 12 23.56	ssrq	0.680	123	1.83 (0.17)	89	1.62 (0.43)
J0841.4+7053	0836+710	08 41 24.37	+70 53 42.17	FSRQ	2.213	889	2.88 (0.14)	776	2.01 (0.46)
J0854.8+2006	OJ 287	08 54 48.87	+20 06 30.64	BLL	0.306	138	4.40 (0.74)	126	6.40 (1.12)
J0903.1+4649	S4 0859+47	09 03 03.99	+46 51 04.14	fsrq	1.465	139	1.39 (0.08)	77	0.96 (0.23)
J0904.3+4240	S4 0900+42	09 04 15.63	+42 38 04.76	fsrq	1.342	61	0.85 (0.08)
J0909.1+0121	PKS 0906+01	09 09 10.09	+01 21 35.62	fsrq	1.023	86	1.60 (0.21)	77	1.58 (0.48)
J0916.3+3857	S4 0913+39	09 16 48.90	+38 54 28.15	fsrq	1.268	58	0.80 (0.06)
J0920.9+4442	S4 0917+44	09 20 58.46	+44 41 53.98	fsrq	2.188	123	1.34 (0.13)	132	2.04 (0.51)
J0921.8+6215	OK 630	09 21 36.23	+62 15 52.18	fsrq	1.458	172	1.10 (0.13)	77	1.14 (0.28)
J0948.6+4041	4C +40.24	09 48 55.34	+40 39 44.58	fsrq	1.250	112	1.22 (0.11)
J0957.6+5523	4C +55.17	09 57 38.18	+55 22 57.77	fsrq	0.901	159	1.83 (0.05)	55	0.96 (0.20)
J0957.4+4728	OK 492	09 58 19.67	+47 25 07.84	fsrq	1.884	115	1.16 (0.25)	38	1.03 (0.19)
J0958.6+6534	S4 0954+65	09 58 47.25	+65 33 54.82	BLL	0.369	542	1.04 (0.32)	565	1.72 (0.90)
J1023.1+3952	4C +40.25	10 23 11.57	+39 48 15.38	fsrq	1.254	86	0.72 (0.07)
J1033.2+4116	S4 1030+41	10 33 03.71	+41 16 06.23	fsrq	1.117	115	1.30 (0.45)	57	1.05 (0.26)
J1033.8+6051	S4 1030+61	10 33 51.43	+60 51 07.33	FSRQ	1.408	73	0.67 (0.13)
J1043.1+2407	B2 1040+24	10 43 09.04	+24 08 35.41	fsrq	0.562	84	0.79 (0.17)	74	0.92 (0.32)
J1044.4+8058	S5 1039+81	10 44 23.06	+80 54 39.44	fsrq	0.168	175	1.20 (0.16)	141	1.05 (0.22)
J1048.4+7144	S5 1044+71	10 48 27.62	+71 43 35.94	FSRQ	1.140	206	2.01 (0.71)	235	2.11 (0.64)
J1058.5+0133	4C +01.28	10 58 29.61	+01 33 58.82	BLL	0.894	106	4.75 (0.59)	93	6.13 (0.99)
J1128.0+5921	TXS 1125+596	11 28 13.34	+59 25 14.80	fsrq	1.799	159	1.08 (0.13)	109	0.93 (0.24)
J1131.4+3819	B2 1128+38	11 30 53.28	+38 15 18.55	fsrq	1.740	120	1.75 (0.31)	36	1.91 (0.47)
J1132.8+1015	4C +10.33	11 32 59.49	+10 23 42.26	FSRQ	0.540	16	0.45 (0.04)
J1145.1+1935	3C 264	11 45 05.01	+19 36 22.74	rdg	0.022	121	2.04 (0.06)
J1146.8+3958	S4 1144+40	11 46 58.30	+39 58 34.30	fsrq	1.088	121	1.51 (0.26)	12	2.49 (0.59)
J1153.4+4932	OM 484	11 53 24.47	+49 31 08.83	FSRQ	0.334	100	1.32 (0.18)	71	1.08 (0.34)
J1153.4+4033	B3 1151+408	11 53 54.66	+40 36 52.62	fsrq	0.925	225	1.02 (0.10)
J1159.5+2914	Ton 599	11 59 31.83	+29 14 43.83	fsrq	0.725	142	2.55 (1.09)	139	4.07 (1.69)
J1213.7+1306	4C +13.46	12 13 32.16	+13 07 20.56	fsrq	1.140	42	0.74 (0.06)
J1224.9+2122	4C +21.35	12 24 54.46	+21 22 46.39	FSRQ	0.434	122	2.15 (0.49)	81	1.34 (0.46)
J1229.1+0202	3C 273	12 29 06.70	+02 03 08.60	FSRQ	0.158	282	29.12 (0.85)	421	17.07 (2.17)
J1230.9+1224	M 87	12 30 49.42	+12 23 28.04	rdg	0.004	122	68.46 (1.35)	118	17.49 (1.32)
J1239.4+0727	PKS 1236+077	12 39 24.59	+07 30 17.19	bll	0.400	62	0.74 (0.11)
J1256.1-0547	3C 279	12 56 11.17	-05 47 21.52	FSRQ	0.536	178	13.03 (0.89)	335	20.32 (5.12)
J1258.1+3233	ON 393	12 57 57.23	+32 29 29.33	fsrq	0.806	42	0.66 (0.15)
J1302.6+5748	TXS 1300+580	13 02 52.47	+57 48 37.61	bll	0.950	43	0.62 (0.14)
J1309.5+1154	4C +12.46	13 09 33.93	+11 54 24.55	BLL	1.453	41	0.93 (0.07)	22	0.87 (0.12)
J1310.6+3222	OP 313	13 10 28.66	+32 20 43.78	fsrq	1.678	133	1.72 (0.60)	64	3.30 (0.69)
J1351.1+0030	PKS 1348+007	13 51 04.43	+00 31 19.40	fsrq	2.084	4	0.54 (0.22)
J1351.1+0030	OQ 530	14 19 46.60	+54 23 14.79	bll	0.152	124	1.25 (0.48)	71	1.06 (0.42)
J1442.6+5156	3C 303	14 43 02.78	+52 01 37.27	rdg	0.141	113	1.16 (0.05)	36	0.85 (0.19)
J1500.6+4750	TXS 1459+480	15 00 48.65	+47 51 15.54	bll	1.059	33	0.47 (0.09)
J1540.8+1449	4C +14.60	15 40 49.49	+14 47 45.88	bll	0.606	109	1.24 (0.23)
J1549.4+0237	PKS 1546+027	15 49 29.44	+02 37 01.16	fsrq	0.414	106	2.86 (0.61)

Table 3. Continued.

Name 3FGL	Assoc. Name	Coordinates (J2000)		AGN Class	z	4.8 GHz		23.6 GHz	
		RA	Dec			<i>N</i>	$\langle S \rangle$ (Jy)	<i>N</i>	$\langle S \rangle$ (Jy)
(1)	(2)	(3)	(4)	(5)	(6)	(7)	(8)	(9)	(10)
J1550.5+0526	4C +05.64	15 50 35.27	+05 27 10.45	fsrq	1.420	98	2.30 (0.08)
J1604.6+5714	GB6 J1604+5714	16 04 37.35	+57 14 36.66	fsrq	0.720	40	0.80 (0.25)
J1613.8+3410	OS 319	16 13 41.06	+34 12 47.91	fsrq	1.398	132	4.34 (0.72)	118	2.63 (0.79)
J1635.2+3809	4C +38.41	16 35 15.49	+38 08 04.50	FSRQ	1.814	120	2.53 (0.35)	105	2.81 (0.40)
J1637.7+4715	4C +47.44	16 37 45.13	+47 17 33.83	fsrq	0.735	91	0.89 (0.07)	34	1.03 (0.18)
J1637.9+5719	OS 562	16 38 13.46	+57 20 23.98	fsrq	0.751	144	1.45 (0.14)	127	1.62 (0.44)
J1640.6+3945	NRAO 512	16 40 29.63	+39 46 46.03	FSRQ	1.672	91	0.98 (0.15)	30	0.81 (0.20)
J1642.9+3950	3C 345	16 42 58.81	+39 48 36.99	FSRQ	0.593	313	5.50 (0.45)	437	5.91 (0.72)
J1653.9+3945	Mkn 501	16 53 52.22	+39 45 36.61	BLL	0.033	113	1.47 (0.09)	41	1.05 (0.30)
J1715.7+6837	S4 1716+68	17 16 13.94	+68 36 38.74	fsrq	0.777	55	0.55 (0.05)
J1727.1+4531	S4 1726+45	17 27 27.65	+45 30 39.73	fsrq	0.717	132	1.12 (0.32)	49	1.03 (0.27)
J1734.3+3858	B2 1732+38A	17 34 20.58	+38 57 51.44	fsrq	0.976	215	0.97 (0.20)	251	1.49 (0.56)
J1740.3+4736	S4 1738+47	17 39 57.13	+47 37 58.36	fsrq	...	95	0.81 (0.09)	25	0.79 (0.28)
J1740.3+5211	4C +51.37	17 40 36.98	+52 11 43.41	fsrq	1.381	123	1.11 (0.26)	42	1.24 (0.55)
J1748.6+7005	S4 1749+70	17 48 32.84	+70 05 50.77	bll	0.770	136	0.82 (0.21)	44	0.85 (0.33)
J1751.5+0939	OT 081	17 51 32.82	+09 39 00.73	bll	0.322	112	2.02 (0.46)	121	2.87 (0.64)
J1800.5+7827	S5 1803+784	18 00 45.68	+78 28 04.02	bll	0.691	170	2.54 (0.21)	183	2.33 (0.24)
J1801.5+4403	S4 1800+44	18 01 32.31	+44 04 21.90	fsrq	0.663	103	0.95 (0.20)	32	1.14 (0.40)
J1806.7+6949	3C 371	18 06 50.68	+69 49 28.11	fsrq	0.049	184	2.06 (0.25)	266	2.02 (0.42)
J1824.2+5649	4C +56.27	18 24 07.07	+56 51 01.49	bll	0.664	141	1.25 (0.13)	131	1.26 (0.21)
J1829.6+4844	3C 380	18 29 31.78	+48 44 46.16	css	0.692	132	5.26 (0.14)	127	2.20 (0.28)
J1849.2+6705	S4 1849+67	18 49 16.07	+67 05 41.68	FSRQ	0.657	136	1.05 (0.21)	124	1.70 (0.41)
J1927.7+6118	S4 1926+61	19 27 30.44	+61 17 32.88	bll	0.540	156	1.14 (0.23)	131	1.20 (0.38)
J2005.2+7752	S5 2007+77	20 05 30.93	+77 52 43.14	bll	0.342	146	1.04 (0.18)	68	1.03 (0.25)
J2007.3+6605	TXS 2007+659	20 07 28.77	+66 07 22.54	fsrq	1.325	133	0.86 (0.21)	39	0.74 (0.17)
J2010.3+7228	4C +72.28	20 09 52.30	+72 29 19.35	bll	...	161	1.10 (0.08)	117	0.96 (0.15)
J2022.5+7612	S5 2023+760	20 22 35.58	+76 11 26.17	bll	0.590	76	0.67 (0.07)	40	0.72 (0.11)
J2023.2+3154	4C +31.56	20 23 19.02	+31 53 02.31	bcu	0.356	136	1.48 (0.15)	36	1.13 (0.21)
J2025.2+3340	B2 2023+33	20 25 10.84	+33 43 00.21	bll	0.219	138	2.16 (0.42)	120	2.88 (0.77)
J2031.8+1223	PKS 2029+121	20 31 54.99	+12 19 41.34	bll	1.215	238	1.19 (0.12)	50	0.88 (0.13)
J2038.8+5113	3C 418	20 38 37.03	+51 19 12.66	fsrq	1.686	135	4.28 (0.26)	73	3.66 (0.84)
J2110.3+3540	B2 2107+35A	21 09 31.88	+35 32 57.60	bcu	0.202	136	2.25 (0.60)	112	2.49 (0.41)
J2123.6+0533	OX 036	21 23 44.52	+05 35 22.09	fsrq	1.940	165	2.04 (0.34)	96	1.99 (0.46)
J2201.7+5047	NRAO 676	22 01 43.54	+50 48 56.39	fsrq	1.899	102	0.79 (0.07)
J2202.7+4217	BL Lacertae	22 02 43.29	+42 16 39.98	BLL	0.067	457	2.56 (0.86)	371	5.45 (2.44)
J2203.7+3143	4C +31.63	22 03 14.98	+31 45 38.27	FSRQ	0.295	69	2.30 (0.34)
J2212.0+2355	PKS 2209+236	22 12 05.97	+23 55 40.54	fsrq	1.127	42	0.80 (0.17)	21	0.59 (0.11)
J2232.5+1143	CTA 102	22 32 36.41	+11 43 50.90	FSRQ	1.032	318	4.22 (0.33)	362	4.06 (1.11)
J2236.3+2829	B2 2234+28A	22 36 22.47	+28 28 57.41	fsrq	0.790	144	1.57 (0.20)	109	1.78 (0.41)
J2254.0+1608	3C 454.3	22 53 57.75	+16 08 53.56	FSRQ	0.859	336	17.08 (2.39)	448	11.69 (3.27)
J2321.9+2732	4C +27.50	23 21 59.86	+27 32 46.44	fsrq	1.255	138	1.23 (0.12)	103	1.44 (0.59)
J2330.5+1104	4C +10.73	23 30 40.85	+11 00 18.71	fsrq	1.501	103	1.04 (0.08)	24	0.74 (0.12)
J2354.1+4605	4C +45.51	23 54 21.68	+45 53 04.24	fsrq	1.992	97	1.11 (0.08)

Table 4. List of SMMAN sources overlapping with UMRAO, F-GAMMA, RATAN-600, OVRO, ROBIN, MRO and SMA.

SMMAN Source	UMRAO	F-GAMMA	RATAN-600	OVRO	ROBIN	MRO	SMA
(1)	(2)	(3)	(4)	(5)	(6)	(7)	(8)
TXS 0008+704
4C +60.01	0014+612
PKS 0056-00	5BZQJ0059+0006
TXS 0059+581	0059+581	J0102+5824	5BZUJ0102+5824	0059+581	...	0059+581	0102+584
4C +01.02	0106+013	J0108+0135	5BZQJ0108+0135	J0108+0135	...	0106+013	0108+015
4C +67.04	5BZUJ0110+6805	TB0110+6805
4C +14.06
OC 457	0133+476	J0136+4751	5BZQJ0136+4751	J0136+4751	...	0133+476	...
4C +15.05	0202+149	...	5BZUJ0204+1514	J0204+1514	0204+152
S5 0212+73	0212+735	J0217+734	5BZQJ0217+7349	J0217+7349	...	0212+735	0217+738
B2 0218+357	0218+357	J0221+3556	5BZUJ0221+3556	J0221+3556	...	0218+357	...
3C 66A	...	J0222+4302	5BZBJ0222+4302	3C 66A	0219+428	3C 66A	...
4C +28.07	0234+285	J0237+2848	5BZQJ0237+2848	J0237+2848	...	0234+285	0237+288
AO 0235+164	0235+164	J0238+1636	5BZBJ0238+1636	J0238+1636	0235+164	0235+164	0238+166
OD 166	J0242+1101	0242+110
4C +47.08	0300+470	J0303+4716	5BZBJ0303+4716	0300+471	0303+472
NGC 1218	NGC1218
NGC 1275	0316+413	J0319+4130	5BZUJ0319+4130	J0319+4130	0316+413	3C 84	0319+415
NRAO 140	0333+321	J0336+3218	5BZQJ0336+3218	0333+321	...	0333+321	0336+323
B3 0350+465	0354+467
TXS 0354+599	TXS0354+599
3C 111	0415+379	J0418+3801	...	0415+379	...	0415+379	0418+380
4C +41.11	5BZBJ0423+4150	TB0423+4150	0423+418
PKS 0507+17	...	J0510+1800	5BZQJ0510+1800	J0510+1800	...	0507+179	0510+180
B3 0509+406	B30509+406
4C +45.08	4C+45.08
4C +27.15
TXS 0518+211	...	J0521+2112	5BZBJ0521+2112	RGBJ0521+212	...
OG 050	0529+075	J0532+0732	5BZQJ0532+0732	J0532+0732	0532+075
TXS 0529+483	5BZQJ0533+4822	TXS0529+483	0533+483
4C +22.12
S5 0633+73	5BZQJ0639+7324	J0639+7324
S4 0707+47	0707+476	...	5BZBJ0710+4732	B30707+476	...	0707+476	0710+475
S5 0716+71	0716+714	J0721+7120	5BZBJ0721+7120	J0721+7120	0716+714	0716+714	0721+713
OI 280	0748+126	J0750+1231	5BZQJ0750+1231	J0750+1231	...	0748+126	0750+125
PKS 0754+100	0754+100	...	5BZBJ0757+0956	J0757+0956	...	0754+100	0757+099
NGC 2484	0755+379
TXS 0800+618	J0805+6144
S4 0805+41	0805+410	...	5BZQJ0808+4052	J0808+4052
S4 0814+42	0814+425	J0818+4222	...	J0818+4222	...	0814+425	0818+423
OJ 535	0820+560	J0824+5552	5BZQJ0824+5552	J0824+5552	...	0820+560	0824+558
4C +39.23	0821+394	...	5BZQJ0824+3916	J0824+3916	...	0821+394	0824+392
OJ 248	0827+243	J0830+2410	5BZQJ0830+2410	J0830+2410	0827+243	OJ 248	0830+241
OJ 448	0828+493	...	5BZBJ0832+4913	0828+493	...
3C 207	0838+133	...	5BZUJ0840+1312	3C 207	0838+133	...	3C207
0836+710	0836+710	J0841+7053	...	0836+710	0836+710	0836+710	...
OJ 287	0851+202	J0854+2006	5BZBJ0854+2006	J0854+2006	0851+202	OJ 287	0854+201
S4 0859+47	0859+470	...	5BZQJ0903+4651	S4 0859+47	...	0859+470	0903+468

NOTE—SMMAN program monitored sources name (Col. 1); Col. 2, Col. 3, Col. 4, Col. 5, Col. 6, Col. 7, and Col. 8 represent the corresponding name of SMMAN source in UMRAO, F-GAMMA, RATAN-600, OVRO, ROBIN, MRO, and SMA monitoring programs, respectively.

Table 4. Continued.

SMMAN Sources	UMRAO	F-GAMMA	RATAN-600	OVRO	ROBIN	MRO	SMA
(1)	(2)	(3)	(4)	(5)	(6)	(7)	(8)
S4 0900+42	S4 0900+42
PKS 0906+01	0906+015	J0909+0121	...	0909+013	0909+013
S4 0913+39	5BZQJ0916+3854	S40913+39
S4 0917+44	0917+449	J0920+4441	5BZQJ0920+4441	J0920+4441	...	0917+449	0920+446
OK 630	0917+624	...	5BZQJ0921+6215	J0921+6215	...	0921+622	0921+622
4C +40.24	0945+408	J0948+4039	...	0945+408	0948+406
4C +55.17	0954+556	C0957+5522	...	S4 0954+556	0957+553
OK 492	0955+476	...	5BZQJ0958+4725	J0958+4725	...	0958+474	0958+474
S4 0954+65	0954+658	J0958+6533	5BZBJ0958+6533	J0958+6533	0954+658	S4 0954+65	0958+655
4C +40.25	1020+400	...	5BZQJ1023+3948	J1023+3948
S4 1030+41	1030+415	...	5BZQJ1033+4116	J1033+4116	...	1030+415	...
S4 1030+61	...	J1033+6051	5BZQJ1033+6051	J1033+6051	1033+608
B2 1040+24	5BZQJ1043+2408	J1043+2408	...	TEX 1040+244	1043+241
S5 1039+81	J1044+8054	...	1039+811	1044+809
S5 1044+71	5BZUJ1048+7143	J1048+7143	1048+717
4C +01.28	1055+018	J1058+0133	5BZUJ1058+0133	J1058+0133	...	1055+018	1058+015
TXS 1125+596	...	J1128+5925	...	J1128+5925
B2 1128+38	1128+385	...	5BZQJ1130+3815	J1130+3815
4C +10.33
3C 264	3C 264
S4 1144+40	1144+402	...	5BZQJ1146+3958	J1146+3958	1146+399
OM 484	1150+497	...	5BZQJ1153+4931	OM484	...	1150+497	1153+495
B3 1151+408
Ton 599	1156+295	J1159+2914	5BZQJ1159+2914	J1159+2914	1156+295	4C 29.45	1159+292
4C +13.46	5BZQJ1213+1307	4C +13.46
4C +21.35	1222+216	J1224+2122	5BZQJ1224+2122	C1224+2122	1222+21	PKS 1222+216	1224+213
3C 273	1226+023	J1229+0203	5BZQJ1229+0203	J1229+0203	1226+023	3C 273	1229+020
M 87	...	J1230+1223	...	3C 274	...	3C 274	1230+123
PKS 1236+077	1236+077	...	5BZUJ1239+0730	J1239+0730	1239+075
3C 279	1256-057	J1256-0547	5BZQJ1256-0547	J1256-0547	1253-055	3C 279	1256-057
ON 393	J1257+3229
TXS 1300+580	5BZUJ1302+5748	J1302+5748	...	1300+580	...
4C +12.46	5BZBJ1309+1154	J1309+1154	...	MC 21307+12	1309+119
OP 313	1308+326	J1330+3220	5BZUJ1310+3220	J1310+3220	...	1308+326	1310+323
PKS 1348+007	5BZQJ1351+0031	PKS 1348+007
OQ 530	1418+546	...	5BZBJ1419+5423	J1419+5423	...	OQ 530	1419+543
3C 303	1441+522
TXS 1459+480	5BZQJ1500+4751	J1500+4751
4C +14.60	1538+149	...	5BZBJ1540+1447	J1540+1447	...	4C +14.60	1540+147
PKS 1546+027	1546+027	...	5BZQJ1549+0237	J1549+0237	...	1546+027	1549+026
4C +05.64	1548+056	J1550+0527	5BZQJ1550+0527	J1550+0527	...	1548+056	1550+054
GB6 J1604+5714	J1604+5714
OS 319	1611+343	J1613+3412	5BZQJ1613+3412	J1613+3412	1611+343	DA 406	1550+054
4C +38.41	1633+382	J1635+3808	5BZQJ1635+3808	J1635+3808	1633+382	4C +38.41	1635+381
4C +47.44	5BZQJ1637+4717	J1637+4717	1637+472
OS 562	1637+574	J1638+5720	...	J1638+5720	...	1637+574	1638+573
NRAO 512	1638+398	...	5BZQJ1640+3946	J1640+3946	...	1638+398	1640+397

Table 4. Continued.

SMMAN Sources	UMRAO	F-GAMMA	RATAN-600	OVRO	ROBIN	MRO	SMA
(1)	(2)	(3)	(4)	(5)	(6)	(7)	(8)
3C 345	1641+399	J1642+3948	5BZQJ1642+3948	J1642+3948	1641+399	3C 345	1642+398
Mkn 501	1652+398	J1653+3945	5BZBJ1653+3945	J1653+3945	1652+398	MARK 501	1653+397
S4 1716+68	J1716+6836	1716+686
S4 1726+45	1726+455	...	5BZQJ1727+4530	J1727+4530	1727+455
B2 1732+38A	1732+389	J1734+3857	1734+389
S4 1738+47	1738+476	...	5BZBJ1739+4737	J1739+4737
4C +51.37	1739+522	...	5BZQJ1740+5211	J1740+5211	...	S4 1739+52	1740+521
S4 1749+70	1749+701	J1748+7005	5BZBJ1748+7005	J1748+7005
OT 081	1749+096	J1751+0939	5BZBJ1751+0939	J1751+0939	...	PKS 1749+096	1751+096
S5 1803+784	1803+784	J1800+7828	5BZBJ1800+7828	J1800+7828	...	S5 1803+784	1800+784
S4 1800+44	1800+440	...	5BZQJ1801+4404	J1801+4404	1801+440
3C 371	1807+698	J1806+6949	5BZBJ1806+6949	J1806+6949	1807+698	3C 371	1806+698
4C +56.27	1823+568	J1824+5651	5BZBJ1824+5651	J1824+5651	...	4C 56.27	1824+568
3C 380	1828+487	...	5BZUJ1829+4844	3C 380	1828+487	1828+487	1829+487
S4 1849+67	...	J1849+6705	...	J1849+6705	...	J1849+6705	1849+670
S4 1926+61	1926+611	...	5BZBJ1927+6117	J1927+6117	1927+612
S5 2007+77	2007+777	J2005+7752	...	S52007+77	2005+778
TXS 2007+659	J2007+6607
4C +72.28	2010+723	...	5BZBJ2009+7229	J2009+7229	2009+724
S5 2023+760	5BZBJ2022+7611	J2022+7611
4C +31.56	2021+317	2023+318
B2 2023+33	3EGJ2027+3429	2025+337
PKS 2029+121	2029+121	J2031+1219	5BZUJ2031+1219	J2031+1219
3C 418	2037+511	2037+511	...	2037+511	2038+513
B2 2107+35A	2109+355
OX 036	2121+053	...	5BZQJ2123+0535	J2123+0535	...	2121+053	2123+055
NRAO 676	NRAO 676
BL Lacertae	2200+420	J2202+4216	5BZBJ2202+4216	BL Lacertae	2200+420	BL LAC	2202+422
4C +31.63	2201+315	J2203+3145	5BZQJ2203+3145	J2203+3145	...	2201+315	2203+317
PKS 2209+236	...	J2212+2355	5BZUJ2212+2355	J2212+2355
CTA 102	2230+114	J2232+1143	5BZQJ2232+1143	2230+114	2230+114	2230+114	2232+117
B2 2234+28A	2234+282	...	5BZQJ2236+2828	J2236+2828	...	2234+282	2236+284
3C 454.3	2251+158	J2253+1608	5BZQJ2253+1608	J2253+1608	2251+158	3C 454.3	2253+161
4C +27.50	2319+272	...	5BZQJ2321+2732	J2321+2732	2321+275
4C +10.73	2328+107	...	5BZQJ2330+1100	J2330+1100
4C +45.51	2351+456	...	5BZQJ2354+4553	2351+456	2354+458

Table 5. Variability and spectral indices of the SMMAN sources.

SMMAN source	F_{var}	23.6 GHz	4.8 GHz	V_S	23.6 GHz	$\alpha_{4.8-23.6}$	$F_{4.8}$	W	$F_{23.6}$	Flux (0.1–100 GeV)	LAT τ	L_γ (0.1–100 GeV)
(1)	(2)	(3)	(4)	(5)	(6)	(7)	(8)	(9)	(10)	(11)		(12)
TXS 0008+704	0.327 ± 0.003	0.308 ± 0.016	0.587 ± 0.014	0.512 ± 0.053	+0.178 ± 0.003 (-0.256, +0.638)
4C +60.01	0.020 ± 0.002	0.011 ± 0.014	0.063 ± 0.032	0.231 ± 0.078	-0.541 ± 0.003 (-0.676, -0.435)
PKS 0056-00	0.073 ± 0.003	...	0.168 ± 0.026
TXS 0059+581	0.270 ± 0.002	0.325 ± 0.006	0.599 ± 0.005	0.594 ± 0.028	+0.154 ± 0.001 (-0.087, +0.457)	2.57 (0.72) × 10 ²⁷	3.80 (1.28) × 10 ²⁷	7.23 ± 0.09	2.330 ± 0.002	(9.272 ± 0.118) × 10 ⁴⁶	...	(1.200 ± 0.001) × 10 ⁵⁰
4C +01.02	0.320 ± 0.003	0.420 ± 0.008	0.439 ± 0.012	0.647 ± 0.056	+0.006 ± 0.001 (-0.352, +0.280)	4.25 (1.39) × 10 ²⁸	6.20 (2.67) × 10 ²⁸	42.20 ± 0.03	2.370 ± 0.004	(1.200 ± 0.001) × 10 ⁵⁰
4C +67.04	0.046 ± 0.002	...	0.117 ± 0.031
4C +14.06	0.084 ± 0.005	...	0.138 ± 0.021
OC 457	0.115 ± 0.002	0.165 ± 0.008	0.269 ± 0.011	0.354 ± 0.043	+0.197 ± 0.001 (-0.149, +0.430)	3.45 (0.42) × 10 ²⁷	4.76 (0.92) × 10 ²⁷	6.15 ± 0.37	2.240 ± 0.002	(1.816 ± 0.110) × 10 ⁴⁷
4C +15.05	0.168 ± 0.002	0.422 ± 0.010	0.271 ± 0.014	0.529 ± 0.046	-0.373 ± 0.001 (-0.378, -0.128)	6.01 (1.01) × 10 ²⁷	3.85 (1.66) × 10 ²⁷	7.62 ± 0.12	2.360 ± 0.006	(1.614 ± 0.030) × 10 ⁴⁷
S5 0212+73	0.025 ± 0.002	0.184 ± 0.008	0.070 ± 0.024	0.305 ± 0.077	+0.107 ± 0.001 (-0.441, +0.108)	5.65 (2.02) × 10 ²⁸	4.33 (0.92) × 10 ²⁸	6.01 ± 0.08	3.240 ± 0.007	(4.414 ± 0.045) × 10 ⁴⁸
B2 0218+357	0.072 ± 0.003	0.067 ± 0.057	0.136 ± 0.023	0.061 ± 0.108	-0.268 ± 0.013 (-0.341, -0.199)	3.03 (0.24) × 10 ²⁷	2.00 (0.24) × 10 ²⁷	7.39 ± 0.09	2.240 ± 0.003	(2.783 ± 0.033) × 10 ⁴⁷
3C 66A	...	0.209 ± 0.055	...	0.152 ± 0.080
4C +28.07	0.181 ± 0.002	0.176 ± 0.011	0.294 ± 0.017	0.333 ± 0.089	-0.049 ± 0.001 (-0.351, +0.120)	1.02 (0.18) × 10 ²⁸	9.15 (1.92) × 10 ²⁷	18.80 ± 0.07	2.210 ± 0.004	(1.396 ± 0.003) × 10 ⁴⁸
AO 0235+164	0.319 ± 0.002	0.241 ± 0.007	0.723 ± 0.004	0.578 ± 0.022	+0.072 ± 0.001 (-0.330, +0.470)	3.47 (1.12) × 10 ²⁷	4.05 (1.05) × 10 ²⁷	8.66 ± 0.11	2.150 ± 0.003	(3.595 ± 0.045) × 10 ⁴⁷
OD 166	0.039 ± 0.004	0.203 ± 0.030	0.069 ± 0.021	0.406 ± 0.076	-0.184 ± 0.007 (-0.448, -0.056)	1.79 (0.09) × 10 ²⁸	1.58 (0.38) × 10 ²⁸	4.26 ± 0.08	2.540 ± 0.011	(2.376 ± 0.044) × 10 ⁴⁸
4C +47.08	0.312 ± 0.002	0.349 ± 0.013	0.498 ± 0.004	0.527 ± 0.042	-0.075 ± 0.001 (-0.260, +0.125)	1.16 (0.37) × 10 ²⁷	1.09 (0.40) × 10 ²⁷	3.09 ± 0.05	1.940 ± 0.003	(3.514 ± 0.061) × 10 ⁴⁶
NGC 1218	0.013 ± 0.004	0.046 ± 0.019	0.049 ± 0.026	0.163 ± 0.058	-0.176 ± 0.001 (-0.382, -0.036)	6.87 (0.19) × 10 ²⁴	2.21 (0.25) × 10 ²⁴	1.72 ± 0.03	1.920 ± 0.008	(4.480 ± 0.071) × 10 ⁴⁵
NGC 1275	0.166 ± 0.002	0.136 ± 0.010	0.192 ± 0.045	0.319 ± 0.067	-0.057 ± 0.001 (-0.180, +0.074)	2.49 (0.42) × 10 ²⁵	2.31 (0.40) × 10 ²⁵	35.20 ± 0.34	2.120 ± 0.001	(2.321 ± 0.023) × 10 ⁴⁴
NRAO 140	0.119 ± 0.002	0.122 ± 0.012	0.207 ± 0.012	0.259 ± 0.082	-0.202 ± 0.001 (-0.479, -0.014)	9.81 (1.13) × 10 ²⁷	7.29 (1.18) × 10 ²⁷	5.46 ± 0.17	3.090 ± 0.020	(4.031 ± 0.125) × 10 ⁴⁷
B3 0850+465	0.183 ± 0.004	0.219 ± 0.043	0.345 ± 0.028	0.386 ± 0.081	-0.170 ± 0.007 (-0.285, -0.037)	4.46 ± 0.35	2.530 ± 0.025
TXS 0354+599	0.074 ± 0.002	0.106 ± 0.022	0.148 ± 0.029	0.199 ± 0.092	-0.191 ± 0.003 (-0.365, -0.013)	6.73 (0.54) × 10 ²⁶	5.05 (0.84) × 10 ²⁶	6.34 ± 0.40	2.490 ± 0.038	(2.919 ± 0.186) × 10 ⁴⁶
3C 111	0.050 ± 0.002	0.319 ± 0.007	0.126 ± 0.028	0.604 ± 0.043	-0.696 ± 0.001 (-1.058, -0.073)	3.92 (0.22) × 10 ²⁵	1.38 (0.46) × 10 ²⁵	6.39 ± 0.18	2.790 ± 0.010	(1.380 ± 0.039) × 10 ⁴⁴
4C +41.11	0.151 ± 0.002	0.145 ± 0.016	0.298 ± 0.016	0.370 ± 0.043	-0.176 ± 0.001 (-0.350, +0.008)	3.35 (0.51) × 10 ²⁷	2.50 (0.47) × 10 ²⁷	6.75 ± 0.23	2.660 ± 0.014	(2.228 ± 0.077) × 10 ⁴⁶
PKS 0507+17	0.119 ± 0.003	0.160 ± 0.012	0.257 ± 0.024	0.283 ± 0.098	+0.437 ± 0.001 (+0.156, +0.884)	4.07 (0.48) × 10 ²⁶	8.50 (1.68) × 10 ²⁶	2.27 ± 0.10	2.190 ± 0.014
B3 0509+406	0.188 ± 0.003	0.297 ± 0.012	0.345 ± 0.018	0.469 ± 0.039	-0.030 ± 0.001 (-0.232, +0.263)
4C +45.08	0.092 ± 0.003	...	0.187 ± 0.015
4C +27.15	0.050 ± 0.003	...	0.119 ± 0.028
TXS 0518+211	0.167 ± 0.007	...	0.254 ± 0.022
OG 050	0.115 ± 0.002	0.167 ± 0.012	0.248 ± 0.017	0.374 ± 0.043	+0.063 ± 0.001 (-0.164, +0.321)	6.79 (0.81) × 10 ²⁷	7.00 (1.3) × 10 ²⁷	10.40 ± 0.11	2.040 ± 0.003	(3.350 ± 0.037) × 10 ⁴⁵
TXS 0529+483	0.271 ± 0.003	0.318 ± 0.018	0.588 ± 0.009	0.542 ± 0.059	+0.044 ± 0.002 (-0.252, +0.254)	4.03 (1.10) × 10 ²⁷	4.53 (1.5) × 10 ²⁷	7.54 ± 0.17	2.310 ± 0.003	(5.595 ± 0.129) × 10 ⁴⁷
4C +22.12	0.027 ± 0.003	0.199 ± 0.030	0.072 ± 0.018	0.312 ± 0.064	-0.477 ± 0.003 (-0.626, -0.182)	5.30 ± 0.09	2.210 ± 0.005	(3.507 ± 0.057) × 10 ⁴⁷
S5 0633+73	0.127 ± 0.002	0.254 ± 0.013	0.230 ± 0.018	0.420 ± 0.043	-0.021 ± 0.001 (-0.304, +0.287)	8.92 (1.17) × 10 ²⁷	8.65 (2.4) × 10 ²⁷	6.13 ± 0.31	2.36 ± 0.019
S4 0707+47	0.085 ± 0.004	...	0.193 ± 0.022	5.79 ± 0.47	2.870 ± 0.003	(1.243 ± 0.101) × 10 ⁴⁸
S5 0716+71	0.216 ± 0.001	0.497 ± 0.006	0.574 ± 0.013	0.838 ± 0.005	+0.176 ± 0.001 (-0.171, +0.724)	1.64 (0.35) × 10 ²⁶	2.05 (1.0) × 10 ²⁶	4.28 ± 0.04	2.620 ± 0.014	(3.070 ± 0.026) × 10 ⁴⁷
OJ 280	0.168 ± 0.002	0.182 ± 0.012	0.271 ± 0.016	0.290 ± 0.038	+0.032 ± 0.001 (-0.194, +0.237)	4.09 (0.69) × 10 ²⁷	4.18 (0.88) × 10 ²⁷	15.70 ± 0.12	1.960 ± 0.001	(3.196 ± 0.024) × 10 ⁴⁶
PKS 0754+100	0.182 ± 0.003	0.195 ± 0.012	0.367 ± 0.010	0.368 ± 0.065	+0.022 ± 0.001 (-0.155, +0.305)	2.21 (0.40) × 10 ²⁶	2.20 (0.48) × 10 ²⁶	5.27 ± 0.08	2.400 ± 0.003	(4.476 ± 0.023) × 10 ⁴⁷
NGC 2484	0.025 ± 0.003	...	0.074 ± 0.011	1.95 ± 0.03	2.050 ± 0.004	(4.520 ± 0.068) × 10 ⁴⁵
TXS 0800+618	0.138 ± 0.004	0.068 ± 0.086	0.219 ± 0.04	0.050 ± 0.064	+0.120 ± 0.026 (+0.067, +0.172)	5.25 (0.68) × 10 ²⁷	7.19 (0.88) × 10 ²⁷	2.45 ± 0.05	2.760 ± 0.039	(2.143 ± 0.048) × 10 ⁴⁸
S4 0805+41	0.124 ± 0.002	...	0.362 ± 0.023	7.87 ± 0.26	2.380 ± 0.003	(7.764 ± 0.260) × 10 ⁴⁷
S4 0814+42	0.213 ± 0.003	...	0.216 ± 0.019	4.84 ± 0.02	1.930 ± 0.003	(7.301 ± 0.026) × 10 ⁴⁶
OJ 535	0.101 ± 0.002	0.073 ± 0.077	0.216 ± 0.019	0.366 ± 0.066	-0.184 ± 0.003 (-0.473, +0.070)	5.79 (0.37) × 10 ²⁷	4.21 (1.12) × 10 ²⁷	3.15 ± 0.04	2.620 ± 0.008	(2.944 ± 0.035) × 10 ⁴⁷
4C +30.23	0.063 ± 0.003	0.224 ± 0.028	0.126 ± 0.035	0.366 ± 0.066	-0.184 ± 0.003 (-0.473, +0.070)	5.79 (0.37) × 10 ²⁷	4.21 (1.12) × 10 ²⁷	2.22 ± 0.04	2.380 ± 0.007	(1.450 ± 0.028) × 10 ⁴⁷
OJ 248	0.117 ± 0.003	0.194 ± 0.025	0.233 ± 0.023	0.413 ± 0.045	+0.038 ± 0.004 (-0.147, +0.421)	2.26 (0.26) × 10 ²⁷	2.26 (0.52) × 10 ²⁷	4.47 ± 0.11	2.840 ± 0.027	(1.200 ± 0.031) × 10 ⁴⁷
OJ 448	0.180 ± 0.005	...	0.274 ± 0.023
3C 207	0.091 ± 0.002	0.241 ± 0.012	0.215 ± 0.012	0.313 ± 0.062	-0.095 ± 0.001 (-0.268, +0.128)	2.45 (0.23) × 10 ²⁷	2.17 (0.58) × 10 ²⁷	2.03 ± 0.56	2.380 ± 0.061	(2.860 ± 0.788) × 10 ⁴⁶
0836+710	0.036 ± 0.001	0.198 ± 0.004	0.143 ± 0.03	0.526 ± 0.064	-0.220 ± 0.001 (-0.556, +0.064)	4.51 (0.22) × 10 ²⁸	3.15 (0.72) × 10 ²⁸	6.16 ± 0.02	3.090 ± 0.007	(2.626 ± 0.009) × 10 ⁴⁸
OJ 287	0.166 ± 0.002	0.143 ± 0.010	0.299 ± 0.011	0.299 ± 0.051	+0.249 ± 0.001 (+0.007, +0.496)	1.01 (0.17) × 10 ²⁷	1.47 (0.26) × 10 ²⁷	4.13 ± 0.02	2.150 ± 0.003	(1.095 ± 0.004) × 10 ⁴⁸
S1 0859+47	0.051 ± 0.002	0.194 ± 0.017	0.110 ± 0.017	0.370 ± 0.061	-0.214 ± 0.002 (-0.472, +0.118)	9.69 (0.56) × 10 ²⁷	6.69 (1.60) × 10 ²⁷

NOTE—SMMAN source name (same as the association name in Col. 2 of Table A) (Col. 1); fractional variability and variability index values for C and K band data sets (Col. 2, 3, 4, and 5); average radio spectral index and the range in spectral index (minimum and maximum values) inside the parenthesis (Col. 6); radio luminosity for each source (with measured redshift) in C and K band (Col. 7 and 8); the estimated *Fermi*-LAT flux, photon index and luminosity for each source (Col. 9, 10, and 11).

Table 5. Continued.

SMMAN source	F_{var}		V_S		$\alpha_{4.8-23.6}$	$P_{4.8}$	$P_{23.6}$	Flux (0.1–100 GeV) (10^{-9} ph cm $^{-2}$ s $^{-1}$)	LAT Γ (photon index)	L_γ (0.1–100 GeV) (erg s $^{-1}$)
	4.8 GHz (2)	23.6 GHz (3)	4.8 GHz (4)	23.6 GHz (5)						
S4 0900+42	0.095 ± 0.004	...	0.180 ± 0.026	3.94 ± 0.13	2.780 ± 0.057	(1.451 ± 0.049) × 10 ⁴⁷
PKS 0906+01	0.131 ± 0.003	0.275 ± 0.016	0.299 ± 0.009	0.412 ± 0.103	-0.039 ± 0.002 (-0.320, +0.281)	4.75 (0.62) × 10 ²⁷	4.69 (1.42) × 10 ²⁷	1.67 ± 0.13	2.230 ± 0.033	(1.364 ± 0.109) × 10 ⁴⁷
S4 0913+39	0.074 ± 0.004	...	0.130 ± 0.016	6.81 ± 0.01	2.270 ± 0.012	(2.245 ± 0.001) × 10 ⁴⁸
S4 0917+44	0.095 ± 0.002	0.226 ± 0.010	0.253 ± 0.015	0.500 ± 0.052	+0.257 ± 0.002 (-0.120, +0.531)	1.18 (0.11) × 10 ²⁸	1.80 (0.45) × 10 ²⁸	8.95 ± 0.13	2.330 ± 0.001	(9.771 ± 0.146) × 10 ⁴⁷
OK 630	0.113 ± 0.002	0.193 ± 0.019	0.205 ± 0.025	0.333 ± 0.083	-0.020 ± 0.002 (-0.315, +0.228)	6.38 (0.75) × 10 ²⁷	6.61 (1.62) × 10 ²⁷	1.64 ± 0.03	2.340 ± 0.028	(1.182 ± 0.019) × 10 ⁴⁷
4C +40.24	0.086 ± 0.003	...	0.160 ± 0.032	6.82 ± 0.06	1.890 ± 0.001	(4.012 ± 0.036) × 10 ⁴⁷
4C +55.17	0.012 ± 0.003	0.145 ± 0.024	0.028 ± 0.037	0.285 ± 0.108	-0.379 ± 0.003 (-0.547, -0.119)	5.24 (0.14) × 10 ²⁷	2.75 (0.37) × 10 ²⁷	2.27 ± 0.05	2.260 ± 0.013	(5.086 ± 0.118) × 10 ⁴⁷
OK 492	0.214 ± 0.002	0.122 ± 0.030	0.353 ± 0.017	0.265 ± 0.063	-0.123 ± 0.003 (-0.296, +0.014)	1.20 (0.20) × 10 ²⁸	1.07 (0.20) × 10 ²⁸	11.90 ± 0.13	2.150 ± 0.001	(4.909 ± 0.053) × 10 ⁴⁶
S4 0954+65	0.303 ± 0.002	0.506 ± 0.005	0.577 ± 0.008	0.850 ± 0.011	+0.306 ± 0.001 (-0.163, +0.806)	3.43 (1.05) × 10 ²⁶	5.66 (2.96) × 10 ²⁶	2.72 ± 0.00	2.550 ± 0.009	(1.812 ± 0.003) × 10 ⁴⁷
4C +40.25	0.086 ± 0.003	...	0.211 ± 0.020	2.33 ± 0.06	2.490 ± 0.005	(1.149 ± 0.032) × 10 ⁴⁷
S4 1030+41	0.344 ± 0.003	0.214 ± 0.019	0.507 ± 0.008	0.308 ± 0.083	-0.079 ± 0.001 (-0.237, +0.333)	4.73 (1.64) × 10 ²⁷	3.82 (0.95) × 10 ²⁷	5.90 ± 0.01	2.100 ± 0.006	(7.277 ± 0.010) × 10 ⁴⁷
S4 1030+61	0.192 ± 0.005	0.225 ± 0.058	0.352 ± 0.052	0.210 ± 0.067	2.00 ± 0.14	2.120 ± 0.009	(2.401 ± 0.172) × 10 ⁴⁶
B2 1040+24	0.208 ± 0.004	0.322 ± 0.017	0.355 ± 0.021	0.560 ± 0.053	+0.095 ± 0.002 (-0.143, +0.412)	6.54 (1.41) × 10 ²⁶	7.62 (2.65) × 10 ²⁶	3.58 ± 0.04	2.780 ± 0.007	(1.223 ± 0.014) × 10 ⁴⁵
S5 1039+81	0.128 ± 0.002	0.176 ± 0.011	0.280 ± 0.030	0.443 ± 0.069	-0.118 ± 0.001 (-0.408, +0.232)	8.70 (1.16) × 10 ²⁷	7.62 (1.60) × 10 ²⁷	16.90 ± 0.02	2.280 ± 0.005	(9.997 ± 0.014) × 10 ⁴⁷
S5 1044+71	0.351 ± 0.003	0.285 ± 0.007	0.649 ± 0.021	0.592 ± 0.039	-0.084 ± 0.001 (-0.331, +0.223)	7.64 (2.70) × 10 ²⁷	8.02 (2.43) × 10 ²⁷	4.54 ± 0.05	2.090 ± 0.002	(1.811 ± 0.018) × 10 ⁴⁷
4C +01.28	0.121 ± 0.003	0.112 ± 0.015	0.272 ± 0.015	0.260 ± 0.076	+0.149 ± 0.001 (-0.011, +0.273)	6.55 (1.19) × 10 ²⁷	1.23 (0.20) × 10 ²⁸	2.17 ± 0.02	2.280 ± 0.003	(4.255 ± 0.035) × 10 ⁴⁷
TXS 1125+596	0.122 ± 0.002	0.210 ± 0.015	0.286 ± 0.019	0.430 ± 0.089	-0.119 ± 0.001 (-0.271, +0.261)	1.02 (0.12) × 10 ²⁸	8.81 (2.27) × 10 ²⁷	5.80 ± 0.07	2.510 ± 0.003	(9.651 ± 0.123) × 10 ⁴⁷
B2 1128+38	0.174 ± 0.002	0.229 ± 0.015	0.302 ± 0.019	0.331 ± 0.059	-0.042 ± 0.004 (-0.195, +0.106)	1.44 (0.26) × 10 ²⁸	1.57 (0.39) × 10 ²⁸
4C +10.33	0.072 ± 0.009	...	0.109 ± 0.029
3C 264	0.016 ± 0.003	...	0.062 ± 0.018	9.15 ± 0.07	2.410 ± 0.002	(4.362 ± 0.032) × 10 ⁴⁷
S4 1144+40	0.173 ± 0.003	0.166 ± 0.060	0.474 ± 0.012	0.259 ± 0.094	+0.340 ± 0.007 (-0.112, +0.585)	3.83 (0.66) × 10 ²⁷	6.31 (1.50) × 10 ²⁷	2.38 ± 0.02	2.530 ± 0.083	(4.916 ± 0.142) × 10 ⁴⁵
OM 484	0.134 ± 0.003	0.283 ± 0.017	0.255 ± 0.031	0.491 ± 0.062	-0.107 ± 0.007 (-0.443, +0.166)	4.01 (0.55) × 10 ²⁶	3.28 (1.03) × 10 ²⁶	1.53 ± 0.04	2.050 ± 0.013	(7.083 ± 0.187) × 10 ⁴⁶
B3 1151+408	0.097 ± 0.002	...	0.191 ± 0.015	36.10 ± 0.16	2.140 ± 0.001	(7.898 ± 0.036) × 10 ⁴⁷
Tom 599	0.427 ± 0.004	0.406 ± 0.007	0.746 ± 0.004	0.834 ± 0.014	+0.094 ± 0.001 (-0.296, +0.402)	3.52 (1.50) × 10 ²⁷	5.62 (2.33) × 10 ²⁷	4.90 ± 0.05	2.380 ± 0.006	(2.206 ± 0.022) × 10 ⁴⁶
4C +13.46	0.078 ± 0.004	...	0.153 ± 0.020	19.90 ± 0.67	2.840 ± 0.001	(5.725 ± 0.194) × 10 ⁴⁵
4C +21.35	0.227 ± 0.002	0.316 ± 0.016	0.332 ± 0.015	0.502 ± 0.056	-0.294 ± 0.001 (-0.531, +0.004)	1.21 (0.28) × 10 ²⁷	7.56 (2.59) × 10 ²⁶	2.04 ± 0.02	2.100 ± 0.003	(6.776 ± 0.054) × 10 ⁴⁴
3C 273	0.017 ± 0.002	0.084 ± 0.006	0.065 ± 0.021	0.257 ± 0.073	-0.387 ± 0.001 (-0.497, -0.292)	1.93 (0.66) × 10 ²⁷	1.13 (0.14) × 10 ²⁷
M87	0.016 ± 0.003	0.077 ± 0.014	0.050 ± 0.015	0.102 ± 0.091	-0.851 ± 0.001 (-0.960, -0.725)	2.58 (0.05) × 10 ²⁴	6.60 (0.50) × 10 ²³
PKS 1236+077	0.145 ± 0.003	...	0.269 ± 0.019
3C 279	0.063 ± 0.002	0.237 ± 0.005	0.126 ± 0.036	0.424 ± 0.047	+0.146 ± 0.001 (-0.156, +0.413)	9.60 (0.66) × 10 ²⁷	1.50 (0.38) × 10 ²⁸	71.30 ± 0.17	2.290 ± 0.001	(5.997 ± 0.015) × 10 ⁴⁷
ON 393	0.222 ± 0.005	...	0.338 ± 0.021	3.09 ± 0.01	2.220 ± 0.005	(7.935 ± 0.028) × 10 ⁴⁶
TXS 1300+580	0.222 ± 0.004	...	0.412 ± 0.017	1.15 ± 0.10	2.080 ± 0.014	(5.424 ± 0.486) × 10 ⁴⁶
4C +12.46	0.076 ± 0.004	0.064 ± 0.045	0.142 ± 0.022	0.096 ± 0.102	-0.046 ± 0.011 (-0.110, +0.088)	5.48 (0.41) × 10 ²⁷	5.13 (0.71) × 10 ²⁷
OP 313	0.346 ± 0.003	0.192 ± 0.011	0.510 ± 0.022	0.665 ± 0.028	+0.255 ± 0.001 (-0.099, +0.384)	9.88 (3.45) × 10 ²⁷	1.90 (0.40) × 10 ²⁸	17.00 ± 0.53	2.290 ± 0.000	(2.758 ± 0.086) × 10 ⁴⁸
PKS 1348+007	0.398 ± 0.030	...	0.375 ± 0.038	4.29 ± 0.59	2.350 ± 0.022	(1.204 ± 0.166) × 10 ⁴⁸
OQ 530	0.382 ± 0.003	0.371 ± 0.016	0.625 ± 0.006	0.652 ± 0.019	-0.100 ± 0.002 (-0.430, +0.125)	7.35 (2.82) × 10 ²⁵	6.23 (2.47) × 10 ²⁵	2.55 ± 0.05	2.370 ± 0.002	(9.819 ± 0.206) × 10 ⁴⁴
3C 303	0.082 ± 0.003	0.171 ± 0.029	0.101 ± 0.025	0.210 ± 0.102	-0.240 ± 0.002 (-0.354, +0.011)	5.95 (0.26) × 10 ²⁵	4.36 (0.97) × 10 ²⁵
TXS 1450+480	0.183 ± 0.006	...	0.357 ± 0.016
4C +14.60	0.186 ± 0.003	...	0.376 ± 0.016
PKS 1516+027	0.213 ± 0.003	...	0.339 ± 0.029	3.67 ± 0.20	2.530 ± 0.018	(1.293 ± 0.069) × 10 ⁴⁶
4C +05.64	0.028 ± 0.003	...	0.076 ± 0.019	2.58 ± 0.02	2.240 ± 0.015	(2.803 ± 0.017) × 10 ⁴⁷
GB6 J1604+5714	...	0.272 ± 0.027	...	0.412 ± 0.075	3.55 ± 0.15	2.480 ± 0.001	(5.402 ± 0.230) × 10 ⁴⁶
OS 319	0.164 ± 0.002	0.276 ± 0.012	0.269 ± 0.012	0.525 ± 0.052	-0.324 ± 0.001 (-0.554, -0.069)	3.03 (0.50) × 10 ²⁸	1.84 (0.35) × 10 ²⁸	2.71 ± 0.01	2.630 ± 0.007	(2.428 ± 0.007) × 10 ⁴⁷
4C +38.41	0.135 ± 0.002	0.099 ± 0.012	0.234 ± 0.020	0.290 ± 0.079	+0.073 ± 0.001 (-0.143, +0.299)	2.00 (0.28) × 10 ²⁸	2.22 (0.32) × 10 ²⁸	14.00 ± 0.02	2.440 ± 0.003	(2.638 ± 0.004) × 10 ⁴⁸
4C +47.44	0.078 ± 0.003	0.096 ± 0.037	0.174 ± 0.026	0.176 ± 0.119	+0.074 ± 0.003 (-0.079, +0.230)	1.28 (0.10) × 10 ²⁷	1.48 (0.26) × 10 ²⁷	1.67 ± 0.05	2.530 ± 0.010	(2.611 ± 0.072) × 10 ⁴⁶
OS 362	0.091 ± 0.002	0.245 ± 0.011	0.208 ± 0.011	0.389 ± 0.076	+0.043 ± 0.001 (-0.246, +0.429)	2.21 (0.21) × 10 ²⁷	2.47 (0.67) × 10 ²⁷	3.63 ± 0.03	3.010 ± 0.008	(4.642 ± 0.051) × 10 ⁴⁶
NRAO 512	0.153 ± 0.003	0.193 ± 0.029	0.339 ± 0.019	0.303 ± 0.089	-0.186 ± 0.005 (-0.306, -0.032)	8.62 (1.32) × 10 ²⁷	7.13 (1.76) × 10 ²⁷	4.67 ± 0.16	2.440 ± 0.012	(7.043 ± 0.152) × 10 ⁴⁷

B. RADIO LIGHT CURVES OF INDIVIDUAL
SOURCES MONITORED IN SMMAN
PROGRAM

Figure 18 of Appendix B presents the light curves for all the 131 SMMAN sources and the three calibrator sources in the program at 4.8 and 23.6 GHz. The data points shown here are unbinned. For some sources, either 4.8 GHz or 23.6 GHz light curves are available; accordingly, those are presented.

REFERENCES

- Abdo, A. A., Ackermann, M., Ajello, M., et al. 2010a, *Nature*, 463, 919, doi: [10.1038/nature08841](https://doi.org/10.1038/nature08841)
- Abdo, A. A., Ackermann, M., Agudo, I., et al. 2010b, *ApJ*, 716, 30, doi: [10.1088/0004-637X/716/1/30](https://doi.org/10.1088/0004-637X/716/1/30)
- Abdollahi, S., Acero, F., Ackermann, M., et al. 2020, *ApJS*, 247, 33, doi: [10.3847/1538-4365/ab6bcb](https://doi.org/10.3847/1538-4365/ab6bcb)
- Abdollahi, S., Ajello, M., Baldini, L., et al. 2023, *ApJS*, 265, 31, doi: [10.3847/1538-4365/acbb6a](https://doi.org/10.3847/1538-4365/acbb6a)
- Acero, F., Ackermann, M., Ajello, M., et al. 2015, *ApJS*, 218, 23, doi: [10.1088/0067-0049/218/2/23](https://doi.org/10.1088/0067-0049/218/2/23)
- Ackermann, M., Ajello, M., Allafort, A., et al. 2011, *ApJ*, 743, 171, doi: [10.1088/0004-637X/743/2/171](https://doi.org/10.1088/0004-637X/743/2/171)
- Ackermann, M., Ajello, M., Atwood, W. B., et al. 2015, *ApJ*, 810, 14, doi: [10.1088/0004-637X/810/1/14](https://doi.org/10.1088/0004-637X/810/1/14)
- Ajello, M., Angioni, R., Axelsson, M., et al. 2020, *ApJ*, 892, 105, doi: [10.3847/1538-4357/ab791e](https://doi.org/10.3847/1538-4357/ab791e)
- Aller, H. D., Aller, M. F., Latimer, G. E., & Hodge, P. E. 1985, *ApJS*, 59, 513, doi: [10.1086/191083](https://doi.org/10.1086/191083)
- Aller, M. F., Aller, H. D., & Hughes, P. A. 1992, *ApJ*, 399, 16, doi: [10.1086/171898](https://doi.org/10.1086/171898)
- . 2017, *Galaxies*, 5, 75, doi: [10.3390/galaxies5040075](https://doi.org/10.3390/galaxies5040075)
- Aller, M. F., Hughes, P. A., Aller, H. D., Hovatta, T., & Ramakrishnan, V. 2016, *Galaxies*, 4, 35, doi: [10.3390/galaxies4040035](https://doi.org/10.3390/galaxies4040035)
- Aller, M. F., Hughes, P. A., Aller, H. D., Latimer, G. E., & Hovatta, T. 2014, *ApJ*, 791, 53, doi: [10.1088/0004-637X/791/1/53](https://doi.org/10.1088/0004-637X/791/1/53)
- Angelakis, E., Fuhrmann, L., Nestoras, I., et al. 2010, arXiv e-prints, arXiv:1006.5610, doi: [10.48550/arXiv.1006.5610](https://doi.org/10.48550/arXiv.1006.5610)
- Angelakis, E., Fuhrmann, L., Marchili, N., et al. 2015, *A&A*, 575, A55, doi: [10.1051/0004-6361/201425081](https://doi.org/10.1051/0004-6361/201425081)
- Angelakis, E., Fuhrmann, L., Myserlis, I., et al. 2019, *A&A*, 626, A60, doi: [10.1051/0004-6361/201834363](https://doi.org/10.1051/0004-6361/201834363)
- Atwood, W. B., Abdo, A. A., Ackermann, M., et al. 2009, *ApJ*, 697, 1071, doi: [10.1088/0004-637X/697/2/1071](https://doi.org/10.1088/0004-637X/697/2/1071)
- Baars, J. W. M., Genzel, R., Pauliny-Toth, I. I. K., & Witzel, A. 1977, *A&A*, 61, 99
- Bach, U., Raiteri, C. M., Villata, M., et al. 2007, *A&A*, 464, 175, doi: [10.1051/0004-6361:20066561](https://doi.org/10.1051/0004-6361:20066561)
- Ballet, J., Bruel, P., Burnett, T. H., Lott, B., & The Fermi-LAT collaboration. 2023, arXiv e-prints, arXiv:2307.12546, doi: [10.48550/arXiv.2307.12546](https://doi.org/10.48550/arXiv.2307.12546)
- Blandford, R. D., & Königl, A. 1979, *ApJ*, 232, 34, doi: [10.1086/157262](https://doi.org/10.1086/157262)
- Blandford, R. D., & Rees, M. J. 1978, in *BL Lac Objects*, ed. A. M. Wolfe, 328–341
- Blinov, D., Jorstad, S. G., Larionov, V. M., et al. 2021, *MNRAS*, 505, 4616, doi: [10.1093/mnras/stab1484](https://doi.org/10.1093/mnras/stab1484)
- Böck, M., Kadler, M., Müller, C., et al. 2016, *A&A*, 590, A40, doi: [10.1051/0004-6361/201424773](https://doi.org/10.1051/0004-6361/201424773)
- Boettcher, M. 2004, in *ESA Special Publication*, Vol. 552, *Proceedings of the 5th INTEGRAL Workshop on the INTEGRAL Universe*, 16–20 February 2004, Munich, Germany., ed. V. Schoenfelder, G. Lichti, & C. Winkler, 543
- Böttcher, M. 2019, *Galaxies*, 7, 20, doi: [10.3390/galaxies7010020](https://doi.org/10.3390/galaxies7010020)
- Buson, S., Tramacere, A., Pfeiffer, L., et al. 2022, *ApJL*, 933, L43, doi: [10.3847/2041-8213/ac7d5b](https://doi.org/10.3847/2041-8213/ac7d5b)
- Carnerero, M. I., Raiteri, C. M., Villata, M., et al. 2015, *MNRAS*, 450, 2677, doi: [10.1093/mnras/stv823](https://doi.org/10.1093/mnras/stv823)
- Casaburo, F., Ciprini, S., Gasparrini, D., & Giacchino, F. 2025, *Particles*, 8, doi: [10.3390/particles8010017](https://doi.org/10.3390/particles8010017)
- Di Gesu, L., Marshall, H. L., Ehlert, S. R., et al. 2023, *Nature Astronomy*, 7, 1245, doi: [10.1038/s41550-023-02032-7](https://doi.org/10.1038/s41550-023-02032-7)
- Fan, J.-H. 2005, *Chinese Journal of Astronomy and Astrophysics Supplement*, 5, 213
- Fan, J. H., Yang, J. H., Liu, Y., et al. 2016, *ApJS*, 226, 20, doi: [10.3847/0067-0049/226/2/20](https://doi.org/10.3847/0067-0049/226/2/20)
- Foschini, L., Bonnoli, G., Ghisellini, G., et al. 2013, *A&A*, 555, A138, doi: [10.1051/0004-6361/201321675](https://doi.org/10.1051/0004-6361/201321675)
- Fossati, G., Maraschi, L., Celotti, A., Comastri, A., & Ghisellini, G. 1998, *MNRAS*, 299, 433, doi: [10.1046/j.1365-8711.1998.01828.x](https://doi.org/10.1046/j.1365-8711.1998.01828.x)

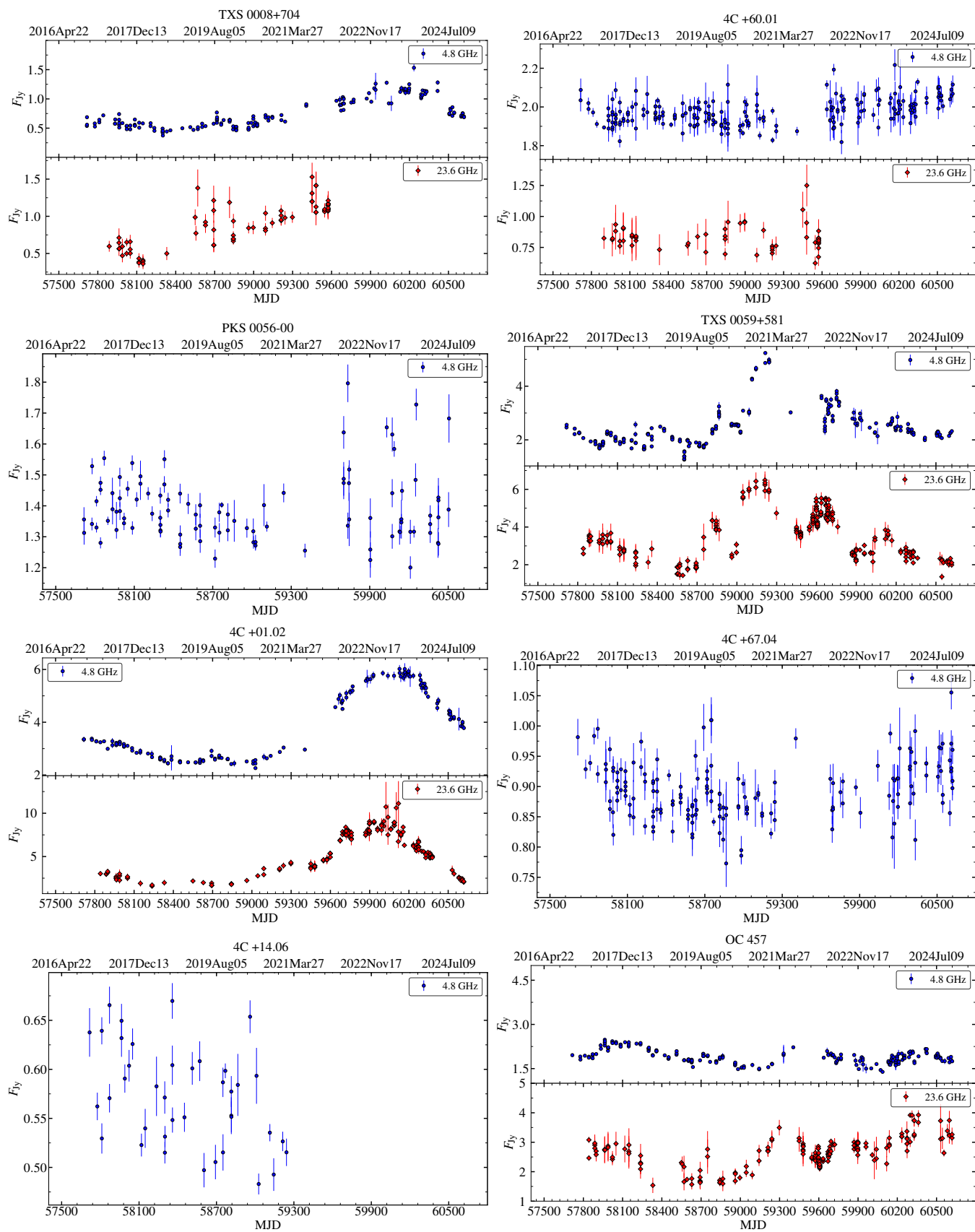


Figure 18. Light curves of the sources monitored by the SMMAN program at 4.8 GHz and 23.6 GHz.

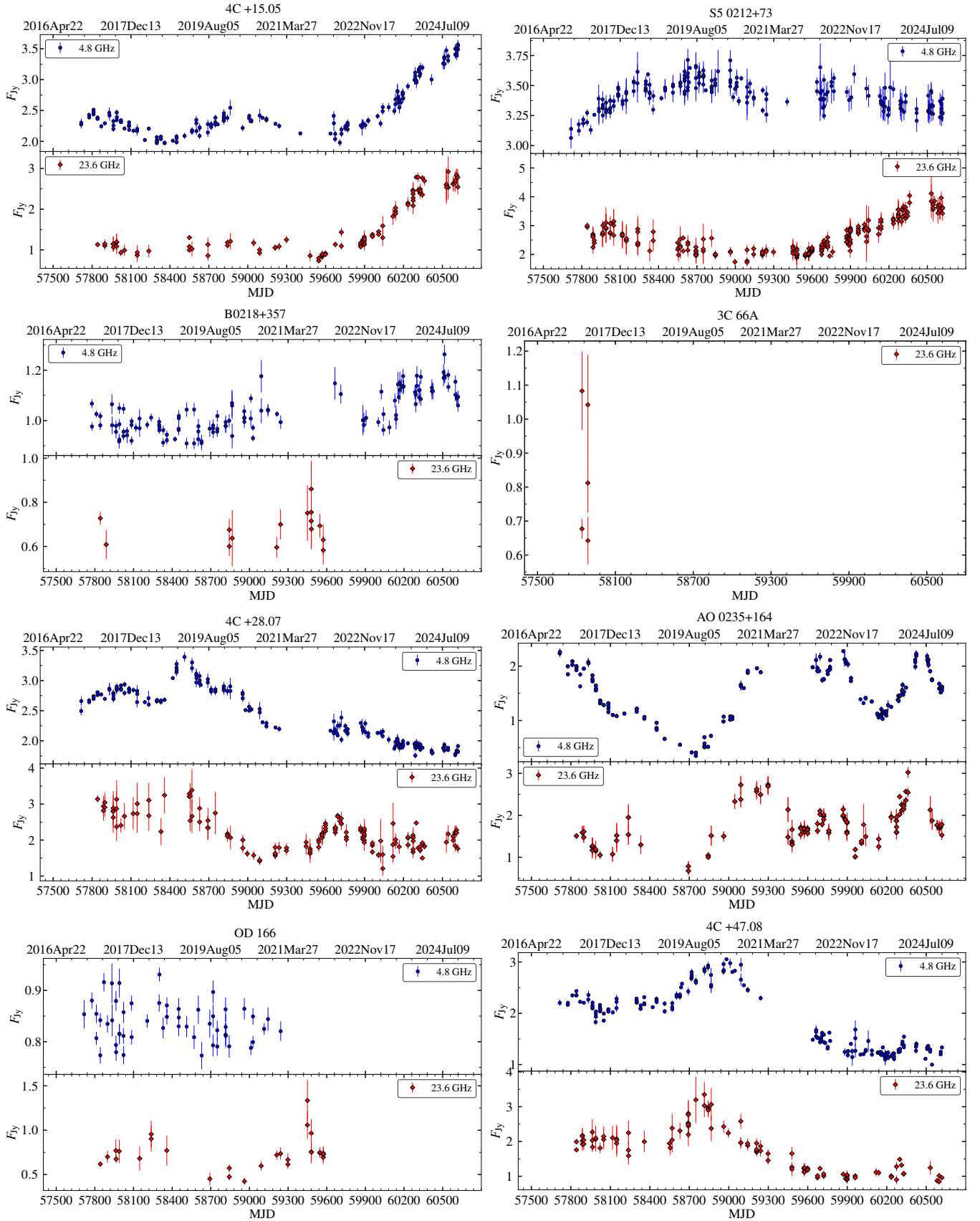


Figure 18. Continued.

Figure 18. Continued.

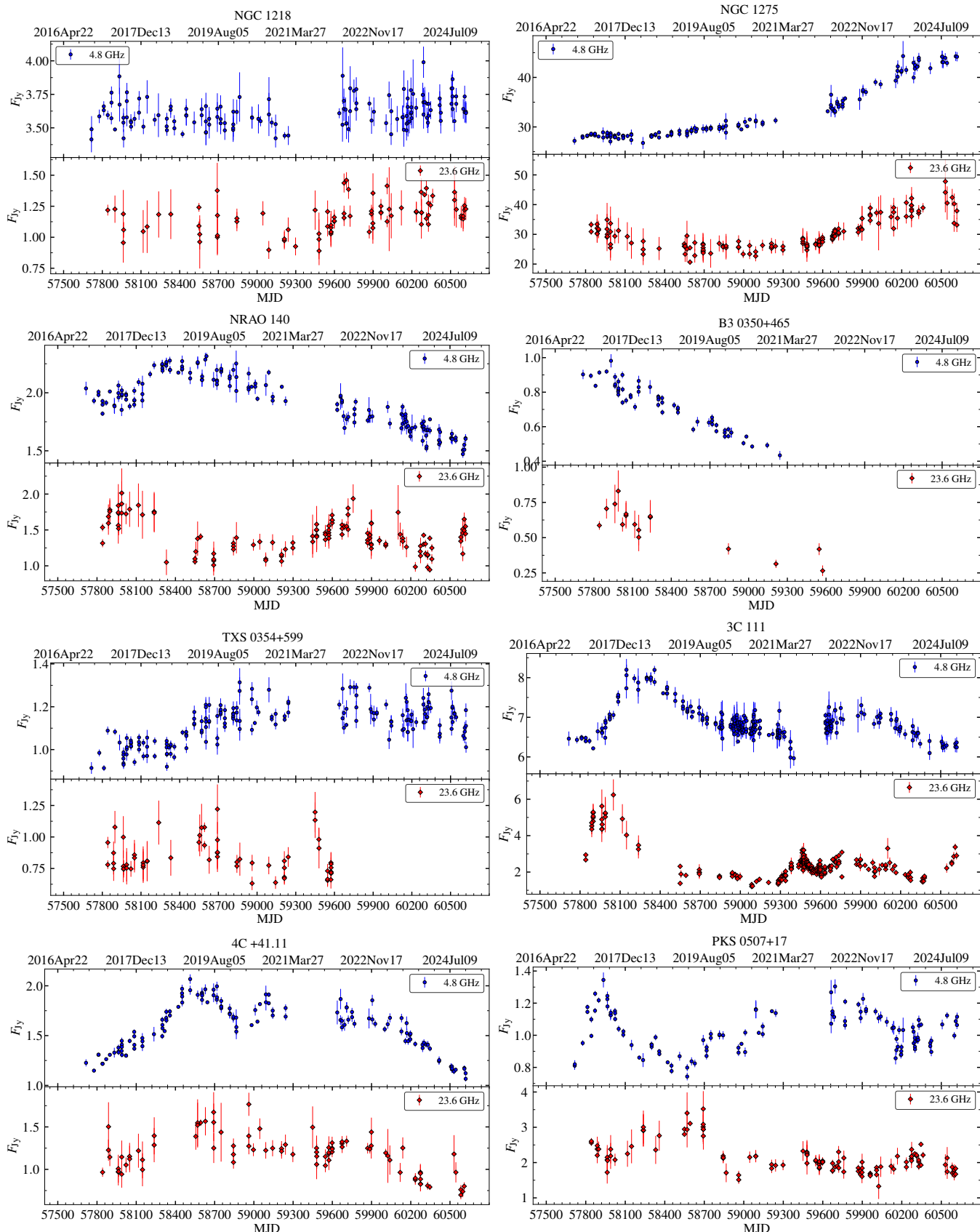


Figure 18. Continued.

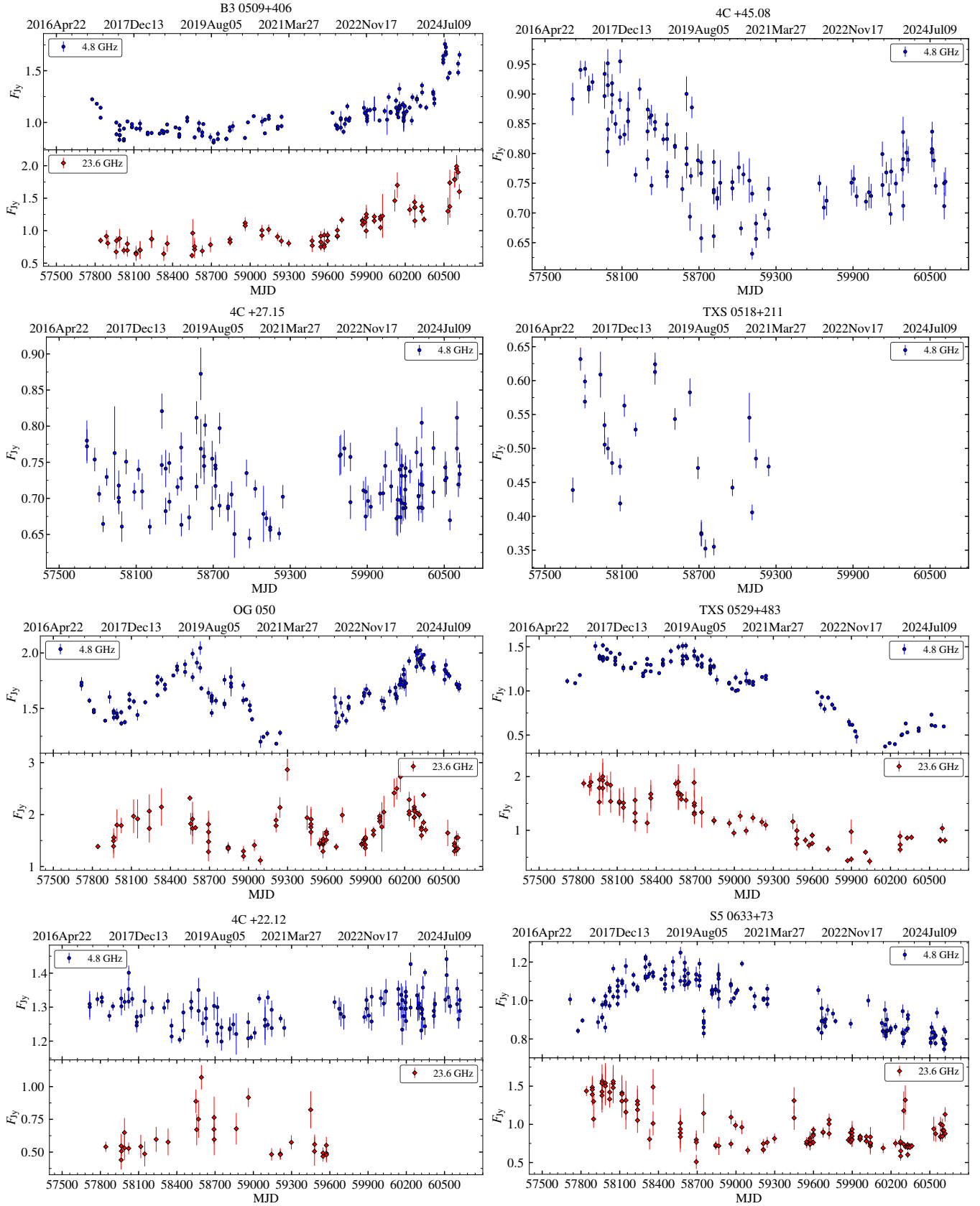


Figure 18. Continued.

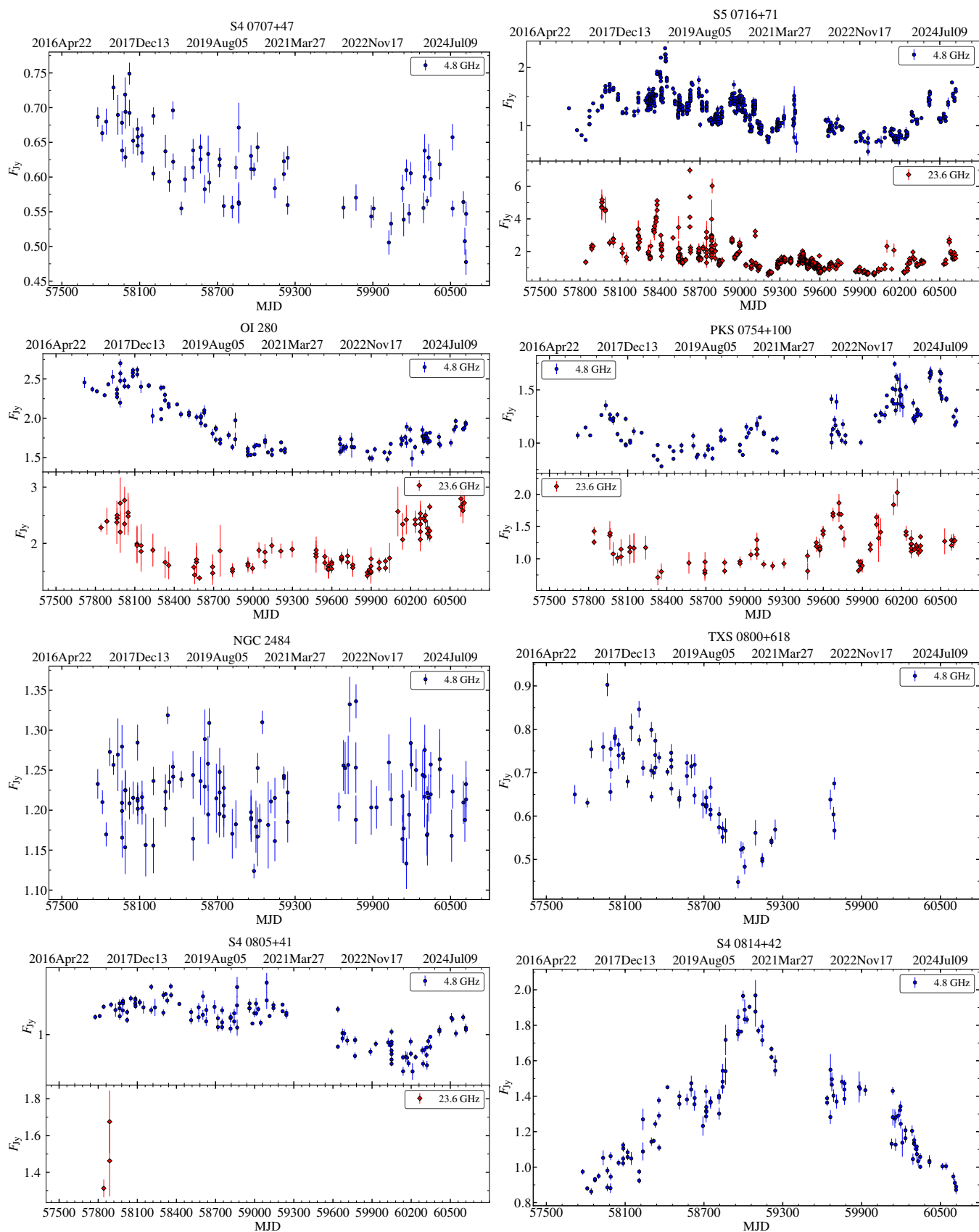


Figure 18. Continued.

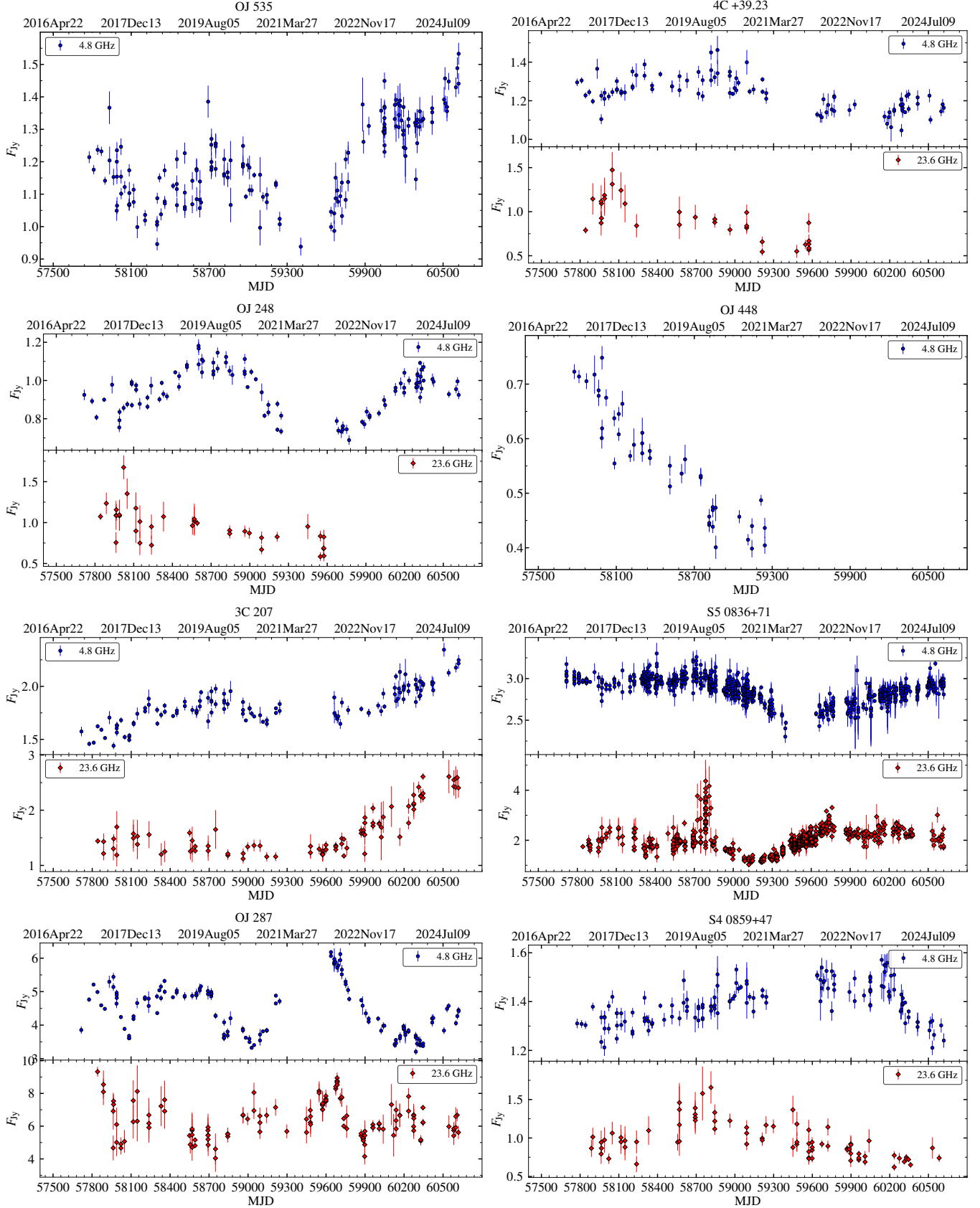


Figure 18. Continued.

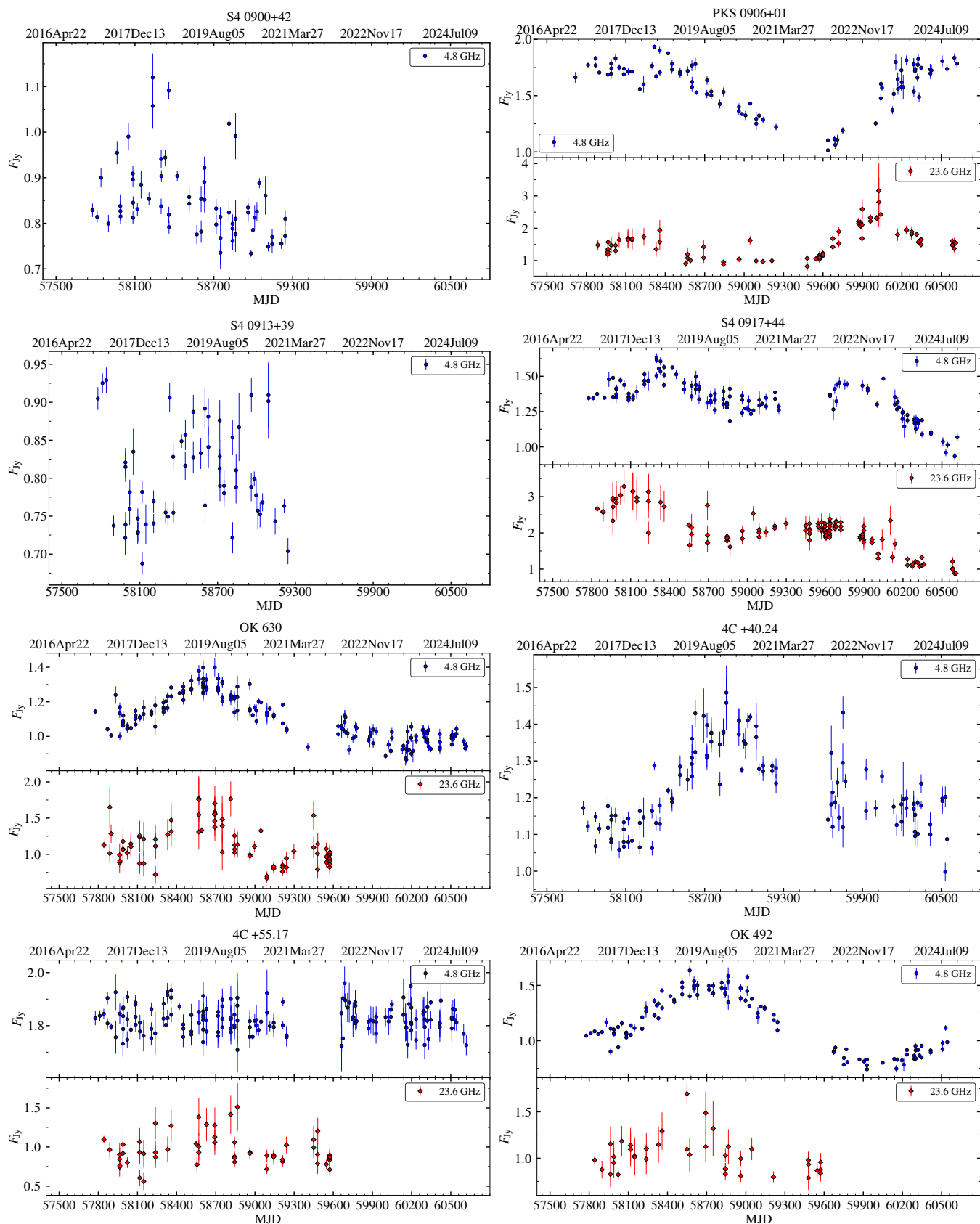


Figure 18. Continued.

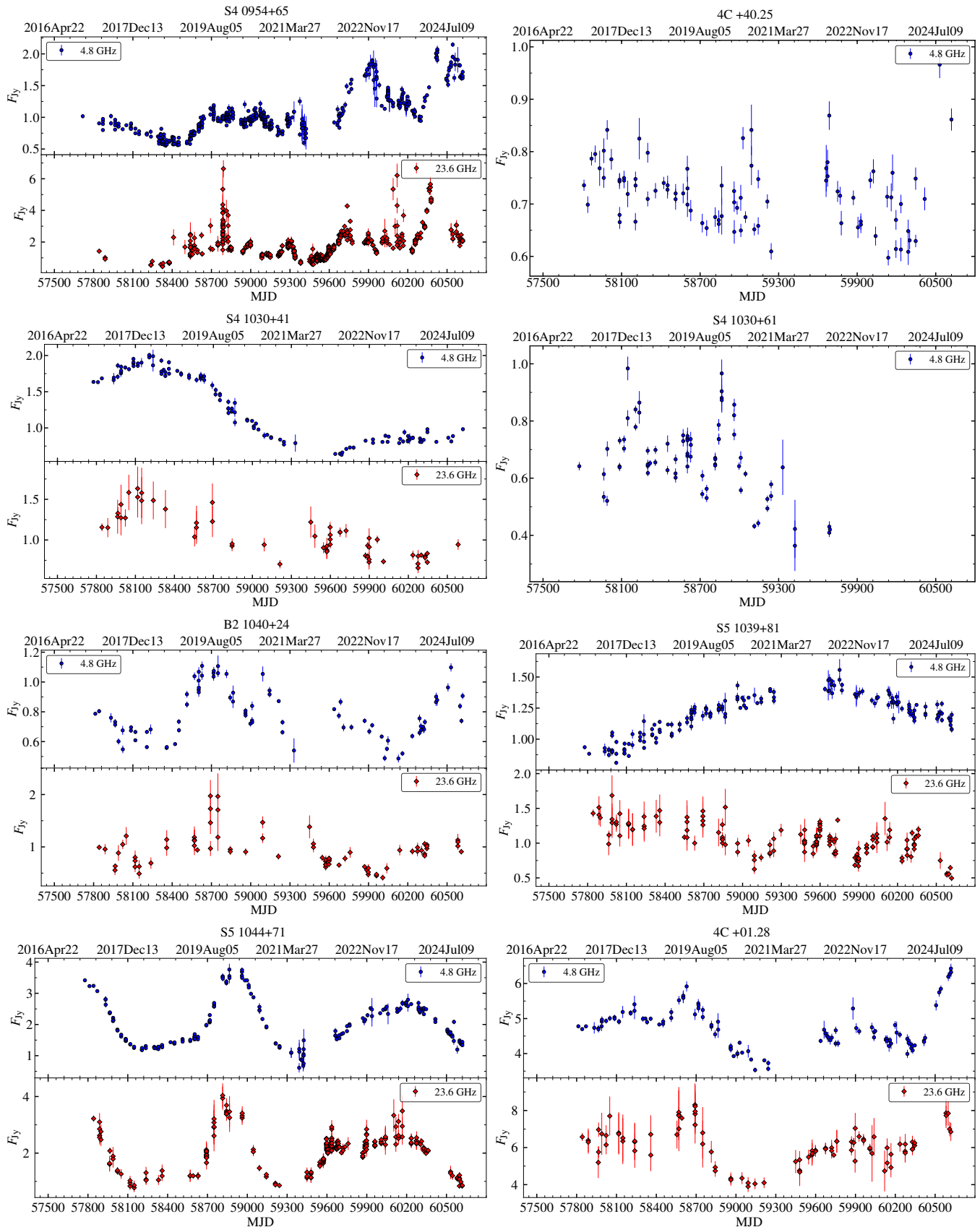


Figure 18. Continued.

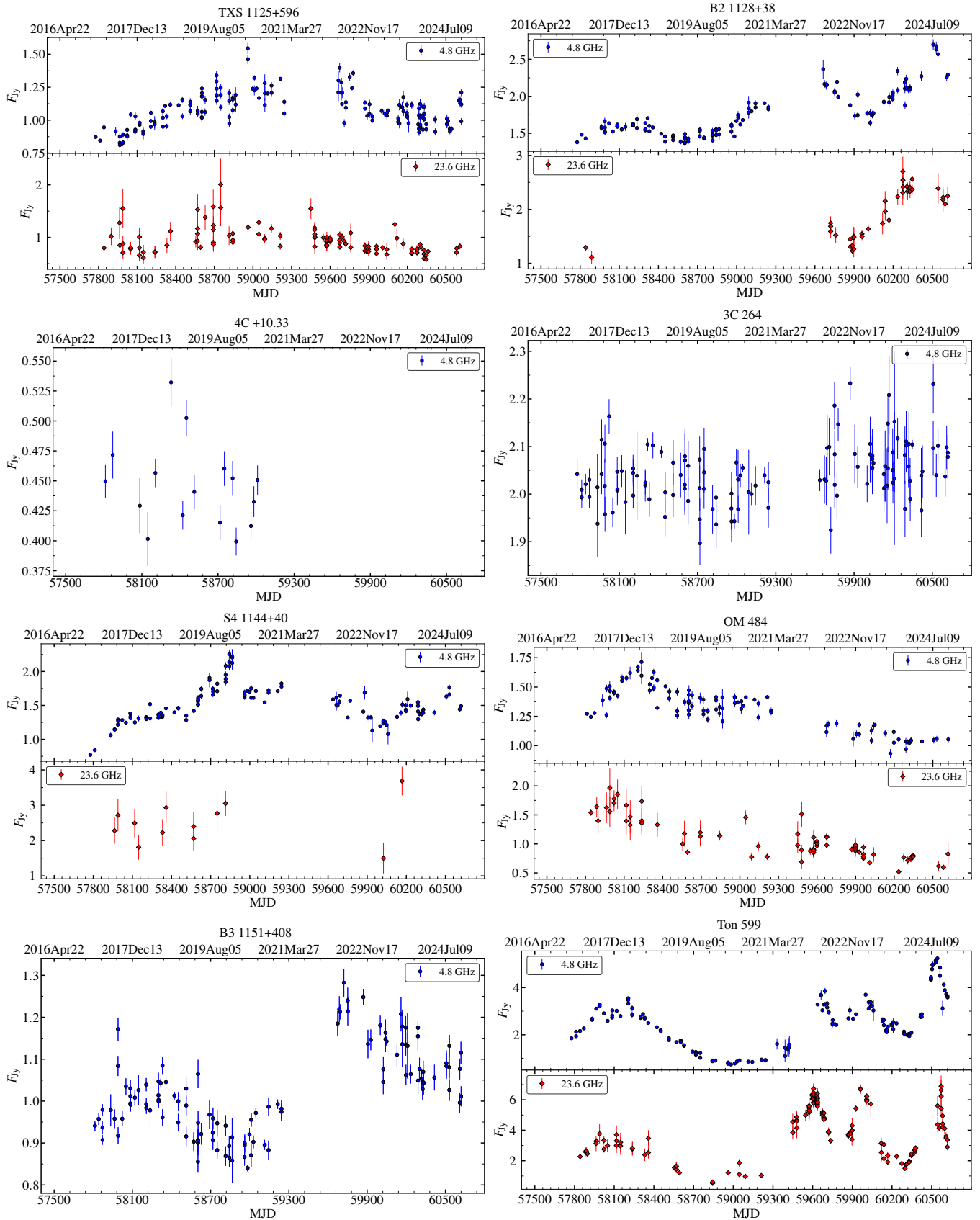


Figure 18. Continued.

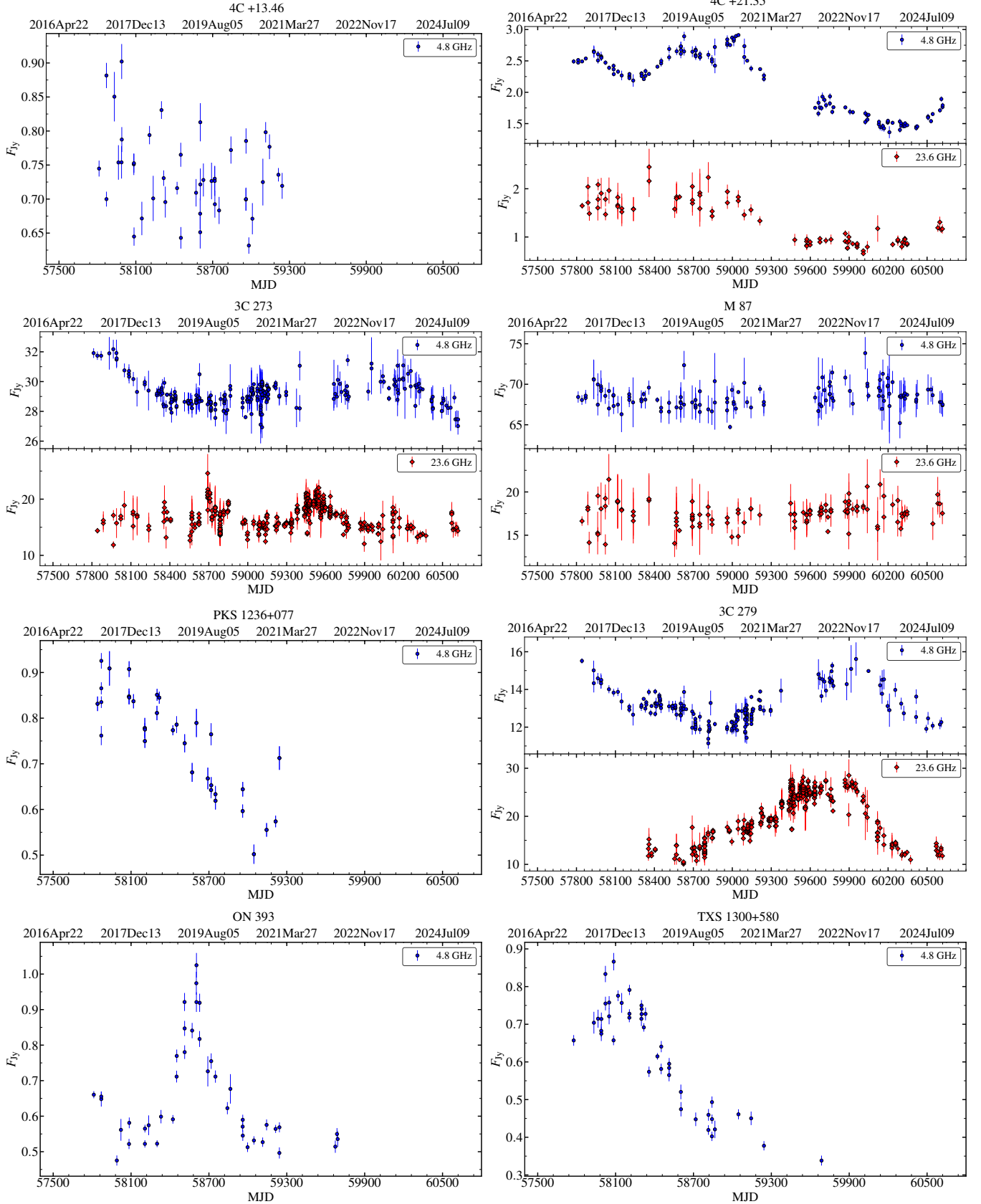


Figure 18. Continued.

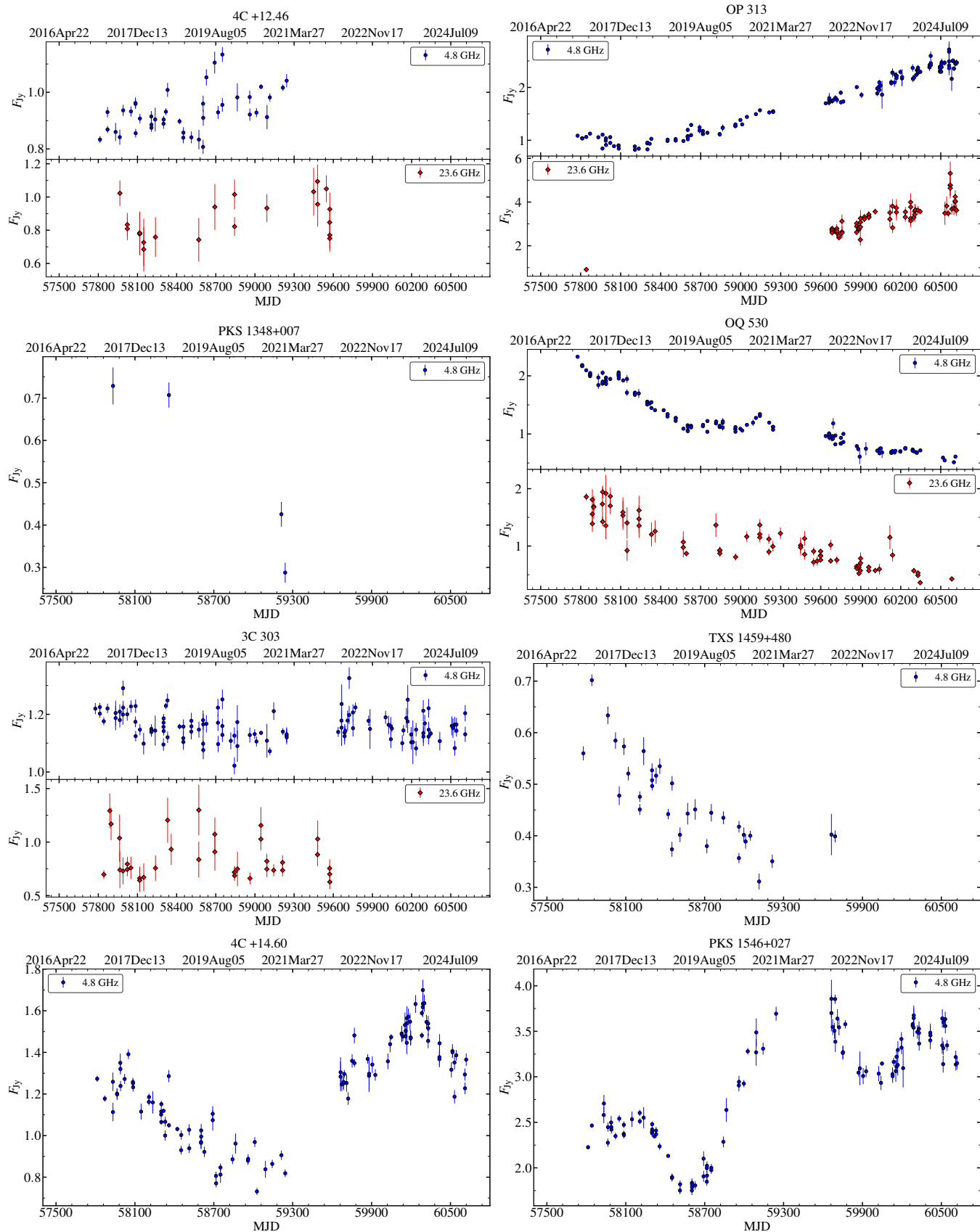


Figure 18. Continued.

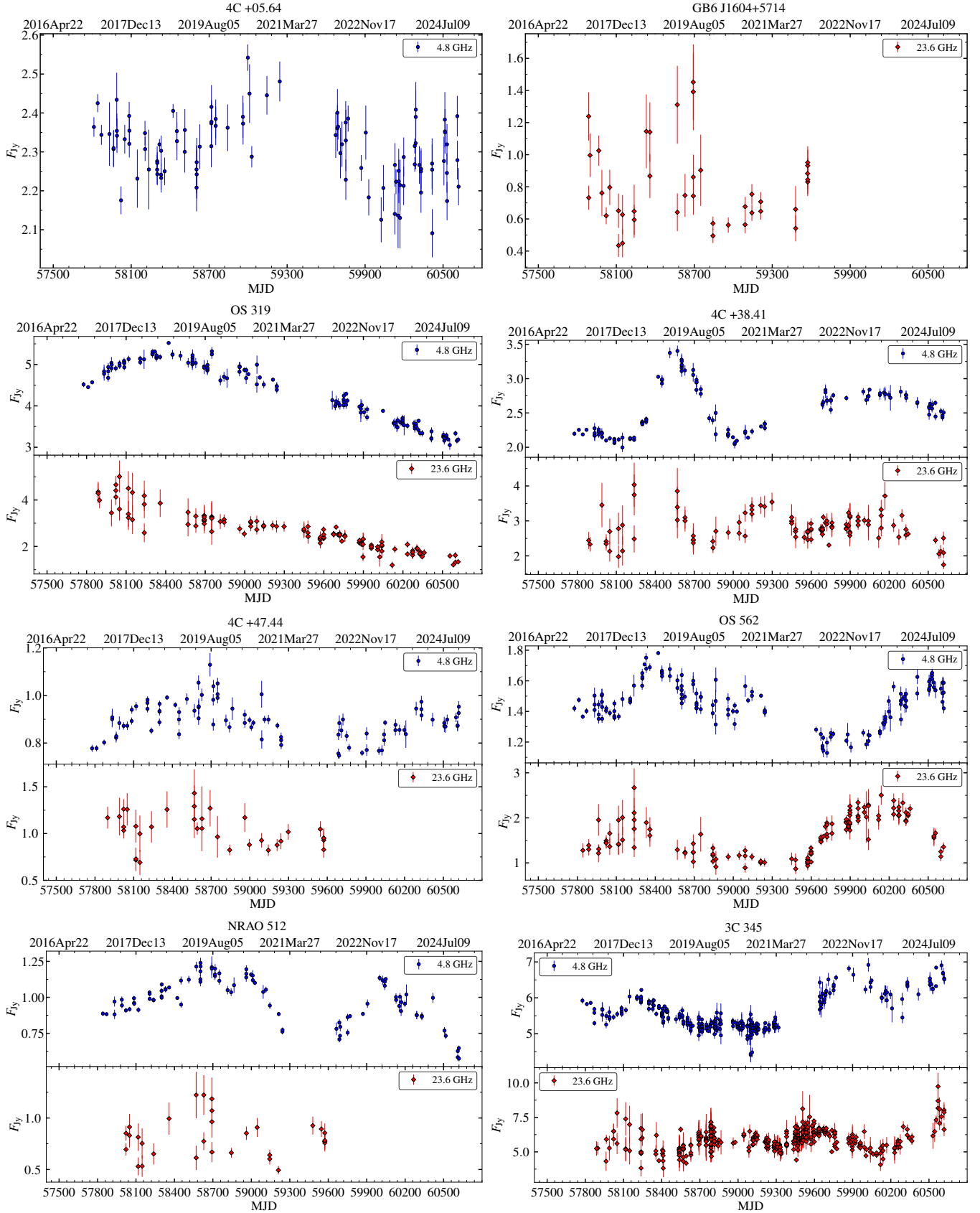


Figure 18. Continued.

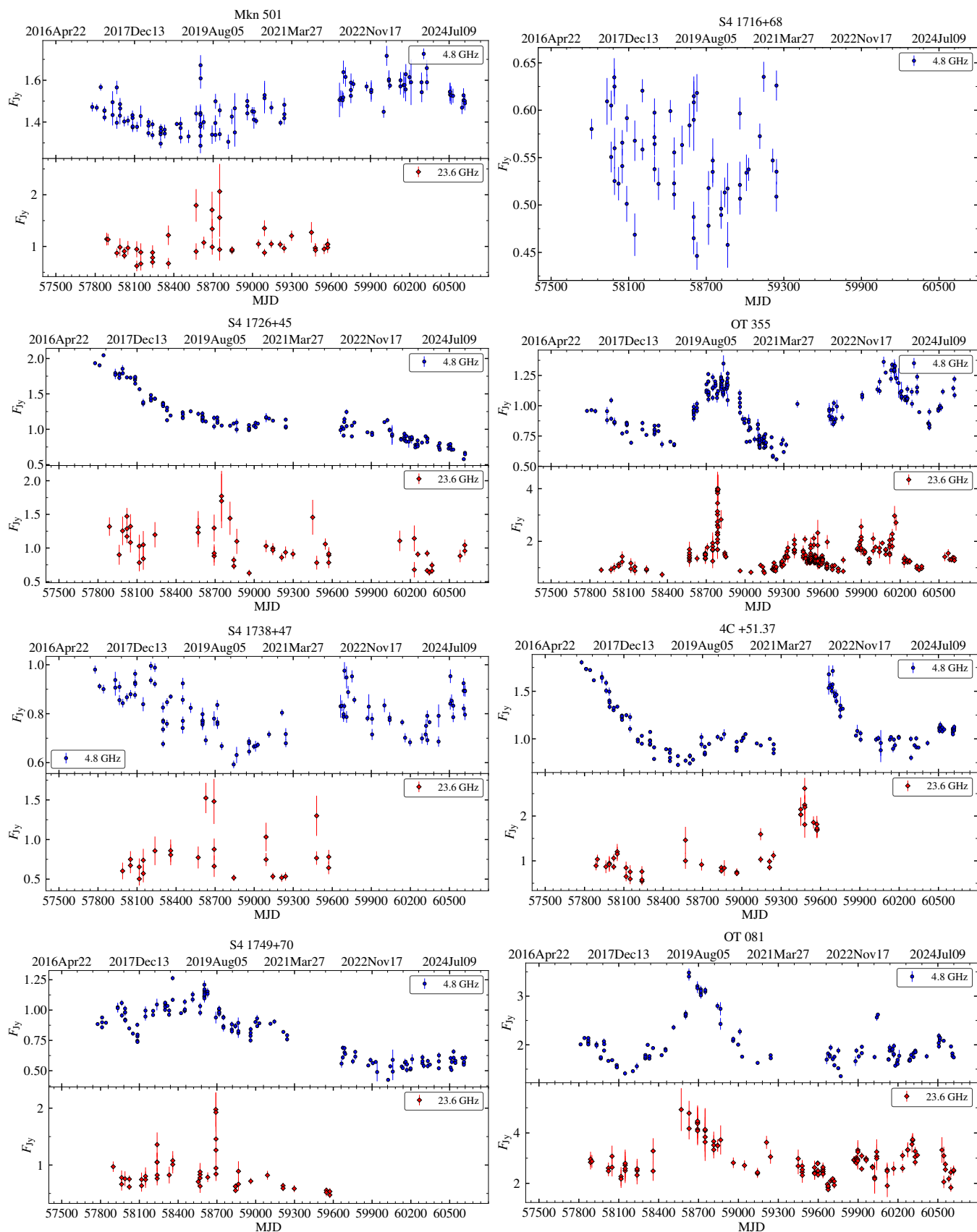


Figure 18. Continued.

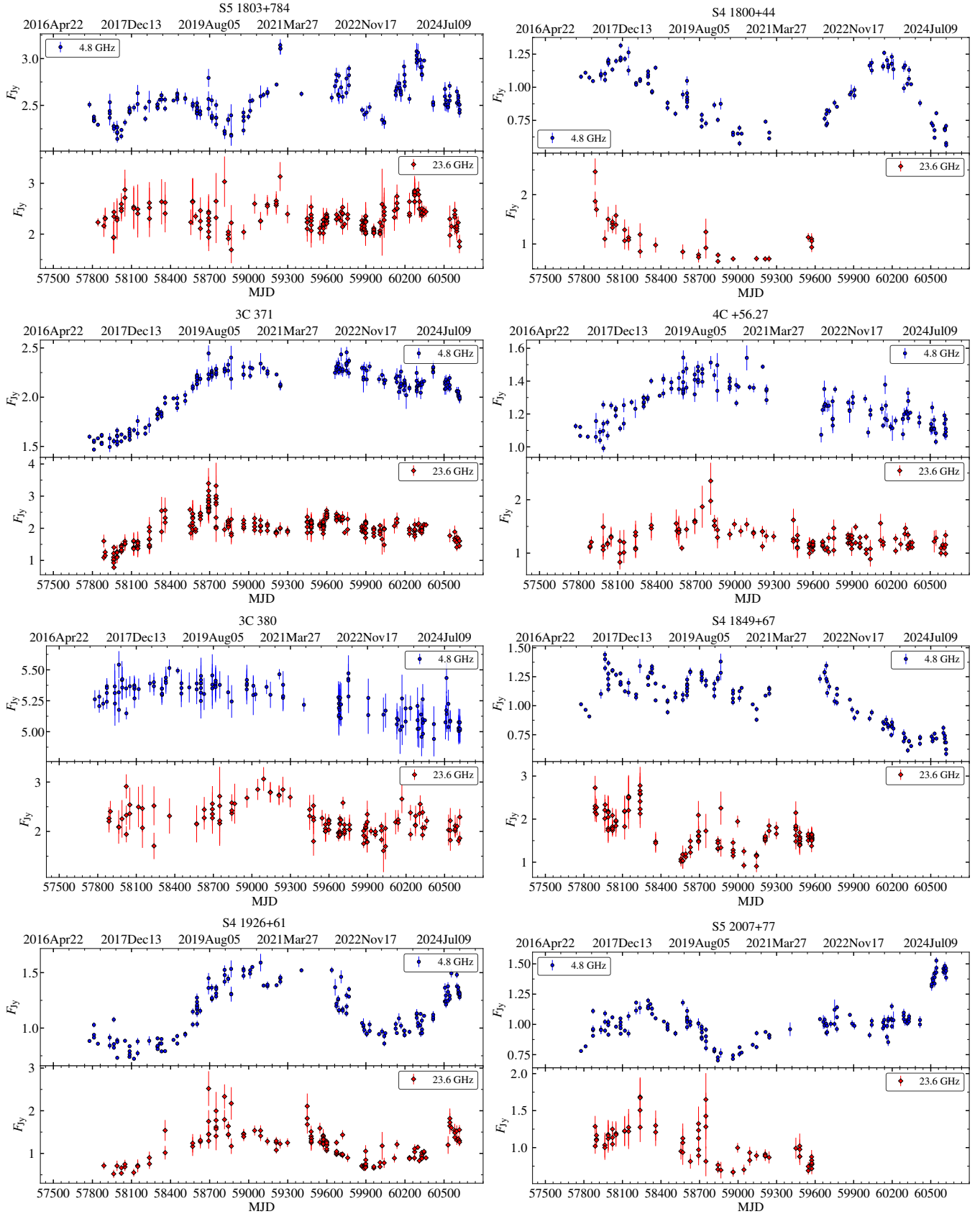


Figure 18. Continued.

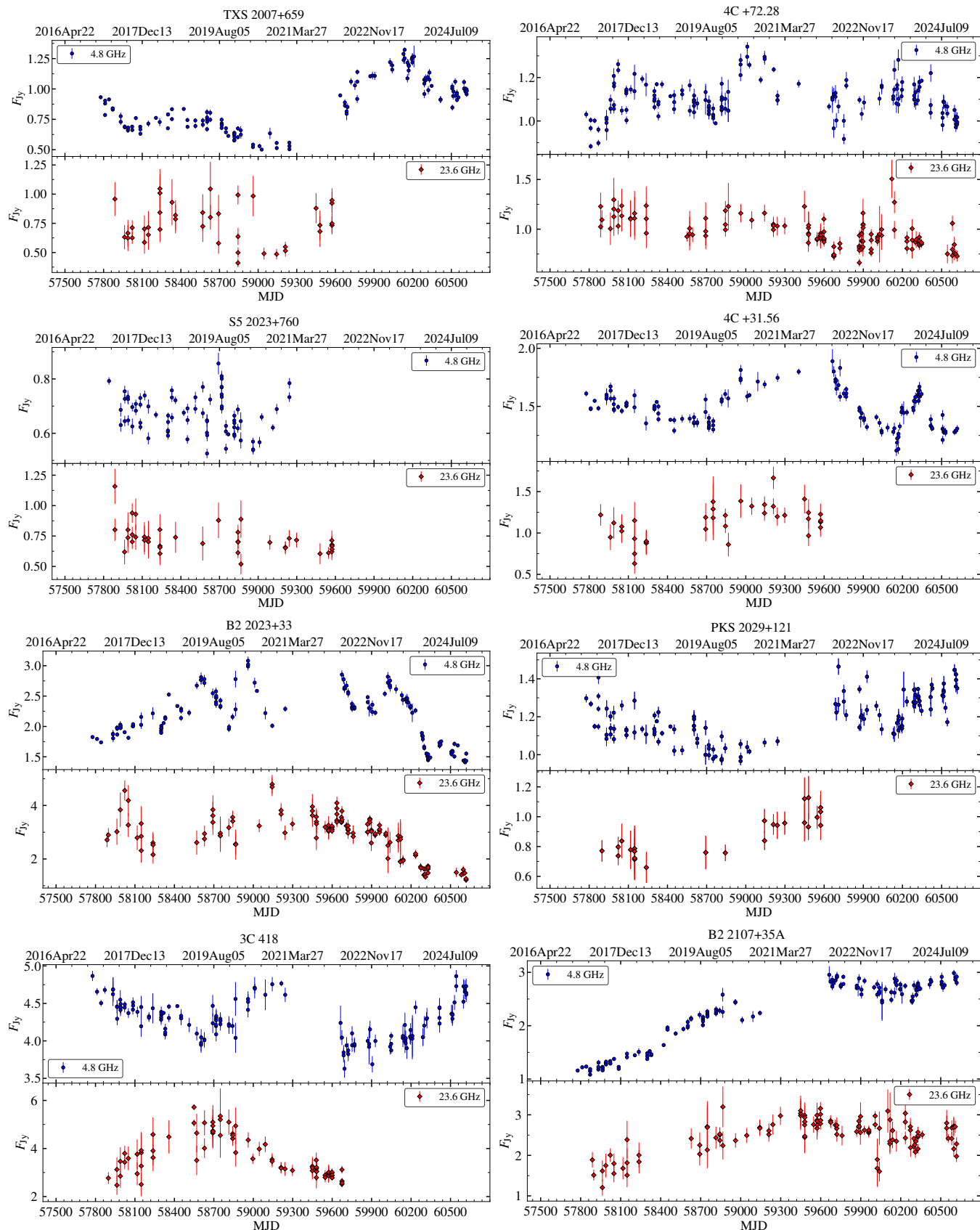
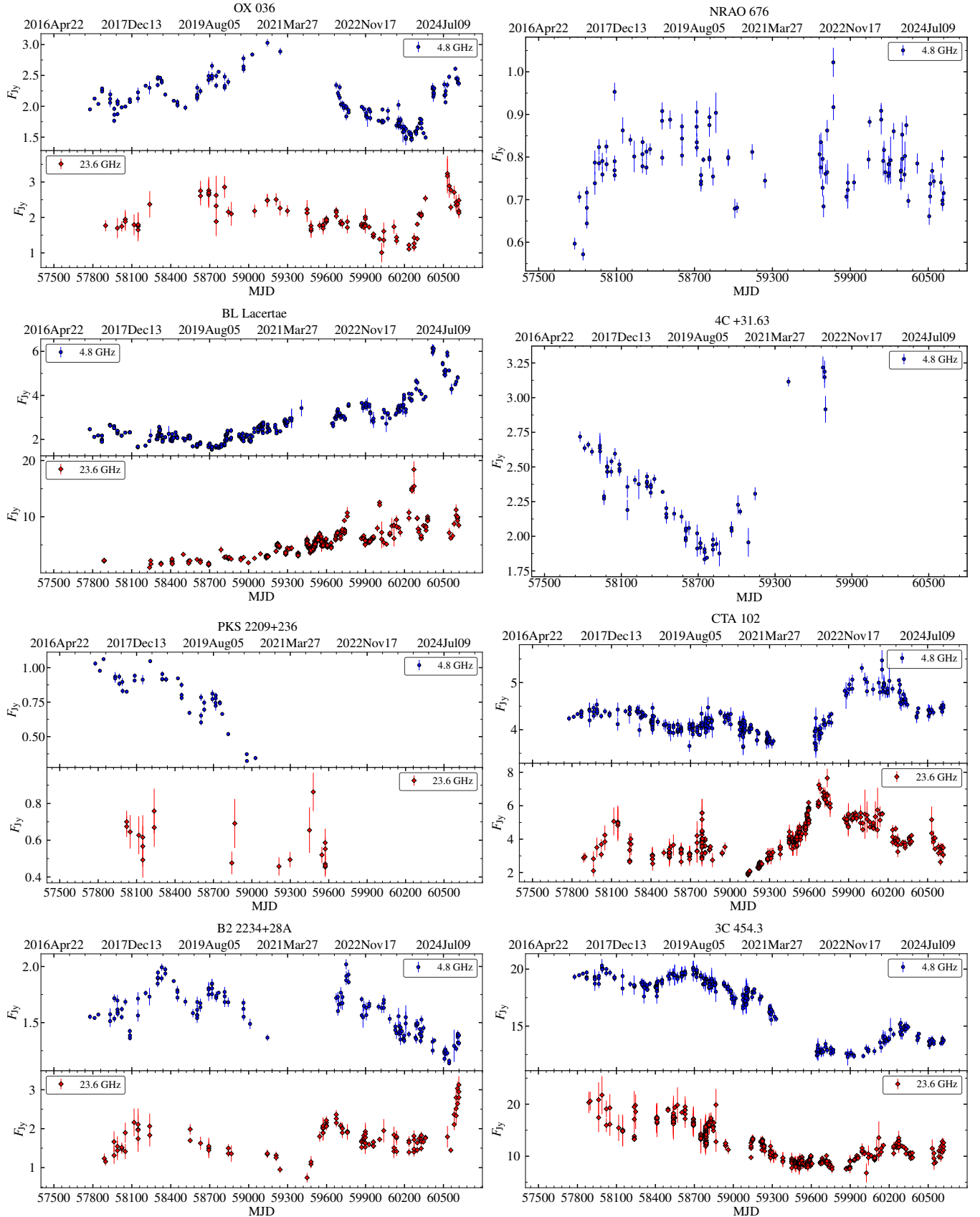
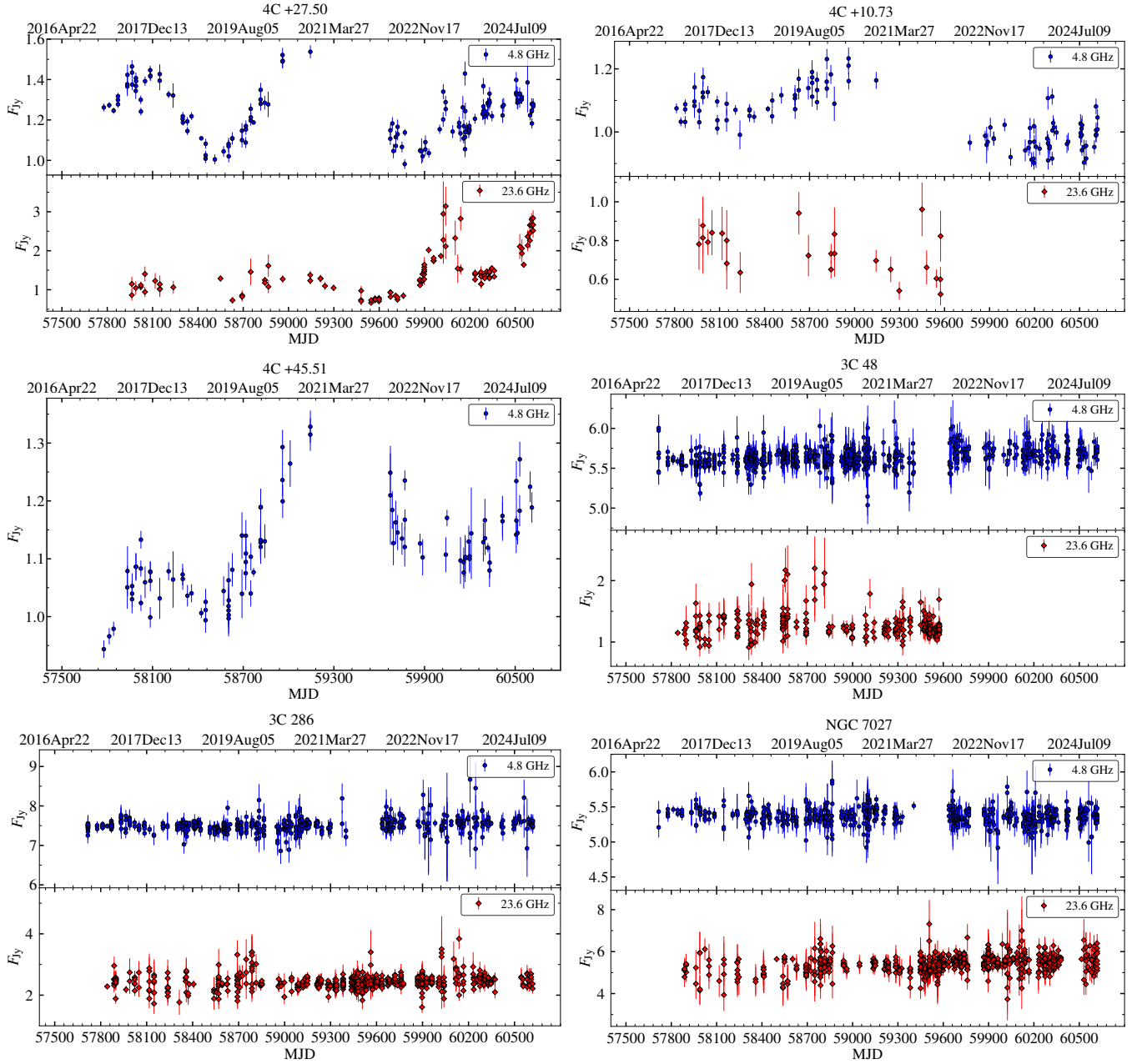


Figure 18. Continued.



- Frank, J., King, A., & Raine, D. 2002, *Accretion Power in Astrophysics*, 3rd edn. (Cambridge University Press), doi: [10.1017/CBO9781139164245](https://doi.org/10.1017/CBO9781139164245)
- Fuhrmann, L., Zensus, J. A., Krichbaum, T. P., Angelakis, E., & Readhead, A. C. S. 2007, in *American Institute of Physics Conference Series*, Vol. 921, *The First GLAST Symposium*, ed. S. Ritz, P. Michelson, & C. A. Meegan (AIP), 249–251, doi: [10.1063/1.2757314](https://doi.org/10.1063/1.2757314)
- Fuhrmann, L., Larsson, S., Chiang, J., et al. 2014, *MNRAS*, 441, 1899, doi: [10.1093/mnras/stu540](https://doi.org/10.1093/mnras/stu540)
- Fuhrmann, L., Angelakis, E., Zensus, J. A., et al. 2016, *A&A*, 596, A45, doi: [10.1051/0004-6361/201528034](https://doi.org/10.1051/0004-6361/201528034)
- Ghisellini, G., Maraschi, L., & Tavecchio, F. 2009, *MNRAS*, 396, L105, doi: [10.1111/j.1745-3933.2009.00673.x](https://doi.org/10.1111/j.1745-3933.2009.00673.x)
- Ghisellini, G., Tavecchio, F., Foschini, L., & Ghirlanda, G. 2011, *MNRAS*, 414, 2674, doi: [10.1111/j.1365-2966.2011.18578.x](https://doi.org/10.1111/j.1365-2966.2011.18578.x)
- Grossberger, C., Kadler, M., Wilms, J., et al. 2012, *Acta Polytechnica*, 52, 18, doi: [10.48550/arXiv.1110.1197](https://doi.org/10.48550/arXiv.1110.1197)
- Gurwell, M. A., Peck, A. B., Hostler, S. R., Darrah, M. R., & Katz, C. A. 2007, in *Astronomical Society of the Pacific Conference Series*, Vol. 375, *From Z-Machines to ALMA: (Sub)Millimeter Spectroscopy of Galaxies*, ed. A. J. Baker, J. Glenn, A. I. Harris, J. G. Mangum, & M. S. Yun, 234
- Hovatta, T., Tornikoski, M., Lainela, M., et al. 2007, *A&A*, 469, 899, doi: [10.1051/0004-6361:20077529](https://doi.org/10.1051/0004-6361:20077529)
- Hovatta, T., Petropoulou, M., Richards, J. L., et al. 2015, *MNRAS*, 448, 3121, doi: [10.1093/mnras/stv220](https://doi.org/10.1093/mnras/stv220)
- Hovatta, T., Lindfors, E., Kiehlmann, S., et al. 2021, *A&A*, 650, A83, doi: [10.1051/0004-6361/202039481](https://doi.org/10.1051/0004-6361/202039481)
- Hughes, P. A., Aller, M. F., & Aller, H. D. 2015, *ApJ*, 799, 207, doi: [10.1088/0004-637X/799/2/207](https://doi.org/10.1088/0004-637X/799/2/207)
- IceCube Collaboration, Aartsen, M. G., Ackermann, M., et al. 2018, *Science*, 361, 147, doi: [10.1126/science.aat2890](https://doi.org/10.1126/science.aat2890)
- Jorstad, S., & Marscher, A. 2016, *Galaxies*, 4, 47, doi: [10.3390/galaxies4040047](https://doi.org/10.3390/galaxies4040047)
- Jorstad, S. G., Marscher, A. P., Stevens, J. A., et al. 2007, *AJ*, 134, 799, doi: [10.1086/519996](https://doi.org/10.1086/519996)
- Kadler, M., Ros, E., Perucho, M., et al. 2008, *ApJ*, 680, 867, doi: [10.1086/529539](https://doi.org/10.1086/529539)
- Kankkunen, S., Tornikoski, M., Hovatta, T., & Lähteenmäki, A. 2025, *A&A*, 693, A318, doi: [10.1051/0004-6361/202450561](https://doi.org/10.1051/0004-6361/202450561)
- Kim, S.-H., Lee, S.-S., Lee, J. W., et al. 2022, *MNRAS*, 510, 815, doi: [10.1093/mnras/stab3473](https://doi.org/10.1093/mnras/stab3473)
- King, O. G., Hovatta, T., Max-Moerbeck, W., et al. 2013, *MNRAS*, 436, L114, doi: [10.1093/mnrasl/slt125](https://doi.org/10.1093/mnrasl/slt125)
- Knuth, K. H. 2006, arXiv e-prints, physics/0605197, doi: [10.48550/arXiv.physics/0605197](https://doi.org/10.48550/arXiv.physics/0605197)
- Kovalev, Y. A., Kardashev, N. S., Kovalev, Y. Y., et al. 2020, *Advances in Space Research*, 65, 745, doi: [10.1016/j.asr.2019.04.034](https://doi.org/10.1016/j.asr.2019.04.034)
- Krishna Mohana, A., Gupta, A. C., Marscher, A. P., et al. 2024, *MNRAS*, 527, 6970, doi: [10.1093/mnras/stad3583](https://doi.org/10.1093/mnras/stad3583)
- Kun, E., Jaroschewski, I., Ghorbanietemad, A., et al. 2022, *ApJ*, 940, 163, doi: [10.3847/1538-4357/ac9cce](https://doi.org/10.3847/1538-4357/ac9cce)
- Kun, E., Jaroschewski, I., Tjus, J. B., et al. 2024, *ApJL*, 963, L16, doi: [10.3847/2041-8213/ad2767](https://doi.org/10.3847/2041-8213/ad2767)
- Kunert-Bajraszewska, M., Krauze, A., Kimball, A. E., et al. 2025, *ApJS*, 277, 50, doi: [10.3847/1538-4365/ada68f](https://doi.org/10.3847/1538-4365/ada68f)
- Larionov, V. M., Jorstad, S. G., Marscher, A. P., et al. 2020, *MNRAS*, 492, 3829, doi: [10.1093/mnras/staa082](https://doi.org/10.1093/mnras/staa082)
- Li, X.-P., Yang, H.-Y., Cai, Y., et al. 2023, *ApJ*, 943, 157, doi: [10.3847/1538-4357/acaec8c](https://doi.org/10.3847/1538-4357/acaec8c)
- Liodakis, I., Romani, R. W., Filippenko, A. V., et al. 2018, *MNRAS*, 480, 5517, doi: [10.1093/mnras/sty2264](https://doi.org/10.1093/mnras/sty2264)
- Marchili, N., Righini, S., Giroletti, M., et al. 2025, arXiv e-prints, arXiv:2509.04577, doi: [10.48550/arXiv.2509.04577](https://doi.org/10.48550/arXiv.2509.04577)
- Marscher, A. P. 2016, *Galaxies*, 4, 37, doi: [10.3390/galaxies4040037](https://doi.org/10.3390/galaxies4040037)
- Marscher, A. P., Jorstad, S. G., Larionov, V. M., et al. 2010, *ApJL*, 710, L126, doi: [10.1088/2041-8205/710/2/L126](https://doi.org/10.1088/2041-8205/710/2/L126)
- Max-Moerbeck, W., Hovatta, T., Richards, J. L., et al. 2014, *MNRAS*, 445, 428, doi: [10.1093/mnras/stu1749](https://doi.org/10.1093/mnras/stu1749)
- Mingaliev, M. G., Sotnikova, Y. V., Udovitskiy, R. Y., et al. 2014, *A&A*, 572, A59, doi: [10.1051/0004-6361/201424437](https://doi.org/10.1051/0004-6361/201424437)
- Mohana A, K., Gupta, A. C., Fan, J., et al. 2025, *ApJ*, 989, 125, doi: [10.3847/1538-4357/adeec77](https://doi.org/10.3847/1538-4357/adeec77)
- Molina, B., Mróz, P., De la Parra, P. V., et al. 2025, arXiv e-prints, arXiv:2510.23103, doi: [10.48550/arXiv.2510.23103](https://doi.org/10.48550/arXiv.2510.23103)
- Mufakharov, T., Mingaliev, M., Sotnikova, Y., Naiden, Y., & Erkenov, A. 2015, *MNRAS*, 450, 2658, doi: [10.1093/mnras/stv772](https://doi.org/10.1093/mnras/stv772)
- Orienti, M., D’Ammando, F., Giroletti, M., et al. 2014, *MNRAS*, 444, 3040, doi: [10.1093/mnras/stu1644](https://doi.org/10.1093/mnras/stu1644)
- Ott, M., Witzel, A., Quirrenbach, A., et al. 1994, *A&A*, 284, 331
- Paliya, V. S., Böttcher, M., Gurwell, M., & Stalin, C. S. 2021, *ApJS*, 257, 37, doi: [10.3847/1538-4365/ac365d](https://doi.org/10.3847/1538-4365/ac365d)
- Parijskij, Y. N. 1993, *IEEE Antennas and Propagation Magazine*, 35, 7, doi: [10.1109/74.229840](https://doi.org/10.1109/74.229840)
- Planck Collaboration, Ade, P. A. R., Aghanim, N., et al. 2016, *A&A*, 594, A13, doi: [10.1051/0004-6361/201525830](https://doi.org/10.1051/0004-6361/201525830)
- Plavin, A., Kovalev, Y. Y., Kovalev, Y. A., & Troitsky, S. 2020, *ApJ*, 894, 101, doi: [10.3847/1538-4357/ab86bd](https://doi.org/10.3847/1538-4357/ab86bd)

Figure 18. Continued.



- Principe, G. 2022, arXiv e-prints, arXiv:2209.03652, doi: [10.48550/arXiv.2209.03652](https://doi.org/10.48550/arXiv.2209.03652)
- Pushkarev, A. B., Butuzova, M. S., Kovalev, Y. Y., & Hovatta, T. 2019, MNRAS, 482, 2336, doi: [10.1093/mnras/sty2724](https://doi.org/10.1093/mnras/sty2724)
- Raiteri, C. M., Villata, M., Larionov, V. M., et al. 2007, A&A, 473, 819, doi: [10.1051/0004-6361:20078289](https://doi.org/10.1051/0004-6361:20078289)
- Raiteri, C. M., Villata, M., Acosta-Pulido, J. A., et al. 2017, Nature, 552, 374, doi: [10.1038/nature24623](https://doi.org/10.1038/nature24623)
- Raiteri, C. M., Villata, M., Carnerero, M. I., et al. 2024, A&A, 692, A48, doi: [10.1051/0004-6361/202452311](https://doi.org/10.1051/0004-6361/202452311)
- Readhead, A. C. S., Aller, M. F., Sullivan, A. G., et al. 2025, arXiv e-prints, arXiv:2511.09409, doi: [10.48550/arXiv.2511.09409](https://doi.org/10.48550/arXiv.2511.09409)
- Rees, M. J. 1966, Nature, 211, 468, doi: [10.1038/211468a0](https://doi.org/10.1038/211468a0)
- Richards, J. L., Max-Moerbeck, W., Pavlidou, V., et al. 2011, ApJS, 194, 29, doi: [10.1088/0067-0049/194/2/29](https://doi.org/10.1088/0067-0049/194/2/29)
- Sotnikova, Y., Mikhailov, A., Mufakharov, T., et al. 2021, MNRAS, 508, 2798, doi: [10.1093/mnras/stab2114](https://doi.org/10.1093/mnras/stab2114)
- Sotnikova, Y. V., Mufakharov, T. V., Majorova, E. K., et al. 2019, Astrophysical Bulletin, 74, 348, doi: [10.1134/S1990341319040023](https://doi.org/10.1134/S1990341319040023)
- Sotnikova, Y. V., Mufakharov, T. V., Mingaliev, M. G., et al. 2022, Astrophysical Bulletin, 77, 361, doi: [10.1134/S1990341322040149](https://doi.org/10.1134/S1990341322040149)
- Stickel, M., Padovani, P., Urry, C. M., Fried, J. W., & Kuehr, H. 1991, ApJ, 374, 431, doi: [10.1086/170133](https://doi.org/10.1086/170133)
- Stoeckel, J. T., Morris, S. L., Gioia, I. M., et al. 1991, ApJS, 76, 813, doi: [10.1086/191582](https://doi.org/10.1086/191582)
- Teraesranta, H., Tornikoski, M., Mujunen, A., et al. 1998, A&AS, 132, 305, doi: [10.1051/aas:1998297](https://doi.org/10.1051/aas:1998297)
- Urry, C. M., & Padovani, P. 1995, PASP, 107, 803, doi: [10.1086/133630](https://doi.org/10.1086/133630)
- Vaughan, S., Edelson, R., Warwick, R. S., & Uttley, P. 2003, MNRAS, 345, 1271, doi: [10.1046/j.1365-2966.2003.07042.x](https://doi.org/10.1046/j.1365-2966.2003.07042.x)
- Villata, M., Raiteri, C. M., Gurwell, M. A., et al. 2009, A&A, 504, L9, doi: [10.1051/0004-6361/200912732](https://doi.org/10.1051/0004-6361/200912732)
- Wang, N., Yi, T.-F., Wang, L., et al. 2023, Research in Astronomy and Astrophysics, 23, 115011, doi: [10.1088/1674-4527/ace9b1](https://doi.org/10.1088/1674-4527/ace9b1)
- Wenger, M., Ochsenbein, F., Egret, D., et al. 2000, A&AS, 143, 9, doi: [10.1051/aas:2000332](https://doi.org/10.1051/aas:2000332)
- Yang, J. H., Fan, J. H., Liu, Y., et al. 2022, ApJS, 262, 18, doi: [10.3847/1538-4365/ac7deb](https://doi.org/10.3847/1538-4365/ac7deb)
- Zijlstra, A. A., van Hoof, P. A. M., & Perley, R. A. 2008, ApJ, 681, 1296, doi: [10.1086/588778](https://doi.org/10.1086/588778)